

# Photoelectron Spectroscopy of Transition Metal Chalcogenides: Charge Density Wave Phase and Thermoelectric Performance

Kapila Wijayaratne  
Kandy, Sri Lanka

B.Sc., University of Peradeniya, Sri Lanka, 2010

A Dissertation presented to the Graduate Faculty of the University  
of Virginia in Candidacy for the Degree of Doctor of Philosophy

Department of Physics

University of Virginia

May, 2019



# *Abstract*

The successful exfoliation of graphene in 2004 ignited the interest in two-dimensional materials within the scientific community. Since then, the study of atomically thin and ultrathin layered materials has grown as an interdisciplinary field and over the years, hundreds of new two-dimensional materials have been discovered. This dissertation focuses on the transition metal dichalcogenides, which is the most commonly studied family of two-dimensional materials after graphene. Among a wide range of physical phenomena exhibited by these compounds, the incommensurate charge density wave phase of the  $2H$ - polytype of  $\text{TaS}_2$  is primarily analyzed in comparison to the similar compounds,  $2H$ - $\text{NbSe}_2$  and  $2H$ - $\text{TaSe}_2$ . Angle resolved photoemission spectroscopy (ARPES) is used as the primary experimental probe for the presented band structure studies due to its unique ability to resolve both energy and momentum in order to map intricate details of the reciprocal space.

The momentum space of a  $2H$ - transition metal dichalcogenide consists of concentric double-walled Fermi barrels about both K and  $\Gamma$  high symmetry points in its normal state. Using this momentum space landscape as a blueprint, the presented work identifies both generalizable and compound-specific features of the incommensurate charge density wave order of these compounds. Reported experiments are conducted in energy, momentum, and temperature domains.

In general, the  $\Gamma$ - centric Fermi surface barrels exhibit no charge density wave energy gap, while K- centric barrels are preferentially gapped. However, the details of the

momentum specificity of the gap change among compounds. These variations can be explained using the differences in orientations of transition metal  $d$ -orbitals. Further, this gap is particle-hole asymmetric with respect to the chemical potential throughout the momentum space. Contrary to the expectations, a gap is observed at temperatures higher than the charge density wave transition temperature. Comparable pseudogaps have been observed in several compounds under the scientific spotlight, including high temperature cuprate superconductors. In the case of charge density waves, this pseudogap can be related to short-range ordering in the sample which remains even at higher temperatures, despite the long-range charge density wave phase coherence being diminished. When comparing momentum space maps among different samples, the sizes of the  $\Gamma$ -centric Fermi surface barrels stay the same while the  $K$ -barrel sizes vary. Within the samples studied, these variations can be correlated with charge density wave transition temperatures of each compound.

Formulating a model applicable for the entire material class is of utmost importance as a basis for further understanding of these materials. However, according to preceding literature, initial attempts of explaining the formation of charge density waves using the traditional ‘Fermi surface nesting’ model have been persistently unsuccessful. On the other hand, in the case of presented work, an alternate tight binding model with strong electron-collective mode coupling is successful in explaining the reported observations. In support of this model, observed band dispersions of the samples show distinct renormalization signatures due to electrons getting coupled to some collective modes.  $2H - \text{TaS}_2$  was further analyzed in order to probe the underlying cause of these collective modes where they are identified as phonons. The work presented suggests that

the mechanism behind the incommensurate charge density wave phase of the  $2H-$  polytype of transition metal dichalcogenides is the electron-phonon coupling, rather than the Fermi surface nesting.

Lead chalcogenide, which is another class of transition metal chalcogenides with a three-dimensional structure is studied in order to understand their band structure and the mechanism leading to the outstanding thermoelectric performance observed above a characteristic crossover temperature. The mechanism behind this phenomenon is controversial, mainly in terms of predicted crossover temperature values. The study of  $n$  and  $p$  doped PbTe, PbSe, and PbS reveal an upper valence band with lighter holes and a lower valence band with heavier holes. This is the first experimental observation of the lower valence band of these compounds.

Upon the increase of the temperature, the lower valence band which lies below the upper valence band rises in energy and eventually crosses over to become the topmost valence band. The heavier holes in the lower valence band increase the thermal carrier density, leading to superior thermoelectric performance at higher temperatures. Additionally, the indirect nature of the bandgap helps in mitigating any adverse effects due to intrinsic carrier activation. Apart from demonstrating the details of this mechanism via a series of temperature dependent ARPES measurements, crossover temperature values are also predicted for the compounds under study. The superior thermoelectric efficiency of lead chalcogenides can be explained by the temperature dependent convergence of light and heavy hole valence bands.

---

# *Acknowledgements*

*“If I have seen further, it is by standing on the shoulders of giants”*

- Sir Isaac Newton (in a letter to Robert Hooke, dated 5<sup>th</sup> February 1676)

Evolution of one’s self from a college student to a doctoral graduate is only possible with a wide network of support. I have been fortunate to receive the aid and guidance from many amazing people throughout the long and sometimes painstaking years leading to this dissertation.

First and foremost, I would like to express my sincere gratitude to my advisor Prof. Utpal Chatterjee for the invaluable guidance, constant inspiration and thoughtful suggestions I have received throughout my life as a graduate student. From the day I joined the UVa-ARPES research group, he had a plan for my success and actively guided me through the numerous obstacles of graduate life until the end. Through his unique ‘big brother’ approach, he shared his expert knowledge and wisdom with me, not just as my research advisor, but as an advisor for many aspects of life. I owe him a deep debt of gratitude for being such an excellent advisor.

I must express my profoundly felt gratitude to the members of the thesis committee. Prof. Despina Louca, whom I first got to know as the graduate director, has been a source of expert advice since the day I stepped into the University of Virginia. Her insight as a senior research collaborator of our group is appreciated as well. Prof. Israel Klich is a long-standing member of my research committee, and his feedback has been crucial in shaping up my research plans. The help and interest extended by Prof. Nikhil Shukla are appreciated with gratitude. I also acknowledge former review committee

members, Prof. Hank Thacker, Prof. Cass Sackett, and Prof. Thomas Gallagher as well. I especially should thank Prof. Nilanga Liyanage, The associate chair and former graduate director for advice and support on numerous occasions. Prof. Maxim Bychkov, Prof. Rick Marshall, and Prof. Olivier Pfister have also helped me in various means in the past seven years in graduate school.

High-quality samples provided by Prof. Mercuri Kanatzidis and Dr. Christos Malliakas at the Chemistry Department of the Northwestern University and Argonne National Laboratory were vital for the presented work. Theoretical insight from Prof. Jasper Van Wezel at the University of Amsterdam, Institute of Theoretical Physics was invaluable. I thank our research scientist, Dr. Junjing Zhao who aided me in developing my instrumentation and data analysis skills. I also acknowledge the help I got in numerous avenues from our current and former group members; Dr. Junqiang Li, Dr. N. Apathurai and Mr. Vis Karlapati. I thank the Spectroscopy of Novel Materials Group at the Paul Scherrer Institute, Prof. Ming Shi, Prof. Milan Radovic, Dr. Nicholas Plumb, and Dr. Mengyu Yao for their friendly and tireless assistance.

Physics machine shop, electronics shop, and the demonstration laboratory deserve my gratitude for the training and assistance granted. Mr. William Fariss and Mr. BH are acknowledged for training me, along with Mr. David Wimer and Mr. Kevin Warren. Sincere thanks go to Mr. Larry St. John, Dr. Al Tobias, Mr. Nikolay Sandev, Dr. Bryan Wright, Mr. Stephen Goadhouse, and Mr. Mike Beverage for various technical, electronics and IT support. I should thank Mr. Peter Cline, Ms. Dawn Shifflett, Ms. Tammie Shifflett and Ms. Beth Guyton along with the rest of the administrative staff and our librarian, Ms. Vicky Ingram deserves a special thanks as well.

I would like to thank all my friends for helping me in numerous aspects along the journey. I express my special gratitude to Dr. Sachith Dissanayake, Dr. Anushika Athauda and Ms. Sanuki Dissanayake for being what is closest to a family here in the USA. I appreciate the vital support from Dr. Anjana Samarakoon, Mr. Anuruddha Rathnayake, and Mr. John Boyd as well. Also, Sumudu, Harshanee, Manula, Kumudu, Amali, Udari, Viranga, Safra, Thushani, Maduka, Kanchana and James lead the long list of friends who shared my joy and helped when I needed.

I am thankful for the invaluable academic foundation I gained from all the teachers of my school, Kingswood College and from the wonderful professors at the Physics Department of the University of Peradeniya, Sri Lanka. I also thank my father, (late) Mr. Gamunu Wijayaratne, my aunt, Mrs. Sujata Kulatunga, and all other relatives back home in Sri Lanka. At last, but not least, my sincere gratitude goes to my loving mother, Mrs. Chandra Wijayaratne who thoughtfully prepared me from the early childhood toward handling the challenges in education as well as turbulences of life.

---

# Contents

<b>Abstract</b>	<b>ii</b>
<b>Acknowledgements</b>	<b>v</b>
<b>Contents</b>	<b>viii</b>
<b>List of Figures</b>	<b>xi</b>
<b>List of Tables</b>	<b>xiii</b>
<b>Abbreviations</b>	<b>xiv</b>
<b>Physical Constants</b>	<b>xvi</b>
<b>1 Introduction</b>	<b>1</b>
1.1 Charge Density Waves in Transition Metal Dichalcogenides . . . . .	3
1.1.1 Transition Metal Dichalcogenides (TMDs) . . . . .	3
1.1.2 Charge Density Wave (CDW) Phenomena . . . . .	5
1.1.3 The Formation of Charge Density Waves in Transition Metal Dichalco- genides . . . . .	9
1.2 Thermoelectric Performance of Lead Chalcogenides . . . . .	12
1.2.1 Thermoelectric Effect . . . . .	12
1.2.1.1 Seeback Effect . . . . .	13
1.2.1.2 Peltier Effect . . . . .	14
1.2.1.3 Thomson Effect . . . . .	15
1.2.1.4 Thermoelectric Figure of Merit . . . . .	16
1.2.2 Lead Chalcogenides . . . . .	16
1.3 Organization of the Dissertation . . . . .	18
<b>2 Experimental Techniques</b>	<b>20</b>
2.1 Angle Resolved Photoemission Spectroscopy (ARPES) . . . . .	20
2.1.1 The Photoelectric Effect . . . . .	20
2.1.2 Energetics of Photoemission . . . . .	22
2.1.3 Visualization of the Photoemission Process . . . . .	24

2.1.3.1	One-Step Model	25
2.1.3.2	Three-Step Model	28
2.1.3.3	The Sudden Approximation	30
2.1.3.4	Photoemission Intensity	32
2.1.4	Kinematics of Photoemission	35
2.1.4.1	ARPES of Low-Dimensional Systems	41
2.1.5	Spectral Function Formalism of ARPES Data	42
2.1.5.1	Self Energy Formalism	45
2.2	Representation of ARPES Data	46
2.2.1	Energy Momentum Intensity Maps (EMIMs)	49
2.2.2	Constant Energy Intensity Maps (CEIMs)	50
2.2.3	Momentum Distribution Curves (MDCs)	50
2.2.4	Energy Distribution Curves (EDCs)	51
2.2.5	Conditioning ARPES Data	51
2.2.5.1	Division by the Fermi Function	52
2.2.5.2	Lucy-Richardson Deconvolution	53
2.3	Experimental Details	54
<b>3</b>	<b>Charge Density Waves in Transition Metal Dichalcogenides</b>	<b>56</b>
3.1	Background	56
3.2	The Charge Density Wave Vector, $\mathbf{q}_{\text{CDW}}$	57
3.3	Low Energy Electronic Structure of $2H$ - TMDs	59
3.3.1	Fermi Surface Topology	59
3.3.2	Fermi Surface Barrels	61
3.3.3	Possibility of Fermi Surface Nesting	64
3.3.3.1	Fermi Surface Nesting as a CDW Mechanism	64
3.3.3.2	Nesting Conditions in TMDs	65
3.3.3.3	Electronic Susceptibility Studies	66
3.3.3.4	Motivation for a Strong Coupling Approximation	67
3.4	Charge Density Wave Energy Gap, $\Delta_{\text{CDW}}$	68
3.4.1	Analysis Procedure for the CDW Energy Gap	68
3.4.2	Momentum Dependence of the CDW Energy Gap	69
3.4.2.1	Bogoliubov Dispersion Signatures of the CDW Phase	69
3.4.2.2	Momentum Anisotropy of the CDW Energy Gap	71
3.4.2.3	Momentum Specificity of the CDW Energy Gap	73
3.4.2.4	Particle – Hole Asymmetry of the CDW Energy Gap	75
3.4.3	Temperature Dependence of the CDW Energy Gap	77
3.4.4	Origin of the Pseudogap	79
3.4.5	Orbital Selectivity and the Anisotropy of the CDW Energy Gap	80
3.5	Summary	84
<b>4</b>	<b>Electron–Phonon Coupling in <math>2H</math>–TaS<sub>2</sub></b>	<b>86</b>
4.1	Background	86
4.2	Self-Energy of the Band Renormalization	88
4.2.1	Self-Energy and the Spectral Function	88
4.2.2	Extraction of the Self-Energy Components from ARPES Data	89

4.2.3	Self-Energy and the Lineshapes of MDC Peaks . . . . .	90
4.3	Identification of the Phonon Modes in <b>2H-TaS<sub>2</sub></b> . . . . .	92
4.3.1	Tracing the Electronic Band Dispersion . . . . .	92
4.3.2	Renormalization Signatures in the Electronic Band Dispersion . . . . .	94
4.3.3	Renormalization Signatures in the Self-Energy . . . . .	97
4.3.4	Renormalizations Due to the Unidentified Collective Modes . . . . .	99
4.4	Momentum and Temperature Dependence of the Band Renormalization . . . . .	100
4.4.1	The Electron-Phonon Coupling Parameter, $\lambda(\mathbf{k})$ . . . . .	100
4.4.2	Momentum Dependence of the Band Renormalization . . . . .	101
4.4.3	Temperature Dependence of the Band Renormalization . . . . .	104
4.5	Summary . . . . .	105
<b>5</b>	<b>Thermoelectric Performance of Lead Chalcogenides</b> . . . . .	<b>106</b>
5.1	Background . . . . .	106
5.1.1	The Band Structure of PbQ . . . . .	106
5.1.2	Samples . . . . .	108
5.2	Hole Pockets in the Momentum Space . . . . .	109
5.2.1	Analysis of Constant Energy Intensity Maps . . . . .	109
5.2.2	High and Low Energy Hole Pockets . . . . .	110
5.3	Energy- Momentum Dispersion . . . . .	112
5.3.1	Resolution of the Band Edges . . . . .	113
5.3.2	Band Edges of PbQ . . . . .	116
5.3.3	Reconstructed Band Dispersions of PbQ . . . . .	119
5.3.4	Effective Masses . . . . .	123
5.3.5	Identification of the Band Gaps . . . . .	124
5.3.6	Variation of the Band Gap Among PbQ . . . . .	125
5.4	Temperature Evolution of the Bands . . . . .	127
5.5	Explanation of the Thermoelectric Efficiency of Lead Chalcogenides . . . . .	130
5.6	Summary . . . . .	134
<b>6</b>	<b>Conclusions</b> . . . . .	<b>138</b>
6.1	Charge Density Wave Phase of Transition Metal Dichalcogenides . . . . .	138
6.2	Thermoelectric Performance of Lead Chalcogenides . . . . .	141

# List of Figures

1.1	Structures of two-dimensional materials . . . . .	2
1.2	Crystal structure of transition metal dichalcogenides (TMDs). . . . .	4
1.3	Characteristics of the charge density wave (CDW) phase. . . . .	6
1.4	Normal and CDW states of $2H$ - and $1T$ -TMDs . . . . .	10
1.5	Seeback and Peltier effects . . . . .	15
1.6	Real and reciprocal space structures of Lead chalcogenides . . . . .	17
2.1	The concept of angle resolved photoemission spectroscopy (ARPES) . . . .	21
2.2	Energetics of photoemission spectroscopy . . . . .	23
2.3	One- and three- step models of photoemission . . . . .	25
2.4	Initial and final eigenstates for a semi-infinite crystal . . . . .	27
2.5	ARPES spectra for interacting and non-interacting electronic systems . .	34
2.6	The geometry of angle resolved photoemission . . . . .	36
2.7	Kinematics of photoemission spectroscopy . . . . .	37
2.8	Representation of ARPES data . . . . .	47
2.9	Fermi function and effective temperature . . . . .	53
3.1	Charge density wave vectors of $2H$ - transition metal dichalcogenides . . .	58
3.2	Fermi surfaces and charge density wave vectors . . . . .	60
3.3	Fermi surface barrels of $2H - \text{TaS}_2$ . . . . .	62
3.4	Nesting vectors Vs. charge density wave vectors . . . . .	66
3.5	Back bending of the bands due to Bogoliubov dispersion . . . . .	70
3.6	Energy distribution curves around K and $\Gamma$ symmetry points in the charge density wave state of $2H - \text{TaS}_2$ . . . . .	72
3.7	Variation of the energy gap in $2H - \text{NbSe}_2$ . . . . .	74
3.8	Symmetry of energy gaps in charge density wave state Vs. superconduct- ing state . . . . .	76
3.9	Temperature dependence of the energy distribution curves . . . . .	78
3.10	Tight binding model band structure for $2H - \text{NbSe}_2$ . . . . .	81
3.11	Possible orientations for $d_{z^2}$ orbitals of three neighboring transition metal cations . . . . .	82
4.1	Band reconstruction of $2H - \text{TaS}_2$ using momentum distribution curves . .	93
4.2	Band renormalization signatures of $2H - \text{TaS}_2$ due to the presence of collective modes . . . . .	95
4.3	Band renormalization signatures of $2H - \text{NbSe}_2$ . . . . .	96
4.4	Renormalization signatures in self-energy . . . . .	99
4.5	Momentum dependence of the electron-phonon coupling in $2H - \text{TaS}_2$ . .	102

---

4.6	Momentum dependence of the electron-phonon coupling in $2H - \text{NbSe}_2$	103
4.7	Temperature dependence of the electron-phonon coupling	104
5.1	Low and high energy hole pockets of doped PbTe, PbSe and PbS	111
5.2	$2^{\text{nd}}$ derivative analysis of band edges	114
5.3	Locating the band edges of PbQ	118
5.4	$2^{\text{nd}}$ derivatives of energy momentum intensity maps	120
5.5	Energy momentum intensity maps, and upper and lower band dispersions of PbQ	122
5.6	Schematic band structure of PbQ	126
5.7	Temperature evolution of the band edges	128
5.8	Temperature evolution of band gaps	130
5.9	Temperature evolution of the band structure	132

# List of Tables

3.1	Comparison of orbital overlap integrals in $2H - \text{NbSe}_2$ and $2H - \text{TaS}_2$ .	83
5.1	Values of effective mass of the UVB ( $m_{UVB}^*$ ), and that of the LVB ( $m_{LVB}^*$ ) in units of electronic mass $m_e$	124
5.2	Values of $\Delta_L$ , $\Delta_U$ , and $\Delta$ obtained from $n$ -type PbTe, PbSe, and PbS samples at $T \sim 100\text{K}$	126
5.3	Comparison of various parameters from this study with existing data for PbTe, PbSe and PbS.	133

# Abbreviations

<b>ARPES</b>	Angle Resolved Photoemission Spectroscopy
<b>PES</b>	Photoemission Spectroscopy
<b>STM</b>	Scanning Tunneling Microscope
<b>SEM</b>	Scanning Electron Microscope
<b>TEM</b>	Transmission Electron Microscopy
<b>UHV</b>	Ultra-High Vacuum
<b>HTSC</b>	High Temperature Superconductor
<b>BCS</b>	Bardeen Copper Schrieffer (theory of superconductivity)
<b><math>T_C</math></b>	Critical temperature (superconducting)
<b>TMD</b>	Transition Metal Dichalcogenides (a.k.a., TMDC)
<b>PbQ</b>	Lead chalcogenides (Q: S, Se, or Te)
<b>EMIM</b>	Energy-Momentum Intensity Map
<b>CEIM</b>	Constant Energy Intensity Map

<b>EDC</b>	Energy Distribution Curve
<b>MDC</b>	Momentum Distribution Curve
<b>FS</b>	Fermi Surface
<b>CDW</b>	Charge Denisty Wave
<b>PLD</b>	Periodic Lattice Distortion
$\Delta_{CDW}$	Charge Denisty Wave Energy Gap
$q_{CDW}$	Charge Denisty Wave Energy Gap
$T_{CDW}$	Charge Denisty Wave Energy Gap
<b>UVB</b>	Upper Valence Band
<b>LVB</b>	Lower Valence Band
<b>CB</b>	Conduction Band

# Physical Constants

Speed of Light  $c = 2.997\,924\,58 \times 10^8 \text{ ms}^{-2}$

Planck Constant  $h = 6.62606957(29) \times 10^{34} \text{ J s}$   
 $= 4.135667516(91) \times 10^{15} \text{ eV s}$

Reduced Planck Constant  $\hbar = 1.054571726(47) \times 10^{34} \text{ J s}$   
 $= 6.58211928(15) \times 10^{16} \text{ eV s}$

Rest Mass of Electron  $m_e = 9.10938215(45) \times 10^{31} \text{ kg}$

Boltzmann constant  $k_B = 1.3806488(13) \times 10^{23} \text{ J K}^{-1}$   
 $= 8.6173324(78) \times 10^5 \text{ eV K}^{-1}$

*Dedicated to my loving mother,  
Mrs. Chandra Wijayaratne ...*

# Chapter 1

## Introduction

A two-dimensional material, in general, can be described as a hybrid between a solid, in the periodic plane -and- a molecule, in the perpendicular direction[1]. In these materials, electrons have the freedom of motion in a two-dimensional plane but are restricted in the third dimension. Graphene, shown in the Fig. 1.1(a), is the simplest example and is an atomically thin material[2]. These materials in their common form are stacked in layers, such as graphite. Despite many fascinating properties of graphene, the lack of an electronic bandgap has led to the discovery of other two-dimensional materials with semiconducting properties[3, 4]. Of the several hundred two-dimensional materials that exist, transition metal dichalcogenides (TMDs)[3] will be studied in this dissertation. As shown in the Fig 1.1(g), these ultra-thin materials are quasi-two-dimensional structures.

Two-dimensional materials, including TMDs, possess a variety of electronic properties existing as insulators, semimetals, metals, superconductors, charge density wave materials and semiconductors with direct and indirect band gaps covering the range from ultraviolet to infrared including the visible spectrum. Band structures of TMDs will be studied using angle resolved photoemission spectroscopy (ARPES).

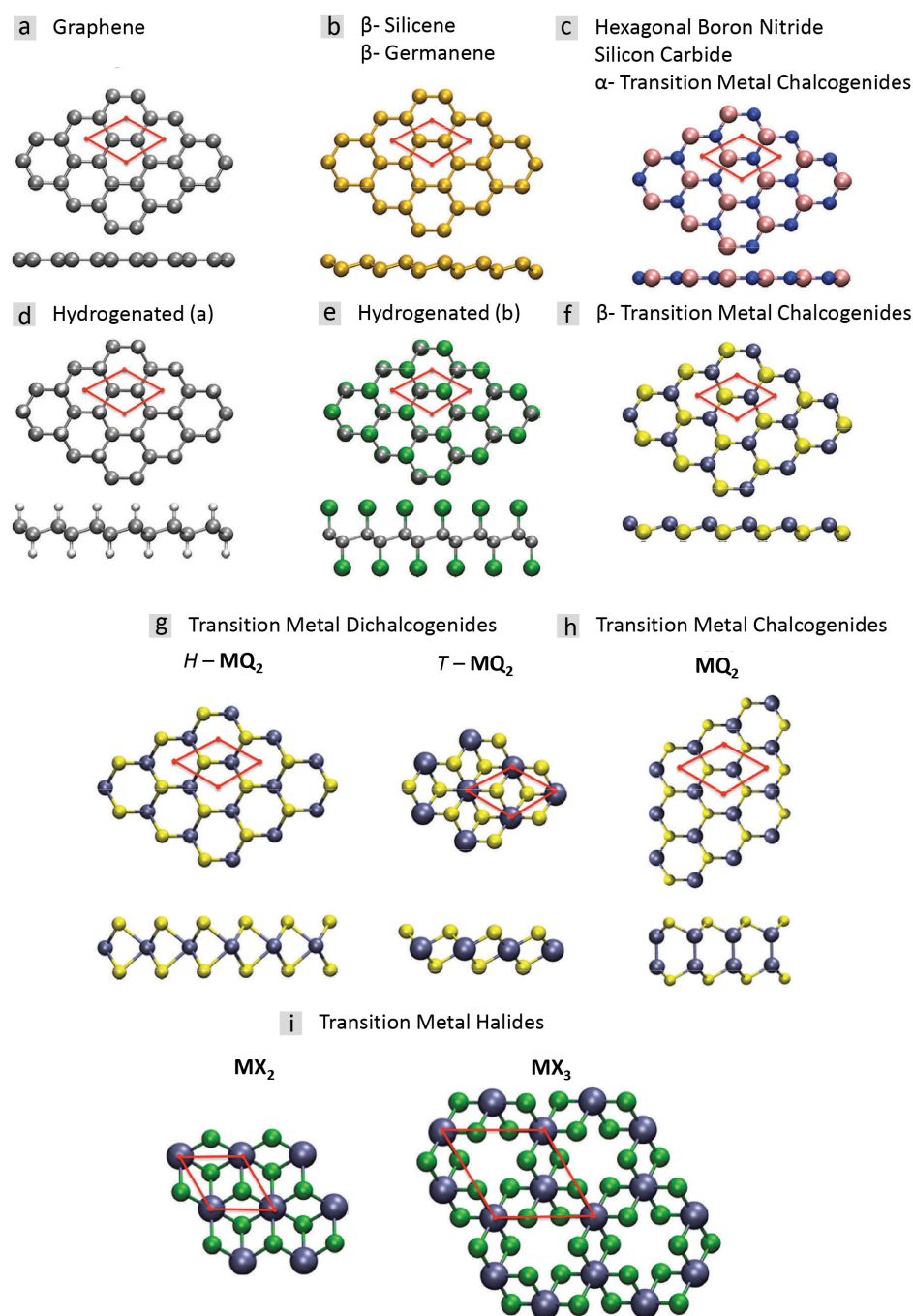


FIGURE 1.1: Structures of two-dimensional materials. [1]

**Atomically thin 2D materials:** (a) graphene, (b) silicene, germanene and; (d,e) their derivatives, (c) silicon carbide (SiC), hexagonal boron nitride ( $H$ -BN), the class of  $\alpha$ - transition metal chalcogenides ( $\alpha$ -TMC). and (f) the class of  $\beta$ - transition metal chalcogenides ( $\beta$ -TMC). **Ultrathin 2D materials:** (g)  $H$  and  $T$  polytypes of transition metal dichalcogenides (TMD), (h) the class of transition metal chalcogenides (TMC) and (i) the class of transition metal halides (TMH). Unit cells are depicted in red. Color code: metals(M) in dark blue, halides(X) in green, chalcogenides(Q) in yellow, nitrogen in medium blue, carbon in grey, silicon and germanium in gold, boron in pink and hydrogen in white.

## 1.1 Charge Density Waves in Transition Metal Dichalcogenides

### 1.1.1 Transition Metal Dichalcogenides (TMDs)

Chalcogenides are chemical compounds consisting of group 16 anions (S, Se, and Te, in particular) and at least one electropositive element. In the case of TMDs, this cation is a transition metal. They have the chemical formula  $\text{MQ}_2$ , where M is a transition metal, and Q is a chalcogen. TMDs are about 60 in number, and about 40 (~60%) of them are quasi 2D layered structures[5], where a transition metal(M) layer is sandwiched between two chalcogen(Q) layers as in Q-M-Q layering order as shown in Fig. 1.2(d). Atoms are held with intra-layer chemical bondings, forming slabs. Such slabs are stacked in a layered arrangement as in Fig. 1.2(c) with comparatively weak inter-layer Van-Der-Walls bondings. This quasi-two-dimensional nature leads to a higher degree of anisotropy in the electronic structure.

Layered TMDs is a class of materials with rich phase diagrams, spanning over a diverse spectrum of quantum phenomena such as metallic phases, semiconductivity, Mott insulator behavior, metal insulator-transitions, Kondo effect, superconductivity and charge density waves[6–10][6, 11–18], including phase competition/coexistence of the latter two[19–21]. The layered nature of TMDs make them quasi 2D structures, somewhat analogous to graphene, but with a layer thickness of 3 atoms. Techniques such as strain engineering [22], exfoliation [23] and chemical intercalation [11, 17, 24–30] can be used to enhance desired properties of these materials [12, 13, 31–34]. Further, TMDs can be formed into mono layers, ultra-thin layers and nanostructures for a series of applications including chemical electro-catalysis, opto-electronics, batteries and supercapacitors[35].

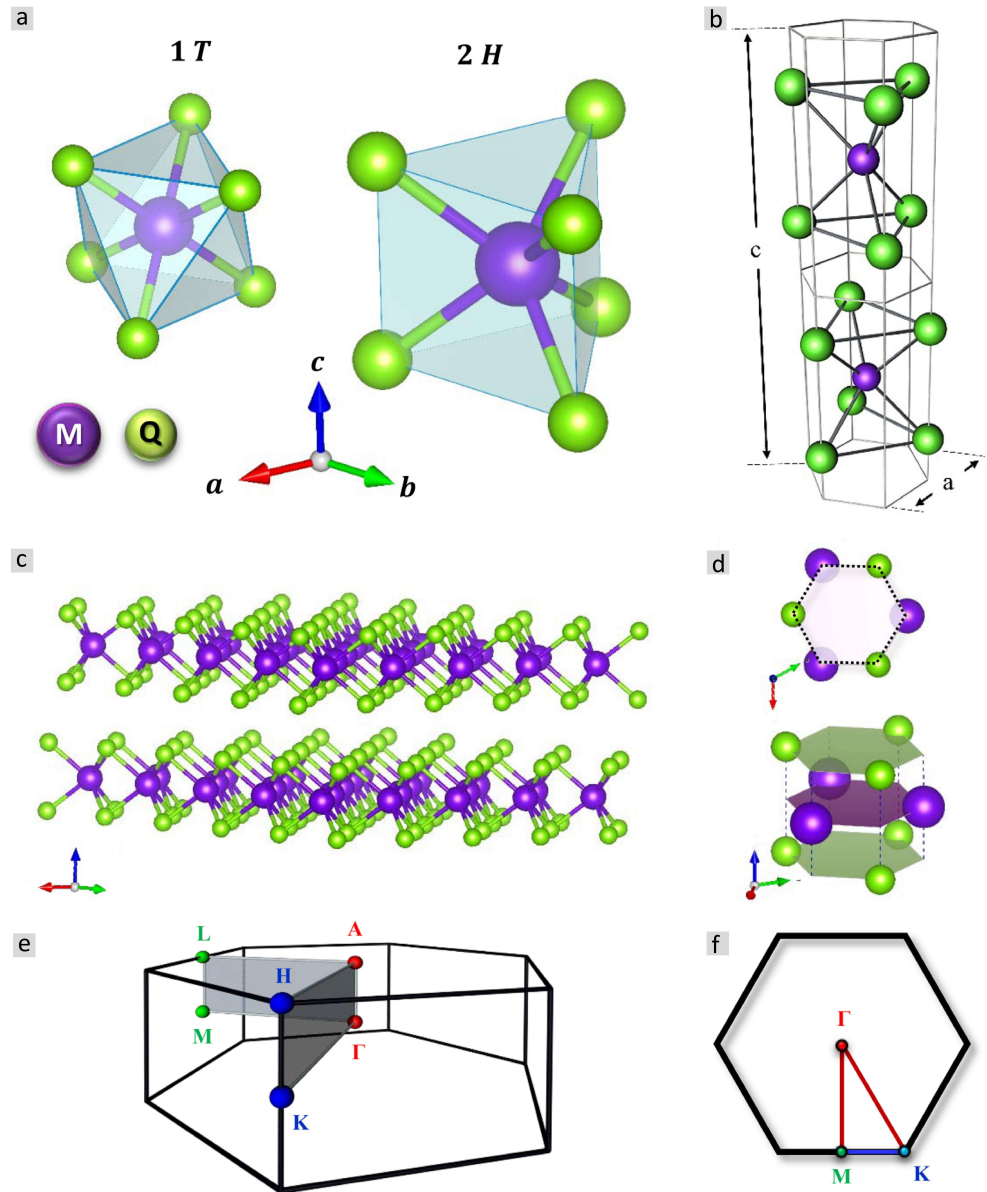


FIGURE 1.2: **Crystal structure of transition metal dichalcogenides (TMDs).** (a) The 1T (*octahedral*) and 2H (*trigonal prismatic*) structures assumed by TMDs. ‘M’ is a transition metal cation and ‘Q’ is a chalcogen (group 16) anion. (b) Unit cell for the 2H polytype, note that the existence of two MQ<sub>2</sub> formula units in one unit cell. (c) Two adjacent slabs of 2H-MQ<sub>2</sub> held by Van-Der-Walls bondings. (d) Placement of metal (M) and chalcogen (Q) atoms in an alternating layered arrangement in the 2H structure. (e) First Brillouin zone in the reciprocal space for the 2H-MQ<sub>2</sub> with key symmetry points labeled. (f) Hexagonal two dimensional Brillouin zone.

For example, Fe intercalated  $2H$  – TaSe<sub>2</sub> alloys have shown highly improved magnetocrystalline anisotropy [36].

Among the several crystal structures exhibited by these compounds, *Trigonal 1T* and *Hexagonal 2H* structures with *octahedral (trigonal anti-prismatic)* and *trigonal prismatic* coordination are the most prominent polytypes [5, 9, 37–39]. These structures are shown in Fig. 1.2(a). This study considers  $2H$ –polytype which consists of two QM<sub>2</sub> formula units per unit cell as shown in the Fig. 1.2(b)[10].  $2H$ – structure has  $D_{3h}$  point group symmetry and  $P6_3/mmc$  (No.194) space group symmetry[40, 41] while the reciprocal space group is  $P6/mmm^*$  (No.191). A simplified three-dimensional Brillouin zone diagram is given in the Fig. 1.2(e) and the two-dimensional projection of this Brillouin zone is a hexagon, as shown in the Fig. 1.2(f).

### 1.1.2 Charge Density Wave (CDW) Phenomena

The driving factor of the CDW order is the pairing of electrons and holes, while the electron–electron pairing is responsible for superconductivity. In the latter case, *Bogoliubov dispersion* is the signature of the pairing, which has been experimentally verified via ARPES measurements for compounds like high temperature cuprate superconductors [42–44]. In general, Bogoliubov dispersion is an approximate solution for the ground state of a quantum system of identical bosons, for a given potential. To figure out the characteristic dispersion signature for CDW pairing, denote the wave vector,  $\mathbf{q}_{CDW}$  as  $\mathbf{q}$  for the simplicity. As an example, Fig. 1.3(b) shows a specific case when  $\mathbf{q} = 2k_F$ , where  $k_F$  is the Fermi momentum. Consider an electron with a momentum  $\mathbf{k}$  which would have an electronic dispersion (i.e., energy as a function of momentum),  $\epsilon_{\mathbf{k}}$ .

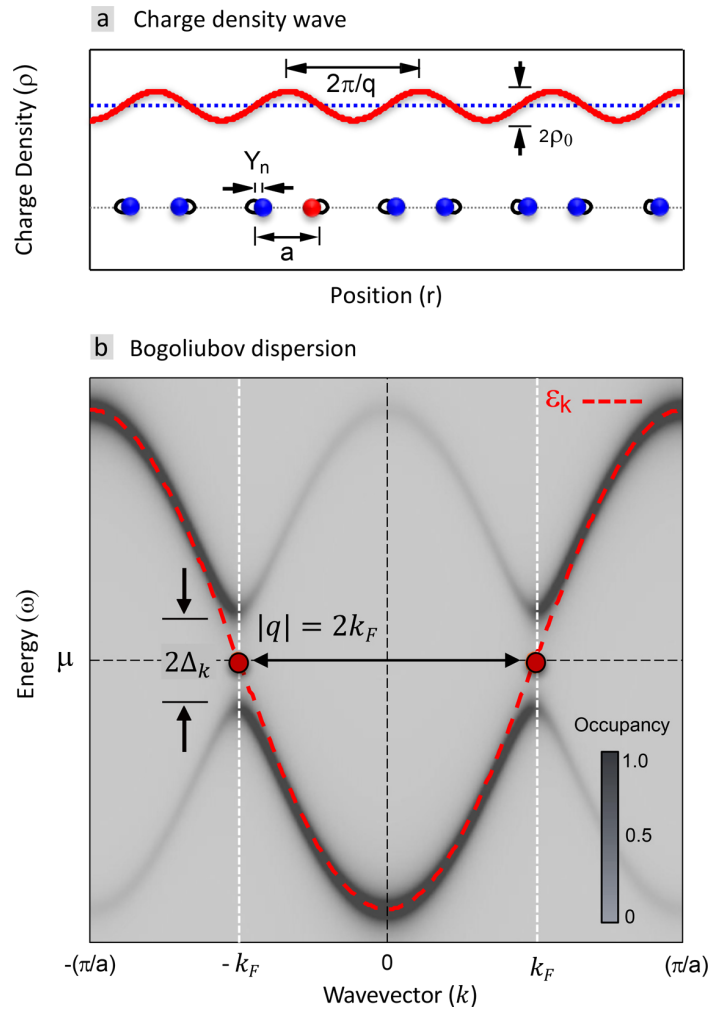


FIGURE 1.3: **Characteristics of the charge density wave (CDW) phase.** (a) A one dimensional chain of atoms subjected to the *Peierls transition*. CDW modulation of the electronic charge distribution is shown with the underlying periodic lattice distortion (PLD) of ion cores. (b) Bogoliubov dispersion of electronic bands. This is for the specific case of  $\mathbf{q} = 2k_F$  (where  $k_F$  is the Fermi momentum). Band dispersion of CDW state is shown in a gray-scale proportional to the electron occupancy while the expected normal state dispersion ( $\epsilon_k$ ) is given by a red dashed line. At the CDW transition, dispersion splits into two branches, and at  $k = \pm k_F$ , they are separated by an interband gap of  $2\Delta_k$ , which is twice of the CDW energy gap.

under the action of the CDW interaction, this electronic state will be coupled to another state with momentum  $\mathbf{k}+\mathbf{q}$ , and thus the dispersion will be modified as [45]:

$$E_{\mathbf{k}} = \frac{1}{2}(\epsilon_{\mathbf{k}} + \epsilon_{\mathbf{k}+\mathbf{q}}) \pm \left[ \frac{1}{4}(\epsilon_{\mathbf{k}} - \epsilon_{\mathbf{k}+\mathbf{q}})^2 + \Delta_{\mathbf{k}}^2 \right]^{\frac{1}{2}} \quad (1.1)$$

where,  $\epsilon_{\mathbf{k}}$  is the dispersion of the normal state as shown by a red dashed line in Fig. 1.3(b), and  $\Delta_{\mathbf{k}} = \Delta_{CDW}(\mathbf{k})$ , which is the CDW energy gap[46]. From the equation 1.1, it is clear that the dispersion will split into two branches ( $\pm$ ), an upper(+) branch and a lower(-) branch, as shown in Fig. 1.3(b). When the momentum  $\mathbf{k}$  associated with an electron is increased from 0, for smaller  $\mathbf{k}$ , its energy will follow the normal dispersion ( $E_{\mathbf{k}} \rightarrow \epsilon_{\mathbf{k}}$ ). But while approaching  $\mathbf{k} \rightarrow (\mathbf{k}+\mathbf{q})$ , electronic energy  $E_{\mathbf{k}}$  will deviate to lower energies in the lower branch, reaching a maximum energy of  $(\epsilon_{\mathbf{k}} - \Delta_{\mathbf{k}})$  which will occur at the momentum  $\mathbf{k}=(\mathbf{k}+\mathbf{q})$ . For the particular example considered, this will occur at the momentum  $k_F$ . On the other hand, the upper(+) branch is the mirror image of the lower(-) branch on the horizontal energy ( $\omega$ ) axis, which drops to a minimum energy of  $(\epsilon_{\mathbf{k}} + \Delta_{\mathbf{k}})$  at same momentum value  $(\mathbf{k}+\mathbf{q})$  as for the lower(-) branch. It can be seen that the interband gap  $= 2\Delta_{\mathbf{k}} = 2\Delta_{CDW}(\mathbf{k})$ . As evident from the Fig. 1.3(b), branches of  $E_{\mathbf{k}}$  do not cross through chemical potential,  $\mu$  (i.e., at  $\omega = 0$ ). Rather, lower(-) and upper(+) branches bend downward and upward at  $\mathbf{k}_F$ , respectively. This bending of the electronic dispersion signifies the electron-hole pairing of the CDW state.

The transition to the CDW phase, much like in superconductivity, is a phenomenon emergent from a symmetry breaking of its core lattice[47]. To characterize the CDW state, a complex order parameter,  $\Psi$  can be defined with a non-zero amplitude and phase

for  $T < T_{CDW}$  [48]. The amplitude of this order parameter is directly proportional to the CDW energy gap,  $\Delta_{CDW}$ . Consider the one-dimensional chain of atoms subjected to Peierls like CDW transition, as depicted in Fig. 1.3(a). The normal state spacial charge density is  $\rho(\mathbf{r})_{avg}$ , which is a constant, and the CDW state charge density is  $\rho(\mathbf{r})$ . The CDW order parameter  $\Psi$  is then  $\rho(\mathbf{r}) - \rho(\mathbf{r})_{avg}$ , which is a complex quantity in general. In the CDW state, when  $T < T_{CDW}$ , the order parameter  $\Psi$  will be a sinusoidal modulation[45]:

$$\rho(\mathbf{r}) = \rho(\mathbf{r})_{avg} + \rho_0 \cos(\mathbf{q}_{CDW} \cdot \mathbf{r} + \phi) \quad (1.2)$$

$$\Psi = \rho(\mathbf{r}) - \rho(\mathbf{r})_{avg} = \frac{2\Delta_{CDW}}{g(|\mathbf{q}|)} \cos(\mathbf{q}_{CDW} \cdot \mathbf{r} + \phi) \quad (1.3)$$

where the parameter  $g(|\mathbf{q}|)$  is the momentum dependent electron-phonon coupling function. It is straightforward to see that the amplitude of the order parameter is directly proportional to the magnitude of the CDW energy gap;  $\rho_0 \propto \Delta_{CDW}$ . The deformation of the underlying lattice can be given as,

$$Y_n = Y_0 \sin(n|\mathbf{q}_{CDW}|a + \phi) \quad (1.4)$$

where,  $n$  is an integer which is the position index of an ion,  $Y_n$  is the deviation of the  $n^{th}$  ion and  $a$  is the lattice constant. Since the order parameter and the lattice deformation are represented by *cosine* and *sine* functions respectively, the periodic lattice distortion(PLD) is out of phase with the charge density wave, as shown in the Fig. 1.3(a).

The formation of CDWs is believed to be related to some of the interesting phenomena observed in condensed matter physics such as the *pseudogap* in high temperature cuprate superconductors [49–51], *enormous mass renormalization* of heavy fermions [52, 53] and *colossal magnetoresistance* in manganite compounds [54, 55]. However, the study of CDW order in these cases is challenging due to the simultaneous occurrence of several different types of interactions in the systems[47]. Therefore, the study of prototype CDW materials such as TMDs is useful since they possess comparatively simpler crystal structures and electronic behaviors.

### 1.1.3 The Formation of Charge Density Waves in Transition Metal Dichalcogenides

The Fig. 1.4 shows the nature of two-dimensional commensurate charge density waves in  $2H - \text{TaSe}_2$  (left column) and  $1T - \text{TaS}_2$  (right column). The formation of the real space super-lattice and the related subdivision of the momentum space is significant.

In the normal state, due to the underlying atomic periodicity, real space lattice has unit cells as indicated in green dashed lines in the Fig. 1.4(a) and (b). The corresponding reciprocal lattices, with Brillouin zones marked in green dashed lines are given in Fig. 1.4(c) and (d) respectively. Consider hexagonal clusters of Ta atoms in  $2H - \text{TaSe}_2$  marked in the Fig. 1.4(a). Upon CDW transition, Ta atoms in the perimeter of the hexagon marked as  $\text{Ta}_b$  (dark gray) would displace toward the Ta atom,  $\text{Ta}_a$  (black) in the center. Similarly, in the case of  $1T - \text{TaS}_2$ , both  $\text{Ta}_b$  (dark gray) and  $\text{Ta}_c$  (light gray) atoms in the perimeter of ‘*star-of-David*’ structures would move toward the  $\text{Ta}_a$  (black) in the center.

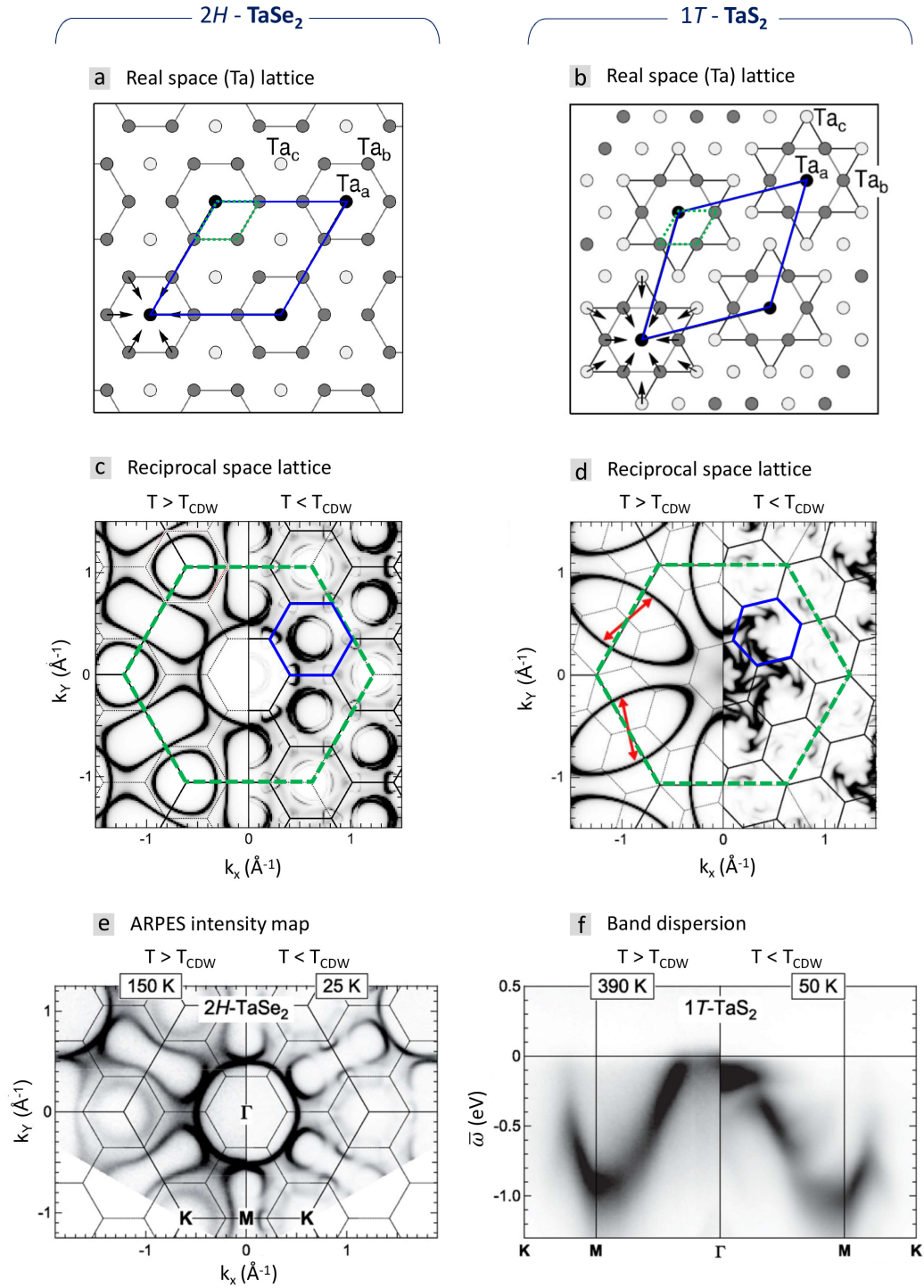


FIGURE 1.4: Normal and CDW states of 2H- and 1T-TMDs. Please see the next page for the details.

**Normal and CDW states of 2H- and 1T-TMDs.**

Continued from the previous page ...

Left side (a) (c) (e) corresponds to 2H – TaSe<sub>2</sub> while right side (b) (d) (f) corresponds to 1T – TaS<sub>2</sub>. **(a, b)** Schematic real space locations of Ta atoms. The arrows indicate in-plane displacements of the Ta atoms from their original positions upon the transition to commensurate CDW state (arrow lengths are not to scale). The Ta atoms at sites labeled ‘a’, ‘b’, and ‘c’ behave differently in the periodic lattice distortion (PLD) patterns. Normal state real space lattice unit cells are indicated in green dashed lines while CDW state super-lattice lattice unit cells are outlined in blue solid lines. **(c, d)** Simulated reciprocal space diagrams for normal ( $T > T_{CDW}$ ) and reconstructed commensurate CDW ( $T < T_{CDW}$ ) phases. Normal state reciprocal lattice unit cells (i.e., 1<sup>st</sup> Brillouin zones) are indicated in green dashed lines while CDW state reciprocal lattice unit cells are outlined in blue solid lines. In (d), The red arrows mark possible nesting vectors. **(e)** Experimental ARPES intensity map of 2H – TaSe<sub>2</sub> for normal and CDW phases, which closely resemble (c). Darker tones represent higher intensity. (ARPES Photon energy,  $h\nu=82$  eV) **(f)** Experimental ARPES band structure of 1T – TaS<sub>2</sub> for normal and CDW phases,  $\bar{\omega}$  is the energy with respect to the Fermi level. Formation of gaps are significant in CDW phase. ( $h\nu=96$  eV) Adapted from [10].

---

This displacement would break the lattice periodicity of the normal state, and a CDW state with a modified lattice periodicity will emerge. The real space unit cell of the CDW state indicated in blue solid lines on the Fig. 1.4(a) and (b), would usually have a larger unit cell with longer spacial periodicity giving rise to a super-lattice. Accordingly, the momentum space will be subdivided into smaller Brillouin zones upon CDW transition. The opening of band gaps in CDW state, as discussed in the section 1.1.2 can be seen on the Fig. 1.4(f) as well.

Out of all the diverse properties and the multitude of layered TMD compounds, the presented studies focus on 2H – TaS<sub>2</sub> which is a prototype material for charge density wave (CDW) behavior, and compare it with two similar candidates, 2H – NbSe<sub>2</sub> and 2H – TaSe<sub>2</sub>. Three compounds 2H – TaS<sub>2</sub>, 2H – NbSe<sub>2</sub> and 2H – TaSe<sub>2</sub> have CDW transition temperatures ( $T_{CDW}$ )  $\sim 75$  K, 33 K and 122 K, respectively [19, 56–58]. Below  $T_{CDW}$ , system enters into an incommensurate CDW order. Further, in the case of 2H – TaSe<sub>2</sub>, the system goes from an incommensurate to a commensurate CDW order below  $\sim$

90 K. Phase competition is also significant in TMDs, just as in high temperature cuprate superconductors. For  $2H - \text{TaS}_2$ , CDW order coexists with superconductivity[19–21] below 0.8 K. In this incommensurate CDW state under study, the system shows a hexagonal symmetry[59, 60] characterized by a CDW wave vector  $\mathbf{q}_{CDW}$  having the magnitude[45]:

$$|\mathbf{q}_{CDW}| = (1 - \delta) \frac{a^*}{3} \quad (1.5)$$

where  $a^* = 4\pi/\sqrt{3}a$ , with  $a$  being the lattice constant. and  $\delta \sim 0.02$ .

## 1.2 Thermoelectric Performance of Lead Chalcogenides

### 1.2.1 Thermoelectric Effect

In 1794, in the process of testing and eventually disproving the concept of Luigi Galvani’s *animal electricity*, Alessandro Volta observed that if a temperature difference exists between the ends of an iron rod, it could excite spasms of a frog’s leg[61, 62]. Then in 1821, Thomas Johann Seebeck independently rediscovered the phenomenon of generating electricity using a temperature gradient. In his experiment, a closed loop formed by wires of two different metals joined together at either end was observed to deflect a compass needle if there was a temperature gradient between the joints[63]. Later, Hans Christian Ørsted established the term ‘*thermoelectricity*’ for this phenomenon [64]. Moreover, in 1950s Abram Ioffe found that doped semiconductors could demonstrate a much larger thermoelectric effect[65].

The *Fermi level* of metal is the highest occupied energy level in the conduction band at a given temperature. When two metals are placed in electrical contact, electrons flow out of the metal with a higher Fermi level to the metal with lower Fermi level in order to minimize the overall energy of the system. This flow, driven by the electrostatic potential difference due to the differing Fermi levels, will result in a current until the Fermi levels of both metals become equal. If a closed circuit like the bi-metal loop in the above mentioned Seebeck's experiment is constructed, no net current will be observed as the two contact potentials will be equal in magnitude and opposite in direction at either joint. However, if the joints are at different temperatures, since the temperature dependence of Fermi levels of two different metals is likely to be different, the contact potentials will not be equal anymore. Therefore, a current will start to flow.

### 1.2.1.1 Seebeck Effect

The Seebeck effect is the above described phenomenon of observing a current flow by exerting a temperature difference between two bi-metallic junctions. The electric potential gradient,  $\nabla V$  created by a temperature gradient,  $\nabla T$  can be related as:

$$\nabla V = -S(T)\nabla T \quad (1.6)$$

The temperature dependent coefficient  $S(T)$ , which is a material property, is known as the *Seebeck coefficient* or the *thermopower*. It is measured in Volts per Kelvin (V/K).

In Fig.1.5 (a) the Seebeck effect is illustrated for doped semiconductor junctions. When the bottom contact is heated, the thermal and charge carriers, the electrons in the  $n$ -doped semiconductor, and the holes in the  $p$ -doped semiconductor, moves upwards. This

motion of electrons and holes manifests in the nominal electric current across the light bulb in the direction indicated.

### 1.2.1.2 Peltier Effect

In 1834, Jean Charles Athanase Peltier passed an electric current through a similar bi-metallic loop circuit and observed the absorption of heat at one junction and rejection at the other junction [66]. This is the converse of the Seebeck effect. The rate of heat generation due to the Peltier effect is:

$$\frac{\Delta Q}{\Delta t} = (\Pi_A - \Pi_B)I \quad (1.7)$$

Where  $I$  is the current passed and  $\Pi_A$  and  $\Pi_B$  are *Peltier coefficients* of respective material.

In the Fig.1.5 (b) the Peltier cooling is illustrated for doped semiconductor junctions. When the positive terminal of the battery is connected to the bottom contact of an  $n$ -doped semiconductor, electrons from the top side will be drifted down. Similarly, since the negative terminal of the battery is connected to the bottom contact of the  $p$ -doped semiconductor, holes from the top side will also be drifted down. These electron and hole movements result in a nominal electric current as shown by the arrows. Notice how all the thermal carriers (electrons and holes) are moving downwards while extracting heat from the top surface and rejecting it at the bottom surfaces. Thus, a persistent current will effectively cool the top surface. Further, it can be seen that the thermoelectric heating is also possible by flipping the utilized surfaces.

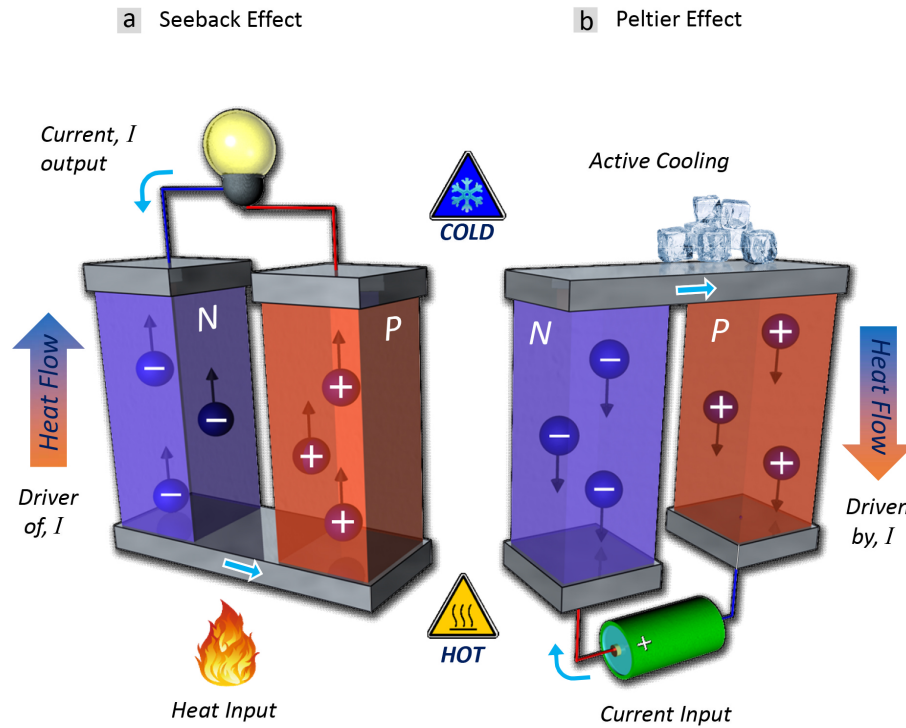


FIGURE 1.5: Seebeck and Peltier effects.

(a) Seebeck effect: Heating a junction of  $n$ - and  $p$ -doped semiconductor drives a current through relatively cold junction, which is the light bulb. This is an example of thermocurrent generation. (b) Peltier effect: Driving a current through a loop consisting of  $n$ - and  $p$ -doped semiconductors exerts a temperature difference between either end. Shown is an example of thermoelectric cooling.

The Seebeck and Peltier coefficients are related via:

$$\Pi = ST \quad (1.8)$$

### 1.2.1.3 Thomson Effect

From equation 1.6, where the Seebeck coefficient is defined, it is apparent that the Seebeck coefficient will change along the circuit due to the spatial temperature gradient. This will result in a continuously cascading Peltier effect. William Thomson (Lord Kelvin) predicted this effect and then experimentally proved it in 1851 [67].

#### 1.2.1.4 Thermoelectric Figure of Merit

The performance of a thermoelectric material is characterized by a dimensionless quantity  $ZT$  commonly known as the *figure of merit*, such that,

$$ZT = \frac{\sigma}{\kappa} S^2 T \quad (1.9)$$

where  $S$  is the Seebeck Coefficient,  $\sigma$  is the electrical conductivity, and  $\kappa$  is the thermal conductivity [68]. In order to obtain a higher figure of merit, higher electrical conductivity and lower thermal conductivity are required simultaneously. This is not trivially accomplished because charge carriers (electrons and holes) usually act as thermal carriers as well. Since all these physical quantities of a material are intimately related to its electronic structure, a detailed knowledge of it is crucial toward formulating strategies for optimization of  $ZT$ . Being a simultaneous probe for the energy and momentum of the occupied electronic states in a solid, ARPES is ideally suited for this task [69].

#### 1.2.2 Lead Chalcogenides

Lead chalcogenides,  $\text{PbQ}$  ( $\text{Q}=\text{Te}$ ,  $\text{Se}$ , and  $\text{S}$ ) are canonical systems for fundamental studies of thermoelectric properties [70–72] due to their unique electronic structure. Recently, new methods such as ‘all scale hierarchical architecture processing’ [73–75] have lead to significant advancements in their thermoelectric performance. For instance,  $p$ -type nanostructured  $\text{PbTe}$  holds a performance record for high temperature energy conversion [76–78]. Despite being studied for decades, research involving  $\text{PbQ}$  is a hot field. One such example is the recently discovered appearance of local  $\text{Pb}$  off-centering dipoles on warming without a structural transition in  $\text{PbTe}$  [79, 80]. Moreover, these

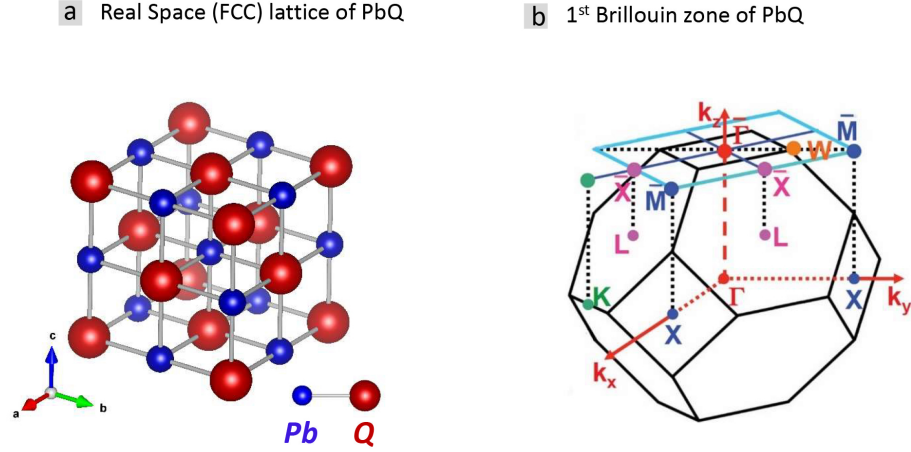


FIGURE 1.6: **Real and reciprocal space structures of Lead chalcogenides.** (a) Real space lattice of Lead Chalcogenides are Face Centered Cubic (FCC). (b) Since the reciprocal lattice is Body Centered Cubic (BCC), the 1<sup>st</sup> Brillouin zone is a *truncated octahedron*. High symmetry points and their projection on to (001) crystallographic plane are as marked[91].

systems have recently been shown to host various novel quantum states of matter. For instance,  $\text{Pb}_{1-x}\text{Sn}_x\text{Se}$  and  $\text{Pb}_{1-x}\text{Sn}_x\text{Te}$  are shown to be topological crystalline insulators [81–89], while superconductivity along with normal state charge Kondo anomaly occurs at Tl doped PbTe [90].

Lead chalcogenides are three-dimensional materials with Face Centered Cubic (FCC) real space lattice as shown in the Fig.1.6(a). The reciprocal lattice is Body Centered Cubic (BCC) with the 1<sup>st</sup> Brillouin zone of *truncated octahedron* shape. The Fig.1.6(b) shows this Brillouin zone with its key symmetry points ( $\Gamma$ , L, X, K, and W) marked. For the ARPES experiments presented in this dissertation, PbQ samples were preferentially cleaved along (001) plane, and hence, the relevant two-dimensional projection of some useful symmetry points ( $\bar{\Gamma}$ ,  $\bar{X}$ ,  $\bar{M}$ ) are also marked for reference.

### 1.3 Organization of the Dissertation

In Chapter 1, material systems, which are transition metal dichalcogenides (TMD) and Lead chalcogenides (PbQ) under study are covered. Brief overviews of physical phenomena, namely, charge density waves (CDW) and the thermometric effect were presented as well.

The experimental techniques used will be outlined in Chapter 2. Both energetics and kinematics of photoemission will be discussed in a progressive cascade of approximations in order to outline the general interpretation of Angle Resolved Photoemission Spectroscopy (ARPES). The spectral function formalism of ARPES data will then be presented, and the concept of self-energy will be introduced in brief. Standard representations of ARPES data and a short overview of general data conditioning methods will follow. Technical details of the presented experiments will complete this chapter.

The incommensurate charge density wave phase of  $2H$  polytype of transition metal dichalcogenides will be studied in both chapters 3 and 4. Via the analysis of the low energy electronic structure of  $2H - TaS_2$  and  $2H - NbSe_2$ , the suitability of ‘Fermi surface nesting’ as the underlying CDW mechanism will be discussed. Next, the momentum and temperature dependence of the CDW energy gap will be studied and then the evidence for *pseudogap* will be presented and justified. Chapter 3 is mostly based on the articles: *Orbital selectivity causing anisotropy and particle-hole asymmetry in the charge density wave gap of  $2H - TaS_2$* , Phys. Rev. B 96, 125103 (2017) [92] and *Spectroscopic study of the charge density wave order in  $2H - TaS_2$* , Proc. SPIE (Spintronics X), 10357:8 (2017)[45].

Furthermore, the compound  $2H - TaS_2$  will be further studied in Chapter 4 in terms of self-energy analysis. Both momentum and temperature dependent data analysis will be used in order to establish underlying collective modes which result in electronic band renormalization as phonons. The study presented in Chapter 4 is mostly based on the publication: *Spectroscopic signature of moment dependent electron-phonon coupling in  $2H - TaS_2$* , J. Mater. Chem. C, 5:11310 (2017)[47].

The remarkable increase in the thermoelectric performance of Lead chalcogenides at elevated temperatures will be analyzed in Chapter 5. Temperature dependent ARPES analysis will be used to justify the reason behind the outstanding thermoelectric performance as the temperature dependent convergence of light and heavy hole valence bands. Chapter 5 is mostly based on the article: *Spectroscopic evidence for temperature-dependent convergence of light- and heavy-hole valence bands of  $PbQ$  ( $Q = Te, Se, S$ )*, EPL,117(2017) 27006 [91].

Finally, in Chapter 6, the results for both studies, charge density waves in transition metal dichalcogenides and thermoelectric performance of Lead chalcogenides, will be summarized and final conclusions will be drawn.

---

## Chapter 2

# Experimental Techniques

Angle resolved photoemission spectroscopy (ARPES) was the primary experimental probe used in the studies presented in this dissertation. A brief discussion of the ARPES technique, representation of ARPES data and a general overview of some data analysis techniques will be given in this chapter.

### 2.1 Angle Resolved Photoemission Spectroscopy (ARPES)

#### 2.1.1 The Photoelectric Effect

The photoelectric effect is the phenomenon of the emission of electrons when light is incident upon a material. This was first discovered by Heinrich Hertz [69, 93] in 1887 by means of irradiating electrodes with ultraviolet light. However, this low energy light–matter interaction occurred only above a certain cut-off frequency and could not be explained with classical physics. Later, by extending the idea of the quantization of electromagnetic energy put forward by Max planck in 1900, Albert Einstein was able to construct a successful quantum mechanical description of the photoelectric effect in 1905 [93]. In 1914, Robert Millikan was able to use this phenomenon to experimentally

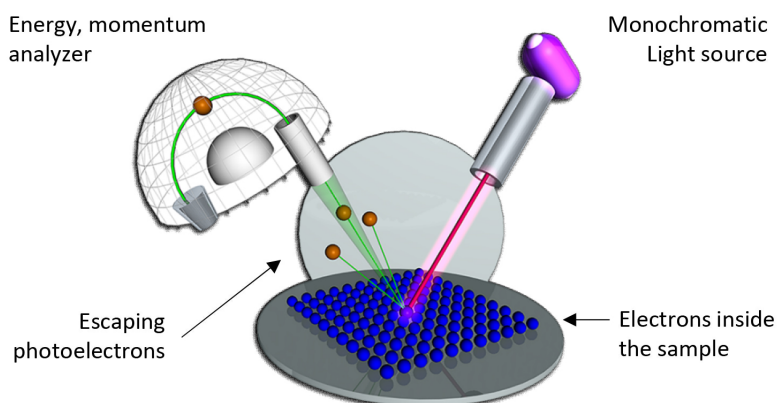
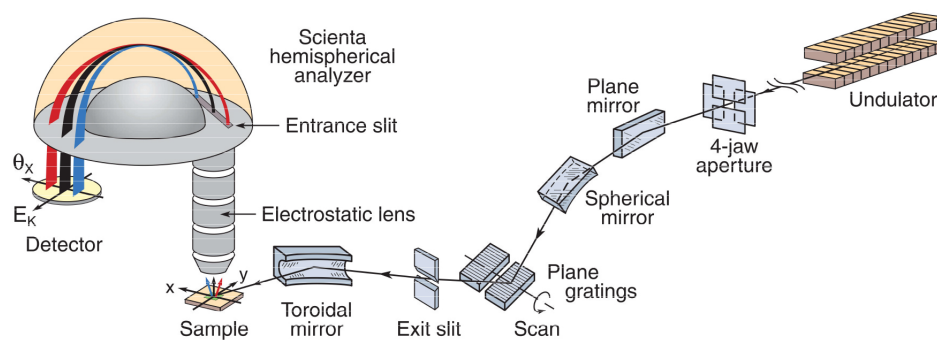
**a** Concept of ARPES**b** ARPES setup in a synchrotron beamline

FIGURE 2.1: **The concept of angle resolved photoemission spectroscopy (ARPES).**

(a) The basic concept of ARPES: incident light from a monochromatic source will eject photoelectrons from the sample, which can then be captured and analyzed in terms of energy and momentum in order to probe the electronic band structure inside the sample. (b) Experimental realization of an ARPES setup in a synchrotron light source.[96]

discover the elementary electric charge of the electron via his famous ‘oil drop experiment’. Albert Einstein and Robert Millikan were awarded Nobel prizes for physics in 1921[94] and 1923[95], respectively. Modern experimental techniques which come under the broad category of *Photoemission Spectroscopy* (PES), are based on this photoelectric effect.

### 2.1.2 Energetics of Photoemission

Einstein's law of photoelectric effect is a specific statement of the conservation of energy:

$$E_{kin}^{vac} = h\nu - E_B - \phi \quad (2.1)$$

where,  $E_{kin}^{vac}$  is the kinetic energy of the emitted photoelectron,  $h\nu$  is the quantized energy of the incident photon,  $E_B$  is the binding energy of the electron (with respect to the chemical potential,  $\mu$ ) and  $\phi$  is the work function of the material. In other words, the photoemission in its simplest picture is a process where a light photon with a specific energy ( $h\nu$ ) will spend some energy ( $E_B$ ) to remove an electron from its state and another portion of energy to overcome the surface energy barrier (work function,  $\phi$ ) and the ejected electron will carry the remainder of the energy ( $E_{kin}^{vac}$ ). Energy relationships between the states inside the material and photoelectric energies detected are illustrated in the Fig. 2.2.

$E_{kin}^{vac}$  is stated with respect to the vacuum energy,  $E_{vac}$  while the work function for a material is defined as the energy required by an electron at the chemical potential (Fermi level) to escape the material and reach the vacuum:

$$\phi = E_{vac} - \mu \quad (2.2)$$

work function ( $\sim 4$  to  $5$  eV in metal) acts as a surface potential barrier which prevents valence electrons from escaping the material[96].

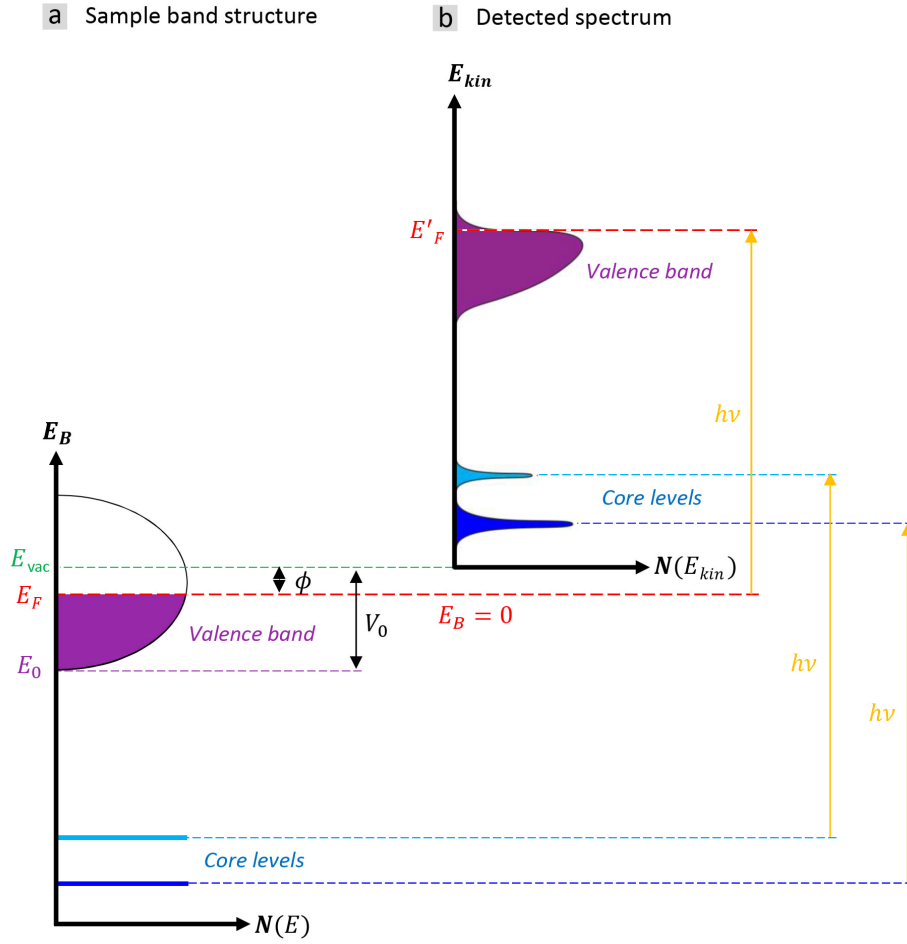


FIGURE 2.2: **Energetics of photoemission spectroscopy.**

Plots of Energy vs. Density of States ( $N$ ) for electronics; (a) In the band structure inside the sample, and (b) in the detected kinetic energy ( $E_{kin}$ ) spectrum.  $E_{vac}$  is the vacuum level,  $E_F$  denotes the Fermi level,  $E_0$  is the valence band bottom. Both the work function,  $\phi$  and the inner potential,  $V_0$  are marked.  $h\nu$  is the energy of the incident photons. For the band structure (a), the convenient reference for binding energy ( $E_B=0$ ) is  $E_F$  (the red horizontal dashed line) whereas for the photoemission spectrum (b), the ( $E_{kin}=0$ ) is  $E_{vac}$  (the green horizontal dashed line). Both spectra are related to each other with the photoelectric relationship,  $E_{kin} = h\nu - |E_B| - \phi$ . Adapted from [69, 96].

Above parameters,  $E_{kin}^{vac}$  or  $E_{vac}$  can neither be directly measurable nor of experimental interest. However, in practical experimental setups, the sample and the electron energy detector are mutually connected to share a common potential, hence what measured is  $E_{kin}^\mu$ , which is the kinetic energy of the photoelectron with respect to the chemical potential[97]. Therefore, the measured electronic energy can be related to incident

photoenergy and the electronic binding energy as:

$$E_{kin}^{\mu} = h\nu - E_B \quad (2.3)$$

Since the incident photoenergy is known, the detected electronic energy can be used to probe the electronic information inside the sample. This is the basis of photoemission spectroscopy (PES).

ARPES incorporates the angle resolution to the above explained photoemission spectroscopy, by means which the momentum information is also extracted in addition to the energy information as elaborated below. A conceptual illustration of ARPES is given in the Fig. 2.1.

### 2.1.3 Visualization of the Photoemission Process

For any approach in explaining the photoemission process, the initial state of the electron should be a Bloch state in the bulk. Via photoemission, this electron gets excited to a free-electron plain wave final state. There are two main perspectives for visualizing this transformation [96].

- One-step model - A quantum mechanical picture.
- Three-step model - A classical phenomenological model with the ‘sudden’ approximation.

These models are illustrated side by side in the Fig. 2.3

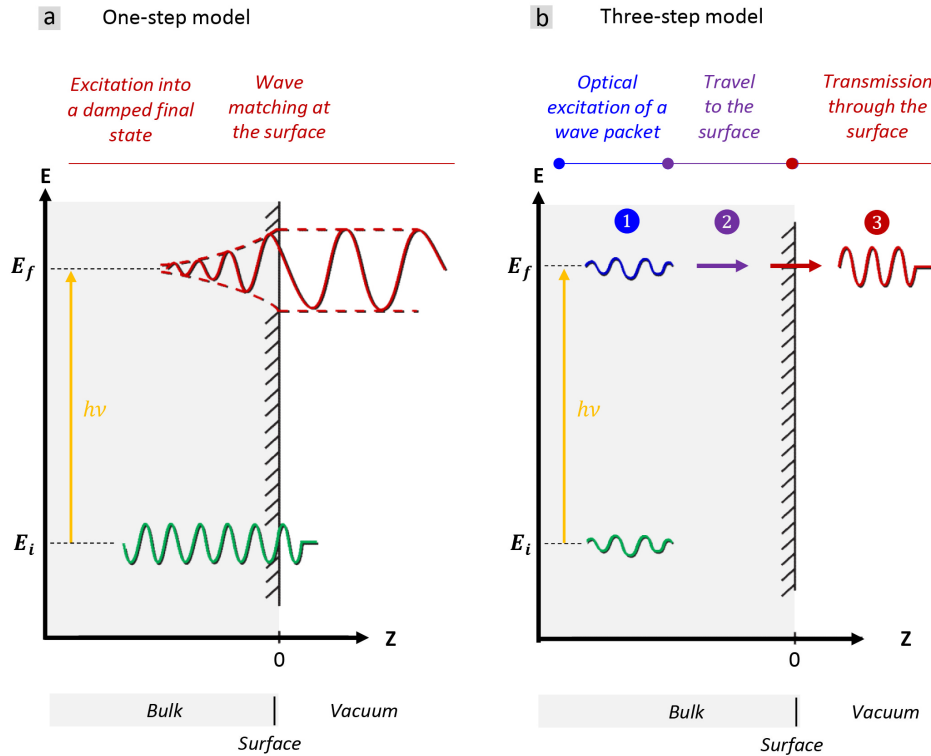


FIGURE 2.3: **One- and three- step models of photoemission.**

(a) The quantum mechanical one-step model explains the photoemission process as an instantaneous transition from an initial state to a final state. (b) The phenomenological three-step model, which visualizes the photoemission in three successive steps under the *sudden* approximation: **1.** Photoexcitation of a bulk initial electronic state to a bulk final state. **2.** Traveling of the excited electron to the sample surface. **3.** Escape of the photoelectron into the vacuum. Adapted from [69].

### 2.1.3.1 One-Step Model

This is a quantum mechanical description of the photoemission, as an instantaneous single-step process. This approach is illustrated in the Fig. 2.3(a) and a simple description of the model would be as follows.

- The initial and final states involved are many body wavefunctions,  $\Psi^N$ , which obey boundary conditions at the surface of the crystal.
- The initial state,  $\Psi_i^N$ , is one of the possible N-electron eigenstates of the semi-infinite crystal.

- The final state,  $\Psi_f^N$ , has two components, one of possible (N-1) electron eigenstates of the semi infinite crystal which is ionized, -and- a component with a propagating plane wave in the vacuum which represents an ejected photoelectron. The latter should have a finite amplitude inside the crystal with some overlap with the initial state ( $\Psi_i^N$ ) as required by quantum mechanics.

The process of photoemission in this one step model is an optical transition between above specified initial and final many-body states. The transition probability is given by the Fermi's golden rule:

$$w_{fi} = \frac{2\pi}{\hbar} |\langle \Psi_f^N | H_{int}^{one-step} | \Psi_i^N \rangle|^2 \delta(E_f^N - E_i^N - h\nu) \quad (2.4)$$

where  $H_{int}^{one-step}$ ,  $E_f^N$ , and  $E_i^N$  are the interaction Hamiltonian, the final state energy, and the initial state energy, respectively.

Requirements for such a transition are, the finite overlap between initial and final states, and the conservation of the energy as well as the momentum within the whole system consisting of the crystal, photoelectron, and the incoming photon.

$$E_f^N - E_i^N = h\nu \quad (2.5)$$

$$\mathbf{k}_f^N - \mathbf{k}_i^N = \mathbf{k}_{h\nu} \quad (2.6)$$

The  $\mathbf{k}_{h\nu}$  here is the incoming photon momentum.

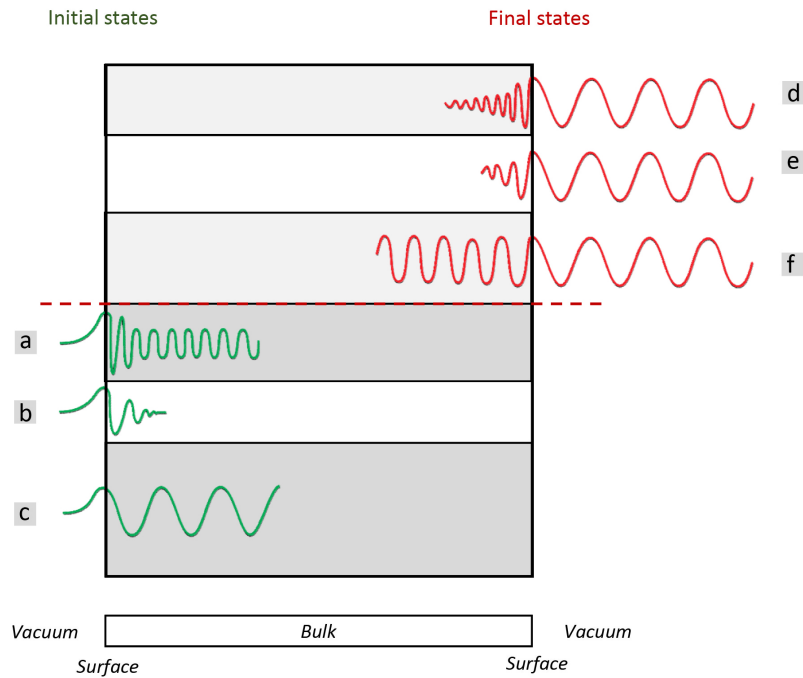


FIGURE 2.4: **Initial and final eigenstates for a semi-infinite crystal.** [69, 113] **Initial states:** (a) Surface resonance. (b) In-gap surface Shockley state (in the gap of the bulk band structure). (c) Bulk Bloch initial state. **Final states:** (d) Surface resonance. (e) In-gap evanescent state. (f) Bulk Bloch final state. The red dashed horizontal line marks the chemical potential. Note, the initial states (left) have decaying components in the vacuum while final states (right) have propagating vacuum components.

In this one step model, the absorption of the photon, removal of an electron, and the detection of the electron are treated as a single, instantaneous and coherent quantum mechanical process [96, 98–112]. However, in this rigorous many-body treatment, the bulk, surface, and vacuum of the crystal should be described in the Hamiltonian  $H_{int}^{one-step}$ , which implies that not only bulk Bloch states, but also surface and evanescent states as well as surface resonances should be considered (see Fig.2.4). Due to this complexity, a simpler approach known as the ‘three-step model’ is widely used in the literature in explaining the phenomenon of photoemission[96].

### 2.1.3.2 Three-Step Model

Three-step model is a classical phenomenological approach with many simplifications but is proven to be successful in explaining most practical photoemission data[103, 114, 115]. This approach is as illustrated in the Fig. 2.3(b), where the photoemission process is explained as a cascade of three mutually exclusive and sequential events:

1. Optical excitation of the electron in the bulk by means of an incident photon.
2. Traverse of this excited electron to the surface.
3. Ejection of this electron (photoelectron) into the vacuum.

The resultant photoemission intensity is the product of probabilities of these three independent steps.

$$\text{Photoemission intensity} \propto \left\{ \begin{array}{l} \text{Total probability of} \\ \text{an optical transition} \end{array} \right\} \left\{ \begin{array}{l} \text{probability for} \\ \text{non-scattering} \\ \text{of traveling} \\ \text{electrons} \end{array} \right\} \left\{ \begin{array}{l} \text{Transmission} \\ \text{probability} \\ \text{through surface} \\ \text{potential barrier} \end{array} \right\}$$

The probability of the step (1), photoexcitation, is determined by the intrinsic electronic structure of the crystal which is the information needed. Therefore, the general objective of ARPES or any other photoelectron spectroscopy (PES) data analysis procedure is to isolate the contribution from this step, from the observed photoemission intensity. This probability can be determined using the Fermi's golden rule:

$$w_{fi} = \frac{2\pi}{\hbar} |\langle \Psi_f^N | H_{int}^{dipole} | \Psi_i^N \rangle|^2 \delta(E_f^N - E_i^N - h\nu) \quad (2.7)$$

where  $w_{fi}$  gives the transition probability from an N-electron initial state,  $\Psi_i^N$  to an N-electron final state  $\Psi_f^N$ .

$$E_f^N = E_f^{N-1} + E_{kin} \quad (2.8)$$

$$E_i^N - E_i^{N-1} + E_B^k \quad (2.9)$$

Here,  $E_B^k$  is the binding energy of the photoexcited electron with kinetic energy  $E_{kin}$  and crystal momentum  $\mathbf{k}$ .

From the perturbation theory, the total Hamiltonian is:

$$H_{total} = \frac{1}{2m}(\mathbf{p})^2 + \frac{1}{2m} \left(\frac{e}{c}\right) (\mathbf{A} \cdot \mathbf{p} + \mathbf{p} \cdot \mathbf{A}) + \frac{1}{2m} \left(\frac{e}{c}\right)^2 (\mathbf{A})^2 \quad (2.10)$$

where,  $\mathbf{A}$  is the magnetic vector potential and  $\mathbf{p}$  is the electronic momentum operator. Note that a gauge choice of which electric scalar potential  $\Phi = 0$  has been made. The first term here is just  $H_0$ , and the third term  $\sim \mathbf{A}^2$  describes non-linear interactions which can be ignored in this context.

By utilizing the commutator relationship  $[\mathbf{p}, \mathbf{A}] = -i\hbar\nabla \cdot \mathbf{A}$  and then, the *dipole approximation* which means the variation of the vector potential,  $\mathbf{A}$  is negligible over atomic dimensions (i.e.,  $\nabla \cdot \mathbf{A} = 0$ ), this interaction Hamiltonian in its simpler form is:

$$H_{int}^{dipole} = \frac{1}{2m} \left(\frac{e}{c}\right) (\mathbf{A} \cdot \mathbf{p} + \mathbf{p} \cdot \mathbf{A}) = \left(\frac{e}{mc}\right) \mathbf{A} \cdot \mathbf{p} \quad (2.11)$$

Step (2) involves the probability for an excited electron to travel to the crystal surface without losing its energy or momentum by means of scattering. This can be understood in terms of the effective mean free path of an electron in the system under study. The inelastic scattering processes would result in a continuous background signal which will be subtracted before data analysis. The probability of these stray processes would also determine the surface sensitivity of photoemission [96].

Subsequent to the above two steps, the electron must escape to the vacuum by surpassing the surface potential barrier, characterized by the work function. It can be seen that an excited electron must pay an energy cost, in step (1) against the electron binding energy  $E_0$  and in step (3) against the work function,  $\phi$ . So, a condition for photoemission can be drawn as,

$$\frac{\hbar^2 \mathbf{k}_\perp^2}{2m} \geq |E_0| + \phi \quad (2.12)$$

where  $\mathbf{k}_\perp$  is the component of the electron crystal momentum, perpendicular to the surface.

### 2.1.3.3 The Sudden Approximation

The next step in simplifying the equation 2.7 would be to factorize the wavefunctions into a photoexcited electron component -and- to another component describing (N-1) remaining electrons. Note that a similar separation of energies has been trivially done in equations 2.8 and 2.9. This would not be possible in a general case where the subsequent relaxation of the system, followed by the photoexcitation will result in

multiple possibilities of complex post-collisional interactions between the excited electron and the rest of (N-1) electrons.

To overcome these complications, assuming sufficiently high incident photon energy, the *sudden approximation* is adopted where the excited electron is considered to be instantaneously removed from the crystal with zero possibility of interaction. This follows an instantaneous and discontinuous change in the effective potential of the system.

Note, on the other hand, in the *adiabatic limit* where low kinetic energy photoelectrons are analyzed, the escape time will be significant compared to the system relaxation time. In such a scenario, this factorization approach would fail, and an intricate treatment of the screening effect should be utilized[96, 116].

Under this sudden approximation, the final state of the system can be factorized as:

$$\Psi_f^N = \mathcal{A}\phi_f^{\mathbf{k}}\Psi_f^{N-1} \quad (2.13)$$

Here, the purpose of the operator  $\mathcal{A}$  is to antisymmetrize the N-electron wavefunction in order to satisfy the *Pauli's exclusion principle*. The wavefunction  $\phi_f^{\mathbf{k}}$  represents a photoexcited electron with a momentum,  $\mathbf{k}$  while  $\Psi_f^{N-1}$  is the excited final state of the remaining (N-1) electron system.

The state  $\Psi_f^{N-1}$  can be expressed to have the eigenfunction  $\Psi_m^{N-1}$  with eigenenergy  $E_m^{N-1}$ , and the total transition probability,  $w_{if}$  should then be the sum over all such possible excited states characterized by  $m$ .

### 2.1.3.4 Photoemission Intensity

Assume the initial state of this fermionic system is a single *Slater determinant* under the *Hartree-Fock formalism*,

$$\Psi_i^N = \mathcal{A} \phi_i^{\mathbf{k}} \Psi_i^{N-1} \quad (2.14)$$

Just like equation 2.13 above, this is an antisymmetrized, factorized product of a single electron orbital component,  $\phi_i^{\mathbf{k}}$  and the remaining (N-1) particle system as a whole ( $\Psi_i^{N-1}$ ). This factorization is simple enough to move on with the treatment, but it should be noted that, the rest of the system is better modeled as:

$$\Psi_i^{N-1} = c_{\mathbf{k}} \Psi_i^N \quad (2.15)$$

where  $c_{\mathbf{k}}$  is the quantum mechanical annihilation operator for an electron with momentum  $\mathbf{k}$ . Also note that the  $\Psi_i^{N-1}$  representing the rest of the system is not an eigenstate of an (N-1) particle Hamiltonian, rather the mere remnant of the previous N-particle wavefunction subsequent to the removal of a photoelectron.

With these simplifications performed under due approximations stated above, the matrix element of the Fermi's golden rule in the equation 2.7 can be factorized as,

$$\langle \Psi_f^N | H_{int}^{dipole} | \Psi_i^N \rangle = \langle \phi_f^{\mathbf{k}} | H_{int}^{dipole} | \phi_i^{\mathbf{k}} \rangle \langle \Psi_m^{N-1} | \Psi_i^{N-1} \rangle \quad (2.16)$$

With the one-electron dipole matrix element:

$$M_{f,i}^{\mathbf{k}} = \langle \phi_f^{\mathbf{k}} | H_{int}^{dipole} | \phi_i^{\mathbf{k}} \rangle \quad (2.17)$$

and the coefficient:

$$c_{m,i} = \langle \Psi_m^{N-1} | \Psi_i^{N-1} \rangle \quad (2.18)$$

which is the overlap integral for remaining (N-1) electrons in the system. The probability that the removal of an electron from state  $i$  will leave the (N-1) particle system in the excited state  $m$  will then be  $|c_{m,i}|^2$ .

By substituting these to the equation 2.7, the photoemission intensity due to one such possible final state  $f = m$  can be found as,

$$w_{fi} = \frac{2\pi}{\hbar} |\langle \phi_f^{\mathbf{k}} | H_{int}^{dipole} | \phi_i^{\mathbf{k}} \rangle|^2 |\langle \Psi_{f=m}^{N-1} | \Psi_i^{N-1} \rangle|^2 \delta(E_f^N - E_i^N - h\nu) \quad (2.19)$$

$$w_{fi} = |M_{f,i}^{\mathbf{k}}|^2 |c_{f=m,i}|^2 \delta(E_f^N - E_i^N - h\nu) \quad (2.20)$$

The total photoemission intensity, as a function of  $E_{kin}$  at a momentum  $\mathbf{k}$ , over all the final states with all possible  $m$  values is then,

$$I(E_{kin}, \mathbf{k}) = \sum_{f,i} w_{fi} \quad (2.21)$$

and finally,

$$I(E_{kin}, \mathbf{k}) \propto \sum_{f,i} |M_{f,i}^{\mathbf{k}}|^2 \sum_m |c_{f=m,i}|^2 \delta(E_{kin} + E_f^N - E_i^N - h\nu) \quad (2.22)$$

For a non-interacting electronic system, for a particulate  $m = m_0$ ; if  $\Psi_i^{N-1} = \Psi_{m_0}^{N-1}$  occurs and the transition is allowed (i.e.,  $M_{f,i}^{\mathbf{k}} \neq 0$ ), the relevant probability becomes  $|c_{m_0,i}|^2 = 1$  while other  $c_{m \neq m_0,i}$  coefficients are zero. In such a non interacting case, the theoretical ARPES spectrum will be a single well-defined delta function at the Hartree–Fock orbital energy  $E_B^{\mathbf{k}} = -\epsilon_{\mathbf{k}}$ . This is illustrated on the Fig. 2.5(a). On the other hand, in a strongly correlated system, even the removal of a single electron would lead  $\Psi_i^{N-1}$  to overlap many eigenstates ( $\Psi_m^{N-1}$ ), due to significant changes in effective potential. The Fig. 2.5(b) shows such an example in the context of a *Fermi liquid system*. [96]

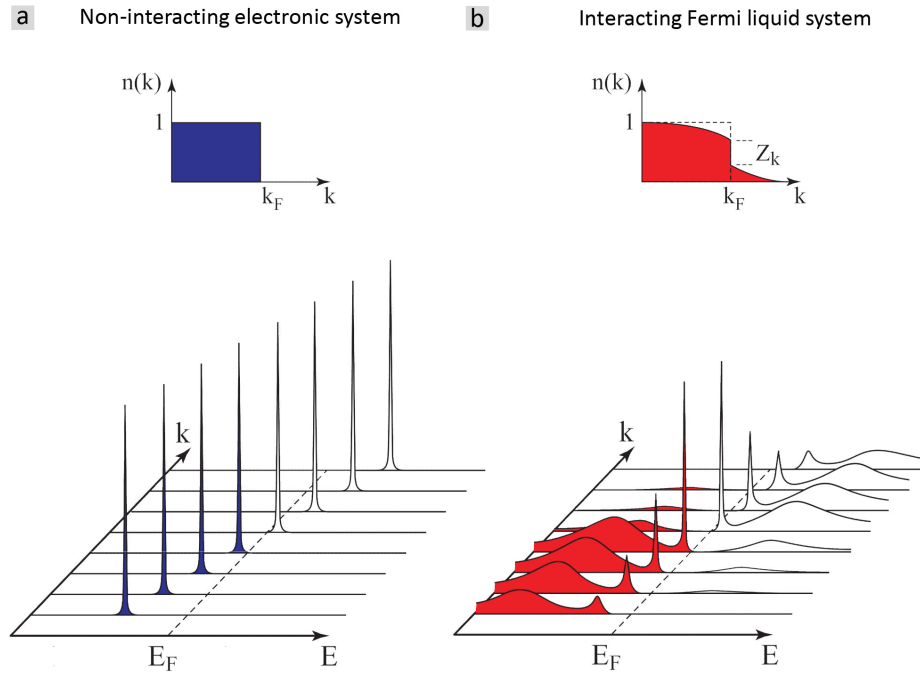


FIGURE 2.5: **Schematic photoemission spectra for interacting and non-interacting electronic systems.** [96]

Ground-state ( $T = 0$  K) momentum distribution functions  $n(\mathbf{k})$  (top) and theoretical photoemission spectra for; (a) A non-interacting electronic system, with a single energy band dispersing across the Fermi level. (b) An interacting Fermi liquid system.

### 2.1.4 Kinematics of Photoemission

Upon the incident of photons with energy  $h\nu$ , photoelectrons are ejected into the vacuum and by detecting these photoelectrons with an electron energy analyzer with a known acceptance angle, their kinetic energy  $E_{kin}$  can be determined for given emission direction. Energetics of this photoemission process was discussed in the section 2.1.2. In addition, ARPES utilizes the ability of angle specificity of the detector to acquire momentum (or wave vector) information as well. The magnitude of the photoelectron momentum measured in the vacuum is:

$$K = |\mathbf{K}| = \frac{\mathbf{p}}{\hbar} = \frac{1}{\hbar} \sqrt{2mE_{kin}} \quad (2.23)$$

Note, from here onward, the upper case  $\mathbf{K}$  notation will be used in referring to the photoelectron momenta measured in the vacuum while the lower case  $\mathbf{k}$  notation is being used for crystal momenta inside the solid. The vector  $\mathbf{K}$  can be resolved into two convenient components as follows.

Components parallel to the sample surface:

$$\mathbf{K}_{\parallel} = \mathbf{K}_x + \mathbf{K}_y = K_x \hat{e}_x + K_y \hat{e}_y \quad (2.24)$$

The component perpendicular to the sample surface:

$$\mathbf{K}_{\perp} = \mathbf{K}_z = K_z \hat{e}_z \quad (2.25)$$

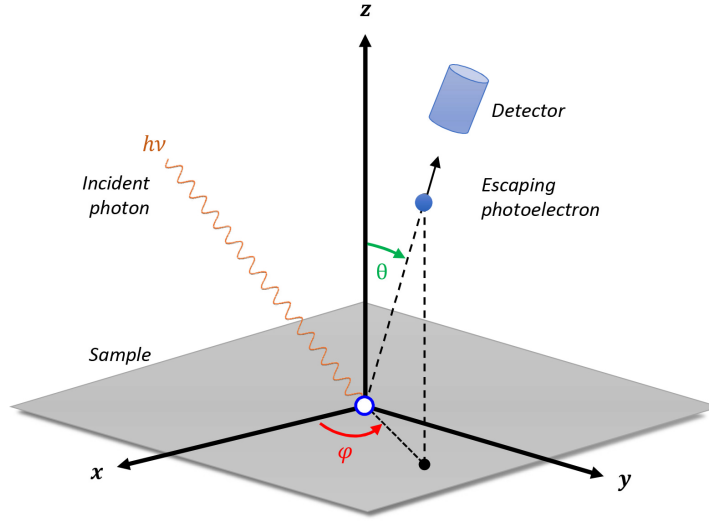


FIGURE 2.6: **The geometry of angle resolved photoemission.**

The coordinate system for determining the momentum of a photoemitted electron by means of angular resolution. polar ( $\theta$ ) and azimuthal ( $\varphi$ ) angles are defined as shown.

Using the spherical coordinate system given in the Fig. 2.6, these magnitudes can be found as,

$$|\mathbf{K}_{\parallel}| = \frac{1}{\hbar} \sqrt{2mE_{kin}} \sin(\theta) = \begin{cases} K_x = \frac{1}{\hbar} \sqrt{2mE_{kin}} \sin(\theta) \cos(\varphi) & (2.26) \\ K_y = \frac{1}{\hbar} \sqrt{2mE_{kin}} \sin(\theta) \sin(\varphi) & (2.27) \end{cases}$$

and,

$$K_z = \frac{1}{\hbar} \sqrt{2mE_{kin}} \cos(\theta) \quad (2.28)$$

where the  $\theta$  and the  $\varphi$  are the polar and azimuthal emission angles, respectively.

Next step of the ARPES process is to deduce crystal momentum components,  $\mathbf{k}_x$ ,  $\mathbf{k}_y$  and  $\mathbf{k}_z$  by applying the conservation of momentum (equation 2.6). For typical ARPES

photoenergies, ( $h\nu < 100$  eV), the momentum of the incoming photon is negligible compared to typical momentum space Brillouin zone dimension,  $\frac{2\pi}{a}$ . So, in the reduced zone scheme (i.e., considering only the first Brillouin zone), the conservation of momentum reduces to:

$$\mathbf{k}_f - \mathbf{k}_i = \mathbf{k}_{h\nu} \approx 0 \quad (2.29)$$

This represents a vertical transition in the reduced-zone scheme as shown with a blue

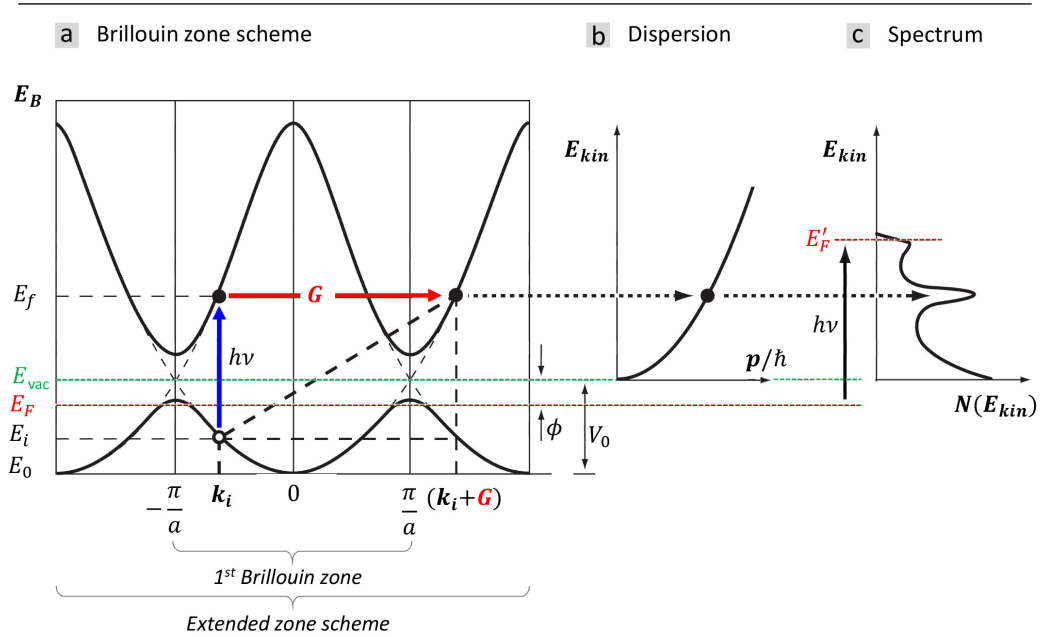


FIGURE 2.7: **Kinematics of photoemission spectroscopy.**

Kinematics of photoemission spectroscopy according to the three-step nearly free electron model. **(a)** Kinematics in the momentum space. The blue vertical arrow shows the direct optical transition in the reduced zone scheme while the red arrow shows a compatible transition in the extended zone scheme.  $k_i$  is the momentum of the initial state while  $G$  is the reciprocal lattice vector. **(b)** Nearly free electron final state dispersion in the vacuum. **(c)** corresponding photoelectron energy spectrum, with a background due to the scattered electrons.  $E_B$  is the electron binding energy with reference to the chemical potential,  $E_{kin}$  is detected electronic kinetic energy,  $N(E_{kin})$  is the detected density of states,  $E_i$  and  $E_f$  are initial and final state energies respectively,  $E_F$  (red horizontal dashed line) is the Fermi level where  $E_B = 0$ ,  $E_{vac}$  (green horizontal dashed line) is the vacuum level and  $E_0$  is the valence band bottom. The work function ( $\phi$ ) and the inner potential ( $V_0$ ) are also marked. Adapted from [69, 117].

vertical arrow on the Fig. 2.7(a). However, it has been repeatedly pointed out in the literature that, it is more useful to visualize photoemission in an extended-zone scheme[96, 98]. In an extended zone diagram, the crystal momentum would provide the additional momentum required by the photoexcitation in integer multiples of  $\mathbf{G}$ , while the photon provides the additional energy. Such a transition is indicated with a red arrow on the Fig. 2.7(a) and the conservation law of momentum thus can be generalized as,

$$\mathbf{k}_f^N - \mathbf{k}_i^N = \mathbf{G} \quad (2.30)$$

where  $\mathbf{G}$  is the reciprocal lattice vector.

In the following discussion, the relationships of photoelectron ( $\mathbf{K}$ ) and crystal ( $\mathbf{k}$ ) momenta will be built via three stages of approximation with increasing complexity.

### **Approximation Level 1: Infinite crystal with no periodic potential**

Consider the simplest case where no surface (i.e., no work function,  $\phi$ ) and no periodic lattice potential is present. This is an infinite free electron gas, thus no Brillouin zones in the momentum space. The dispersion relation is a simple parabola.

In this case, under the above assumption of  $k_{h\nu} \approx 0$ , no momentum conserving transition such that  $\mathbf{k}_f = \mathbf{k}_i$  is possible. Such direct transitions are forbidden since no final states are available. Even though the photon can provide energy, there is no agent (i.e.,  $\mathbf{G}$ ) to provide the necessary momentum.

### Approximation Level 2: Semi-infinite crystal with no periodic potential

For the next level of complexity, a surface for the free electron gas is introduced. In such a semi-infinite crystal, the surface would not perturb the translational symmetry in the x-y plane, chosen parallel to the surface.  $\mathbf{k}_{\parallel}$  ( $k_x, k_y$ ) will still be conserved up to a constant reciprocal lattice vector,  $\mathbf{G}_{\parallel}$  and therefore, will remain a good quantum number.

On the contrary,  $\mathbf{k}_{\perp}$  will be subjected to an abrupt change at the surface and so,  $k_z$  will no longer be a good quantum number. However, this momentum discontinuity at the surface can conserve the momentum in indirect transitions even in the absence of a crystal potential. This will give rise to a special case of photoemission known as *surface photoelectric effect*[96], and is beyond the scope of this introductory discussion.

### Approximation Level 3: Semi-infinite crystal with a periodic potential

In a more realistic case of a crystal with a surface and a periodic lattice potential, as illustrated in the Fig. 2.7(a), the three-step model discussed in the section 2.1.3.2 can be applied. Toward the objective of expressing detected momenta ( $\mathbf{K}$ ) in terms of crystal momenta ( $\mathbf{k}$ ), the bulk Bloch eigenstates inside the crystal are matched to free electron plane waves in the vacuum, as shown in the Fig. 2.4.

For momentum components parallel to the surface, the translational symmetry is still valid and it is trivial that,

$$k_{\parallel} = K_{\parallel} = \frac{1}{\hbar} \sqrt{2mE_{kin}} \sin(\theta) \quad (2.31)$$

with  $k_{\parallel} = |\mathbf{k}_{\parallel}|$ , where  $\mathbf{k}_{\parallel}$  is the crystal momentum component parallel to the surface. In the extended-zone scheme, this can be projected on to the first order Brillouin zone by subtracting the reciprocal lattice vector,  $\mathbf{G}_{\parallel}$ .

For the work presented in this dissertation as well as in most ARPES studies in the literature, the interpretation of the parallel momentum components is sufficient. However, for the sake of completeness, the perpendicular momentum component can be expressed as follows.

$$k_{\perp} = \frac{1}{\hbar} \sqrt{2m(E_{kin} \cos^2(\theta) + V_0)} \quad (2.32)$$

In terms of the equation 2.28, this becomes,

$$k_{\perp} = \sqrt{K_{\perp}^2 + \frac{2m}{\hbar^2} V_0} \quad (2.33)$$

The parameter ‘inner potential’,  $V_0$  above is defined using the work function,  $\phi$  and the bottom of the valence band,  $E_0$  with reference to the chemical potential,  $E_f$  (see Fig. 2.2) as follows[96].

$$V_0 = |E_0| + \phi \quad (2.34)$$

Determination of this inner potential is done in several methods under appropriate approximations for each case [69, 118–120].

### 2.1.4.1 ARPES of Low-Dimensional Systems

One particular case in which the  $k_{\perp}$  is practically needless is, in low-dimensional systems with an anisotropic electronic structure having insignificant dispersion along the z-axis; therefore, the electronic dispersion is almost  $E(\mathbf{k}_{\parallel})$ [96]. Transition metal oxides like copper oxide superconductors [118, 121] and transition metal dichalcogenides are widely studied examples under this category. Chapters 3 and 4 present ARPES studies on such quasi two dimensional systems.

In the case of low dimensional samples, the width of the photoemission peaks can be directly correlated to the lifetime of the photohole states[122]. These lifetimes, related to the imaginary part of the electron self-energy, can be used in probing quasiparticle correlation effects of the crystal. Such a study is presented in the chapter 4.

Finally, the energy and momentum relationships between detected photoelectrons and the states inside the crystal can be summarized as[123]:

$$E = -E_B = E_{kin} - h\nu \quad (2.35)$$

$$k_x = K_x = \frac{1}{\hbar} \sqrt{2mE_{kin}} \sin(\theta) \cos(\varphi) \quad (2.36)$$

$$k_y = K_y = \frac{1}{\hbar} \sqrt{2mE_{kin}} \sin(\theta) \sin(\varphi) \quad (2.37)$$

In a nutshell, ARPES exposes the sample to photon with energy  $h\nu$ , and then detects  $E_{kin}$  and  $\mathbf{K}$  of the photoelectrons ejected into the vacuum. Next, it determines the

binding energy  $E_B$  and the crystal electronic momentum  $\mathbf{k}$ , and finally constructs the electronic band dispersion:  $E(\mathbf{k})$ .

### 2.1.5 Spectral Function Formalism of ARPES Data

The photoemission process, mainly in the regime of correlated electron systems as discussed in the section (2.1.3.4) is conveniently explained with a spectral function formalism. In this scheme, the propagation of a single electron in a many-body system is described using a time-ordered one-electron Green's function,  $\mathcal{G}(t - t')$  [124–129]. Squared Green's function can be interpreted as the probability that an electron in a Bloch state with momentum  $\mathbf{k}$  at a  $t = 0$  will still remain in the same state after a time  $|t - t'|$  [96]. This Green's function can be Fourier transformed from the time domain to the energy-momentum domain as,

$$\mathcal{G}(\mathbf{k}, \omega) = \mathcal{G}^+(\mathbf{k}, \omega) + \mathcal{G}^-(\mathbf{k}, \omega) \quad (2.38)$$

where the advanced Green's function,  $\mathcal{G}^+(\mathbf{k}, \omega)$  and the retarded Green's function,  $\mathcal{G}^-(\mathbf{k}, \omega)$  respectively represent one-electron addition and removal. Define the electron annihilation operator  $c_{\mathbf{k}}^- = c_{\mathbf{k}}^\dagger$  such that,

$$\Psi^{N-1} = c_{\mathbf{k}\sigma} \Psi^N \quad (2.39)$$

and also the corresponding electron creation operator  $c_{\mathbf{k}}^+ = c_{\mathbf{k}\sigma}$ . These operators act upon the N-partial initial state  $\Psi_i^N$  to create or annihilate an electron with the energy

$\omega$ , momentum  $\mathbf{k}$ , and the spin  $\sigma$ . In the zero temperature limit, Greens functions can be explicitly expressed as, (by taking  $\hbar = 1$ )

$$G^\pm(\mathbf{k}, \omega) = \sum_m \frac{|\langle \Psi_m^{N\pm 1} | c_{\mathbf{k}}^\pm | \Psi_i^N \rangle|^2}{\omega - E_m^{N\pm 1} + E_i^N \pm i\eta} \quad (2.40)$$

where  $\eta$  is a positive infinitesimal. In the limit of  $\eta \rightarrow 0^+$ , using the integration identity,  $(x \pm i\eta)^{-1} = \mathcal{P}(1/x) \mp i\pi\delta(x)$  where  $\mathcal{P}$  is the principle value, the one-particle spectral function can be defined as,

$$A(\mathbf{k}, \omega) = -\frac{1}{\pi} \text{Im} \{G(\mathbf{k}, \omega)\} \quad (2.41)$$

or,

$$A^+(\mathbf{k}, \omega) + A^-(\mathbf{k}, \omega) = -\frac{1}{\pi} \text{Im} \{G^+(\mathbf{k}, \omega) + [G^-(\mathbf{k}, \omega)]^*\} \quad (2.42)$$

Here  $[G^-(\mathbf{k}, \omega)]^*$  accounts for the retarded Green's function while  $A^+(\mathbf{k}, \omega)$  and  $A^-(\mathbf{k}, \omega)$  define spectra resultant in one electron addition and removal, respectively. Electron addition can be probed with direct photoemission and the removal, in theory, can be probed with inverse photoemission. These spectral functions can now be explicitly stated as,

$$A^\pm(\mathbf{k}, \omega) = \sum_m |\langle \Psi_m^{N\pm 1} | c_{\mathbf{k}}^\pm | \Psi_i^N \rangle|^2 \delta(\omega - E_m^{N\pm 1} - E_i^N) \quad (2.43)$$

This is derived in the zero temperature limit, but the same procedure can be followed for finite temperatures as well, by starting with appropriate Green's functions [127]. By utilizing the sudden approximation discussed above in the section 2.1.3.3, the measured ARPES intensity can be expressed in terms of the spectral function as,

$$I(\mathbf{k}, \omega) = I_0(\mathbf{k}, \nu, \mathbf{A}) f(\omega) A(\mathbf{k}, \omega) \quad (2.44)$$

In a two-dimensional single band system,  $\mathbf{k} = \mathbf{k}_{\parallel}$  and energy  $\omega$  is the electron energy measured with respect to the chemical potential.  $\nu$  is the frequency of incoming photon while  $\mathbf{A}$  is the electromagnetic vector potential and,

$$I_0(\mathbf{k}, \nu, \mathbf{A}) \propto |M_{f,i}^{\mathbf{k}}|^2 \quad (2.45)$$

is the one-electron matrix element which was established in the section 2.1.3.4 via equations 2.19 and 2.20. It depends on the electron momentum, photon energy, and photon polarization.

The intensity modulation by Fermi function,

$$f(\omega) = \frac{1}{1 + e^{\frac{\omega}{k_B T}}} \quad (2.46)$$

relates to the fact that, the direct ARPES only can detect the occupied electronic states.

Since  $A(\mathbf{k}, \omega)$  is the probability of removing or adding an electron with momentum  $\mathbf{k}$  and energy  $\omega$  to a many-particle system, it should theoretically fulfill the following relationship,

$$\int_{-\infty}^{+\infty} A(\mathbf{k}, \omega) d\omega = 1 \quad (2.47)$$

for the practical case of photoemission experiments where only the electron removal spectrum ( $A^-(\mathbf{k}, \omega)$ ) is available, the relationship,

$$\int_{-\infty}^{+\infty} f(\omega) A(\mathbf{k}, \omega) d\omega = n(\mathbf{k}) \quad (2.48)$$

is more useful in practice, where  $n(\mathbf{k})$  is the momentum distribution.

### 2.1.5.1 Self Energy Formalism

Augmentations to the spectral function due to quasi-particle interactions can be taken into account using the *proper self-energy* function. This complex function can be expressed as,

$$\Sigma(\mathbf{k}, \omega) = \Sigma'(\mathbf{k}, \omega) + i\Sigma''(\mathbf{k}, \omega) \quad (2.49)$$

The real part,  $\Sigma'(\mathbf{k}, \omega)$  contains information about band renormalizations while the imaginary part,  $\Sigma''(\mathbf{k}, \omega)$  holds information about life times.

An electron of band energy  $\epsilon_k$  and crystal momentum  $\mathbf{k}$ , propagating in a many-particle system would have a Green's Function:

$$G(\mathbf{k}, \omega) = \frac{1}{\omega - \epsilon_k - \Sigma(\mathbf{k}, \omega)} \quad (2.50)$$

Then, by the relationship 2.41, the spectral function becomes,

$$A(\mathbf{k}, \omega) = -\frac{1}{\pi} \frac{\Sigma''(\mathbf{k}, \omega)}{[\omega - \epsilon_k - \Sigma'(\mathbf{k}, \omega)]^2 + [\Sigma''(\mathbf{k}, \omega)]^2} \quad (2.51)$$

The  $G(t, t')$  is a linear response function to an external perturbation and  $G(\mathbf{k}, \omega)$  is its Fourier transform as discussed above. This is bound to satisfy causality, which means in principle, real and imaginary parts of  $G(\mathbf{k}, \omega)$  are related via *Kramers–Kronig relations*. If the complete spectral function as in the equation 2.42 is available experimentally,  $Im\{G(\mathbf{k}, \omega)\}$  can be found from the equation 2.41, and then  $Re\{G(\mathbf{k}, \omega)\}$  can be calculated with Kramers–Kronig relations. Then the equation 2.49 can be used to find self energy,  $\Sigma(\mathbf{k}, \omega)$ . However, in reality, due to the lack of inverse photoemission data, complete spectral function  $A(\mathbf{k}, \omega)$  is not possible to measure, and this approach is not applicable. Rather, in practice, system-specific approximations are used in finding real and imaginary self energy components[47, 96, 130]. Such a study is presented in Chapter 4.

## 2.2 Representation of ARPES Data

ARPES data obtained for a fixed photoenergy,  $h\nu$  is shown in the Fig. 2.8(a). Independent variables are two orthogonal momentum components (e.g.  $k_x, k_y$ ) and energy ( $\bar{\omega}$ ). Momenta are usually expressed in units of inverse-angstroms ( $\text{\AA}^{-1}$ ) since they represent reciprocal space dimensions. In some cases, angle ( $\theta$ ) with units of degrees is also used as, in ARPES, momentum is resolved by means of the emission angle of the photoelectron (see the Fig. 2.6).

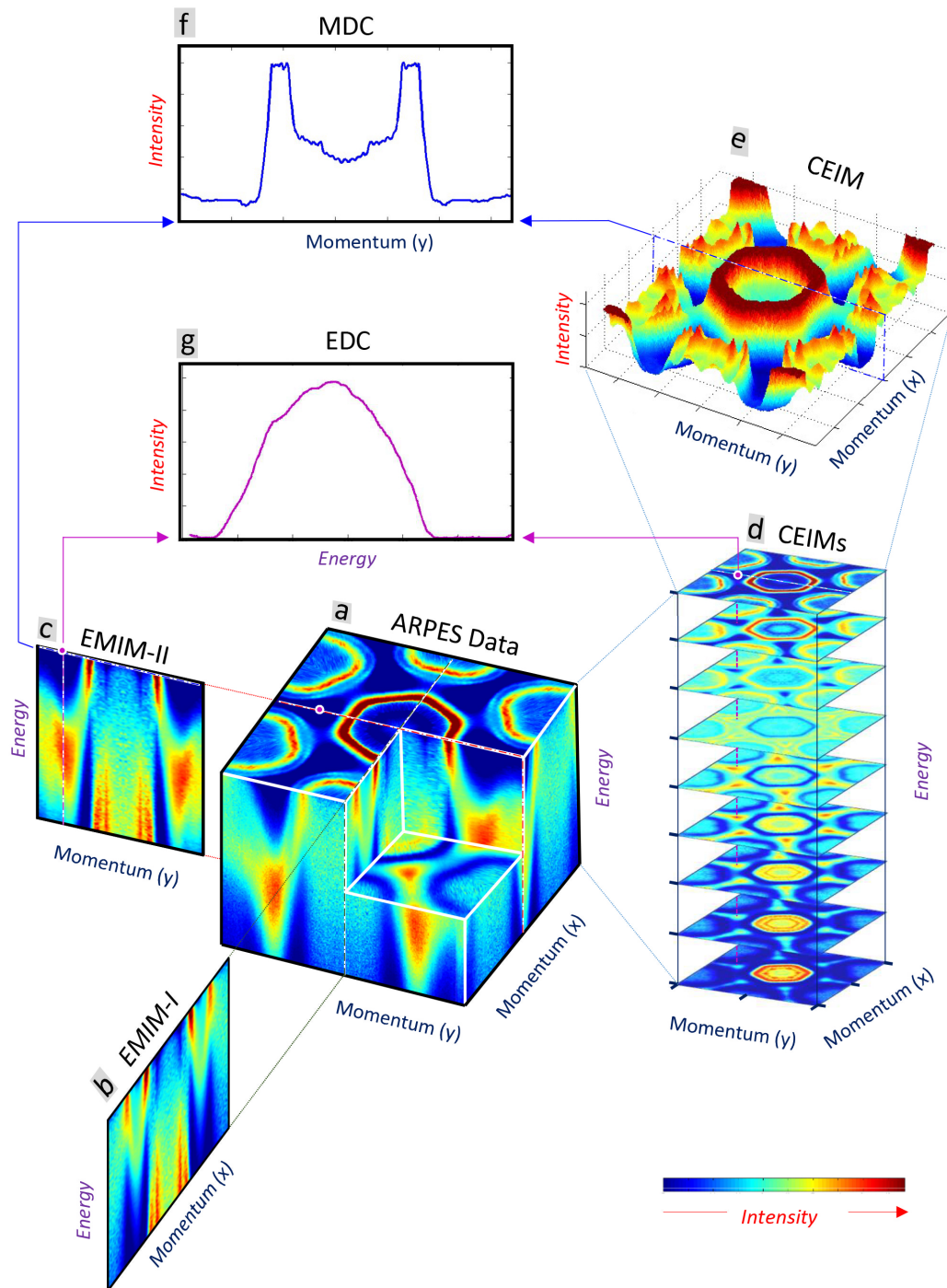


FIGURE 2.8: **Representation of ARPES data.**  
Please see the next page for the details.

**Representation of ARPES data.**

Continued from the previous page ...

(a) Primary ARPES data: Intensity  $I(k_x, k_y, \bar{\omega})$  as a function of independent variables, energy  $\bar{\omega}$  and in-plane momentum components  $k_x$  and  $k_y$ . (b, c) EMIM: *Energy Momentum Intensity Maps*, where the intensity is plotted as a function of energy and one momentum component while the other momentum component is fixed. (b) is  $I(k_x, \bar{\omega})$  for fixed  $k_y$ , or the image slice marked on (a) with a green dashed line, while (c) is  $I(k_y, \bar{\omega})$  for fixed  $k_x$ , or the image slice marked on (a) with red dashed lines. (d) CEIM: *Constant Energy Intensity Maps*, where the intensity is plotted as a function of in-plane momentum components for a fixed energy. These are energy iso-surfaces and a stack of such  $I(k_x, k_y)$  image slices are shown. Note the top most CEIM is the Fermi surface intensity map as it corresponds to  $\bar{\omega} = 0$ . (e) A three-dimensional CEIM representation (of the Fermi surface) where the height represents intensity. (f) MDC: A *Momentum Distribution Curve*, where the intensity is plotted as a function of one momentum component while the other momentum component and the energy are held constant. (f) Shows such an MDC,  $I(k_y)$  which can be visualized either as the intensity profile on the frame outlined by blue dashed lines on (e), or as the image line profile taken on blue dashed lines marked on (c) or (d). (g) EDC: A *Energy Distribution Curve*, where the intensity is plotted as a function of energy with both in-plane momentum components ( $k_x, k_y$ ) are fixed. Such an EDC,  $I(\bar{\omega})$  taken at the momentum location indicated by a pink dot on (a),(c) and (d) is shown in (f). This EDC can be visualized either as the image line profile taken on pink vertical dashed lines, marked on (c) or passes through the stack of CEIMs in (d).

---

Energy can be expressed as electron binding energies with the chemical potential as the zero energy level. Commonly used energy units are electron-Volts (eV).

The dependent variable is the signal intensity, which is the photoelectron count. It is proportional to the occupation probability of the filled states. Raw ARPES data is the intensity  $I = I(k_x, k_y, \omega)$  where  $\omega$  is the energy. In this dissertation, the notation  $\bar{\omega}$  will be used in representing energies expressed with respect to the chemical potential,  $\mu$ , where,

$$\bar{\omega} = \omega - \mu \quad (2.52)$$

The Raw ARPES data is in four-dimensional ‘chunks’ as in the Fig. 2.8(a). For visualization, analysis and communication purposes, four standard types of data subsets are

used in the literature. Two of them are three-dimensional where intensity is the dependent variable while two of  $k_x, k_y$ , or  $\bar{\omega}$  being independent variables, while the other is fixed. These are called *Intensity Maps* (IMs). Intensity is usually represented as color as in Fig. 2.8(b),(c) and (e), or occasionally as height as in the Fig. 2.8(e).

Two kinds of two-dimensional representations, known as *Curves* are also used. These curves can be visualized as subsets of intensity maps. The dependent variable is always the intensity which usually is the vertical axis, and the horizontal axis will represent the dependent variable which is either a momentum component,  $k$  or the energy,  $\bar{\omega}$ .

### 2.2.1 Energy Momentum Intensity Maps (EMIMs)

An EMIM is the intensity  $I(k_1, \bar{\omega})$  plotted as a function of one momentum component,  $k_1$  and energy,  $\bar{\omega}$ , by fixing the value of the other momentum component. In the Fig. 2.8(b), such an EMIM of  $I(k_x, \bar{\omega})$ , for a fixed  $k_y$  is shown. Relevant image slice is marked with green dashed lines on the Fig. 2.8(a). Another EMIM which is  $I(k_y, \bar{\omega})$ , for a fixed  $k_x$  is given in the Fig. 2.8(c) and the corresponding image slice location is marked with red dashed lines on the Fig. 2.8(a). Other types of EMIMs which are not strictly parallel to  $k_x$  or  $k_y$  can be constructed as well, by means of a momentum relationship that defines a line on the two-dimensional momentum plane (e.g.,  $k_x - 2k_y = 0$ ).

Since EMIMs have Energy ( $\bar{\omega}$ ) and momentum ( $k$ ) as axes, they are conveniently used in analyzing electronic band structure  $\bar{\omega}(k)$ . Chapters 4 and 5 depict such analysis.

### 2.2.2 Constant Energy Intensity Maps (CEIMs)

Energy iso-surfaces or CEIMs are maps of ARPES intensity  $I(k_x, k_y)$  as a function of in-plane momentum components  $k_x$  and  $k_y$  at a fixed energy  $\bar{\omega}$ . A series of such CEIMs are shown in the Fig. 2.8(d). The special CEIM at  $\bar{\omega} = 0$  is referred to as the ‘Fermi surface intensity map’. Such maps will be used in laying out blue prints for analysis in chapters 3, 4 and 5.

In quasi two-dimensional materials, CEIMs often provide a general insight into the momentum space landscape. Another representation of CEIM is given in the Fig. 2.8(e) where the height (as well as the color) represents intensity. Both Fig. 2.8(d) and (e) visualizes the characteristic double-walled barrel structure in the momentum space of  $2H$ – transition metal dichalcogenides.

### 2.2.3 Momentum Distribution Curves (MDCs)

An MDC is, intensity  $I(k_1)$  plotted as a function of a momentum component  $k_1$ , for fixed values of energy  $\bar{\omega}$  and the other momentum component. The Fig. 2.8(f) shows such an MDC  $I(k_y)$  for a particular  $k_x$  and  $\bar{\omega}$ . This MDC can be primarily visualized as the intensity on the plane defined with a blue dashed frame on the Fig. 2.8(e). Alternatively, it is the intensity profiles at image line cuts denoted by the blue dashed lines on the EMIM-II (Fig. 2.8(c)) or on the topmost Fermi surface CEIM of Fig. 2.8(d).

In general, MDCs taken near the chemical potential are expected to show sharp peaks corresponding to bands. In Chapter 4, such an MDC analysis will be used to trace intricate details of band dispersions.

### 2.2.4 Energy Distribution Curves (EDCs)

An EDC,  $I(\bar{\omega})$ , is a plot of ARPES intensity as a function of  $\bar{\omega}$  taken at a fixed point in the momentum space  $(k_x, k_y)$ . An example EDC is given in the Fig. 2.8(g) and corresponding locations can be visualized as purple vertical dashed lines on either EMIM-II (the Fig. 2.8(c)) or on the stack of CEIMS in the Fig. 2.8(d). This momentum location is marked as a purple dot on the Fig. 2.8(a) as well.

EDCs are primarily useful in determining energy gaps, as can be seen in Chapter 3. They can also be used in determining band structure, particularly when the features under analysis are away from the chemical potential. Such a case will be studied in Chapter 5.

### 2.2.5 Conditioning ARPES Data

Here ‘conditioning’ refers to the general procedure performed on raw ARPES data before any particulate analysis. This can be considered as the initial step of any ARPES data normalization. Subsequent steps of data normalization that are specific to each analysis will further be discussed in relevant contexts in the proceeding chapters.

As per equation 2.44, measured ARPES intensity signal is the convolution of the spectral function,  $A(\mathbf{k}, \omega)$  and the Fermi distribution function,  $f(\omega)$ . Also, on the other hand, the detector has finite energy and momentum resolutions and should be compensated for as well. To isolate the spectral function data from the raw ARPES intensity data, two main methods are utilized in the literature.

### 2.2.5.1 Division by the Fermi Function

In this method, the raw data gets divided by a Fermi distribution function characterized by an effective temperature,  $T_{eff}$ .

1. Determine the full-width-at-half-maxima (FWHM) associated with the detector energy resolution,  $W$ . This resolution broadening is of Gaussian type.
2. Calculate the effective temperature,  $T_{eff}$  which accounts for both Fermi distribution expected at the actual temperature  $T$  the data were acquired -and- for the above mentioned resolution broadening,  $W$ . A good approximation, as shown in the Fig. 2.9 is,

$$(K_B T_{eff})^2 = (K_B T)^2 + \left(\frac{W}{4}\right)^2 \quad (2.53)$$

3. Construct a Fermi distribution function with this effective temperature,

$$f(\omega) = \frac{1}{1 + e^{\frac{\omega}{k_B T_{eff}}}} \quad (2.54)$$

4. Divide the raw data with this effective Fermi function. Specifically, each energy distribution curve (EDC) can be divided by this or, an entire energy momentum intensity map (EMIM) can be divided by a two dimensional Fermi function value set.

For energies above the chemical potential, the Fermi function quickly approaches zero, and so the Fermi function division blows up. However, as discussed in the section 2.1.5, this should not become a significant problem in practice, since no photoemission data

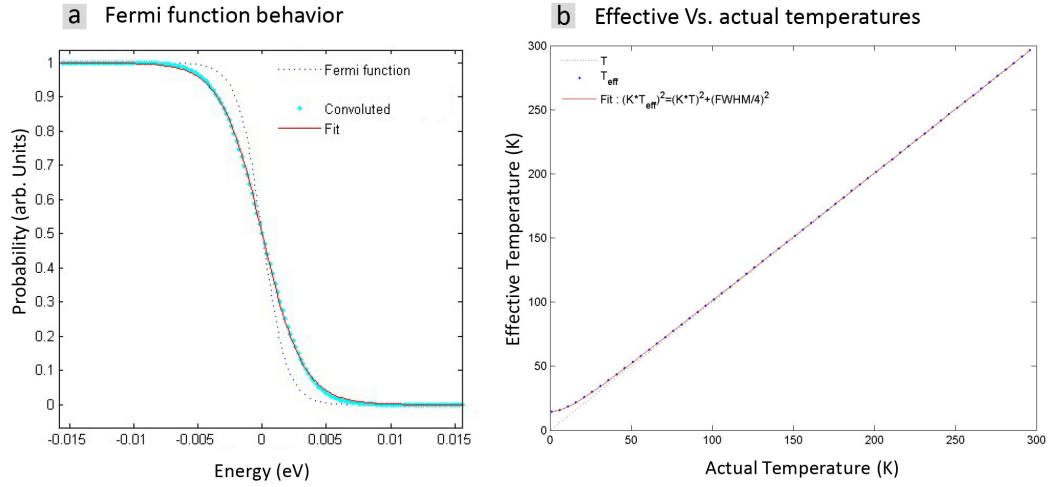


FIGURE 2.9: **Fermi function and effective temperature.**

The effective temperature due to the finite detector energy resolution is estimated as

$$T_{eff} = \sqrt{(T)^2 + \left(\frac{W}{4K_B}\right)^2}.$$

(a) Fermi functions at  $T = 11\text{K}$  (blue dotted line) and for an effective temperature  $T_{eff}$ , compensating for an energy resolution of 5 meV (large light blue dots). Red fit is used to extract  $K_B T_{eff}$ . (b) Effective temperature vs actual sample temperature. Note how the finite detector resolution results in an overestimation for lower temperatures.

can be acquired due to the lack of occupied electronic states in this region anyway. Fermi function division is a widely used method and was utilized in all the studies presented in this dissertation as well.

### 2.2.5.2 Lucy-Richardson Deconvolution

The Lucy-Richardson iterative deconvolution algorithm is popular in image analysis. In this method, data is deconvoluted by using a *deconvolution filter*, also known as a *kernel* which is a *point-spread function* (PSF) in this context. First, the raw ARPES data is divided by a Fermi function as explained above, but using the actual sample temperature  $T$ . Then the resultant data is deconvoluted with a Gaussian deconvolution filter with an FWHM determined by the detector resolution,  $W$ .

In practical ARPES data analysis, such as EDC analysis, a one-dimensional deconvolution filter that accounts only for the energy resolution might be sufficient. However, it is possible to construct an asymmetric two-dimensional deconvolution filter with both energy and momentum widths and deconvolute an entire EMIM at once. Usage of this method is limited so far in the literature [131], but for the presented work, both the Lucy-Richardson deconvolution and the Fermi function division resulted in similar results.

Alternatively, instead of trying to remove the effect of finite detector resolution, Fermi function divided data can be fitted with *Voigt* fits. A Voigt function is a convolution of a Lorentzian form with a Gaussian form. By fitting peaks with a Voigt model with a fixed Gaussian width which accounts for detector resolution, the effective Lorentzian width of the optical transition can be determined. This method is particularly useful in analyzing peak widths of momentum distribution curves (MDCs), as the Fermi function division method explained above is unable to compensate for detector momentum resolution. Chapter 4 outlines such an analysis.

## 2.3 Experimental Details

The ARPES measurements reported in chapter 3 and 4 were conducted using the 21.2 eV Helium-I line from a discharge lamp along with a Scienta<sup>®</sup> R3000 analyzer at the University of Virginia, Virginia, USA, and using a Scienta<sup>®</sup> R4000 analyzer at the plane grating monochromator (PGM) beamline (22 and 75 eV) of the Synchrotron Radiation Center (SRC), Wisconsin, USA. The angular resolution was  $\sim 0.01 \text{ \AA}^{-1}$  (0.3 degree), while the energy resolution was  $\sim 8\text{--}15 \text{ meV}$ . Samples used in these studies were synthesized using the standard Iodine vapor deposition method.

For the study in Chapter 5 which was conducted in the SRC's PGM beamline with 22 eV synchrotron light, the energy resolution was  $\sim 20$  eV, and the momentum resolution was  $0.0055 \text{ \AA}^{-1}$ . Samples for this study were prepared by melting mixtures of constituents inside evacuated fused silica tubes.

All the ARPES measurements were done in ultra-high vacuum environments (pressure less than  $5 \times 10^{-11}$  Torr), in both facilities. Temperatures were measured using silicon diode sensors located close to the sample holder. Temperature dependent data were collected in cyclic manners to verify that there were no effects due to sample aging. During each measurement, the chemical potential  $\mu$  of the system was determined by fitting a Fermi function to an ARPES spectrum obtained for a polycrystalline gold reference sample in electrical contact with the sample under study[69].

---

## Chapter 3

# Charge Density Waves in Transition Metal Dichalcogenides

### 3.1 Background

The charge density wave (CDW) phenomenon is believed to be related to some of the interesting observations in the field of condensed matter physics such as pseudogap in cuprate high-temperature superconductors [49–51], enormous mass renormalization of heavy fermions [52, 53] and colossal magnetoresistance in manganite compounds [54, 55]. However, the study of the charge density wave order in these materials becomes challenging due to the simultaneous occurrence of various competing interactions in the systems[47]. Because of this, the study of prototype charge density wave materials such as transition metal dichalcogenides (TMDs) is useful as they possess comparatively simpler crystal and electronic structures. TMDs can be considered as an ideal class of material to study CDW formation in low dimensions due to this simplicity. Additionally, the CDW orders in the TMDs can be modulated via various external perturbations leading to fascinating phase diagrams.

We conducted a series of Angle Resolved Photo-Emission Spectroscopy (ARPES) studies to probe both generalizable and compound-specific features of the incommensurate CDW order in layered TMDs in momentum, energy, and temperature domains. This study focuses on  $2H - \text{TaS}_2$ ,  $2H - \text{TaSe}_2$  and  $2H - \text{NbSe}_2$  which are canonical quasi-two-dimensional CDW materials[6, 7, 10]. All three compounds exhibit a transition from a metallic to an incommensurate CDW state, and in the case of  $2H - \text{TaSe}_2$ , a commensurate CDW phase also exists upon further reduction in temperature. At very low temperatures, the co-existence of charge density waves with superconductivity is observed. For  $2H - \text{TaS}_2$ , this phase coexistence occurs below 0.8 K [19–21].

### 3.2 The Charge Density Wave Vector, $\mathbf{q}_{\text{CDW}}$

For an incommensurate charge density wave state, the periodicity of the charge density modulation is different from the lattice periodicity. In other words, the wavelength of the charge density wave is not an integer multiple of the lattice periodicity. The incommensurate CDW phase of these layered transition metal dichalcogenides show a hexagonal symmetry[59, 60], characterized by a charge density wave vector  $\mathbf{q}_{\text{CDW}}$  having the magnitude of[45]:

$$|\mathbf{q}_{\text{CDW}}| = (1 - \delta) \frac{a^*}{3} \quad (3.1)$$

The parameter  $\delta \sim 0.02$ , determines the degree of incommensuration while  $\mathbf{a}^*$  is the reciprocal lattice constant. If the hexagonal real space Bravais lattice has a lattice constant of  $\mathbf{a}$ , this reciprocal lattice constant,  $\mathbf{a}^*$  of its self-dual hexagonal reciprocal lattice can be given as:

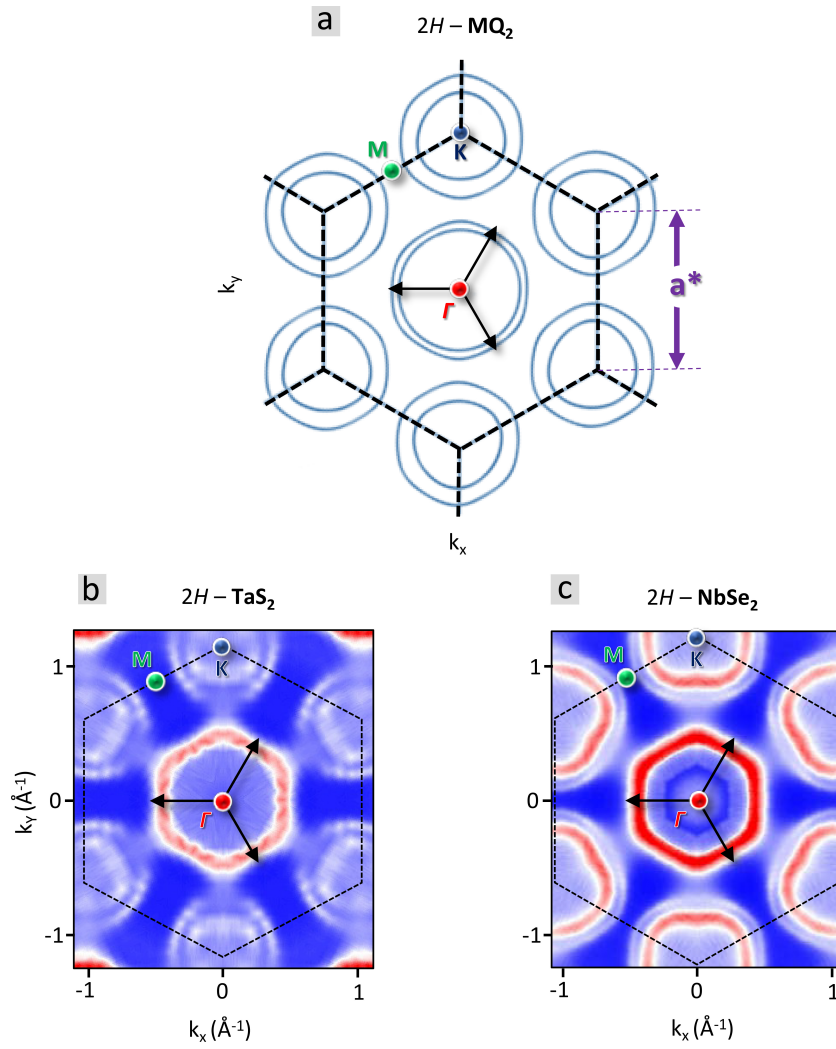


FIGURE 3.1: Charge density wave vectors of 2H-transition metal dichalcogenides.

(a) Calculated Fermi surface for a general 2H-TMD [132]. (b) and (c) Experimental Fermi surface of 2H-TaS<sub>2</sub> and 2H-NbSe<sub>2</sub>, respectively [92, 133]. Black solid arrows represent individual charge density wave vectors in each diagram.

$$a^* = 4\pi/\sqrt{3}a \quad (3.2)$$

The Fig. 3.1(a) depicts these charge density wave vectors with reference to a calculated Fermi surface diagram [132] whereas Fig. 3.1(b) and (c) overlay such CDW wave vectors on experimentally observed normal state ( $T > T_{CDW}$ ) Fermi surface diagrams for 2H-

TaS<sub>2</sub> and for 2H – NbSe<sub>2</sub>, respectively. Note the relative size of black arrows that represent charge density wave vectors, compared to the underlying reciprocal space lattice.

### 3.3 Low Energy Electronic Structure of 2H - TMDs

#### 3.3.1 Fermi Surface Topology

Band structure calculations for 2H– transition metal dichalcogenide material under investigation predict two closely spaced pairs of quasi-two-dimensional Fermi surface (FS) barrels centered around  $\Gamma$  and K symmetry points[132]. A schematic is shown in the Fig. 3.1(a). These barrels are associated with bonding and anti-bonding bands derived from the transition metal  $d$  orbitals[38, 40, 92, 134, 135]. Further, these barrels are double-walled because there are two ‘ $MQ_2$ ’ formula units per unit cell as shown in Fig. 1.2.

Experimental Fermi surface intensity maps of 2H – TaS<sub>2</sub> and 2H – NbSe<sub>2</sub> are presented in Fig. 3.2(a) and (b), respectively. These are intensity plots of electron count  $I(k_x, k_y)$  as a function of the in-plane momentum components  $k_x$  and  $k_y$ , taken at the energy isosurface of  $\bar{\omega} = 0$ . The parameter  $\bar{\omega}$  is the electronic energy with respect to the chemical potential,  $\mu$ . These Fermi surface maps were constructed for the normal state with the data collected at temperatures  $T > T_{CDW}$ , for both materials. Fermi surface intensity map for 2H – TaS<sub>2</sub> in Fig. 3.2(a) is based on ARPES data collected with 75 eV photon energy ( $h\nu$ ) at a temperature,  $T \sim 90\text{K}$ , while data for 2H – NbSe<sub>2</sub> in Fig. 3.2(b) corresponds to  $h\nu = 22\text{ eV}$  at  $T \sim 50\text{K}$ .

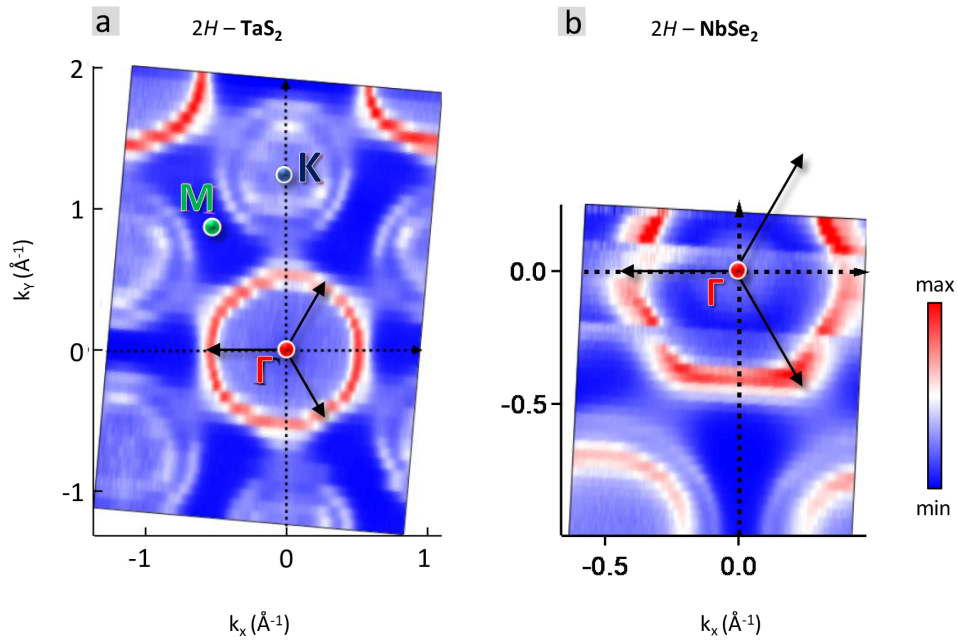


FIGURE 3.2: **Fermi surfaces and charge density wave vectors.** Fermi surface of (a)  $2H - \text{TaS}_2$  and (b)  $2H - \text{NbSe}_2$ . Black arrows in (a) and (b) represent individual charge density wave vectors [92, 133].

Experimental data shown in the Fig. 3.2 agree well with band structure calculations[132].

The common observations for both  $2H - \text{TaS}_2$  and  $2H - \text{NbSe}_2$  are:

- There are double-walled FS barrels centered around  $\Gamma$  and K points.
- Saddle bands are visible as regions of high intensity along  $\Gamma$ –K lines.

However, there are certain compound specific features as well. For example:

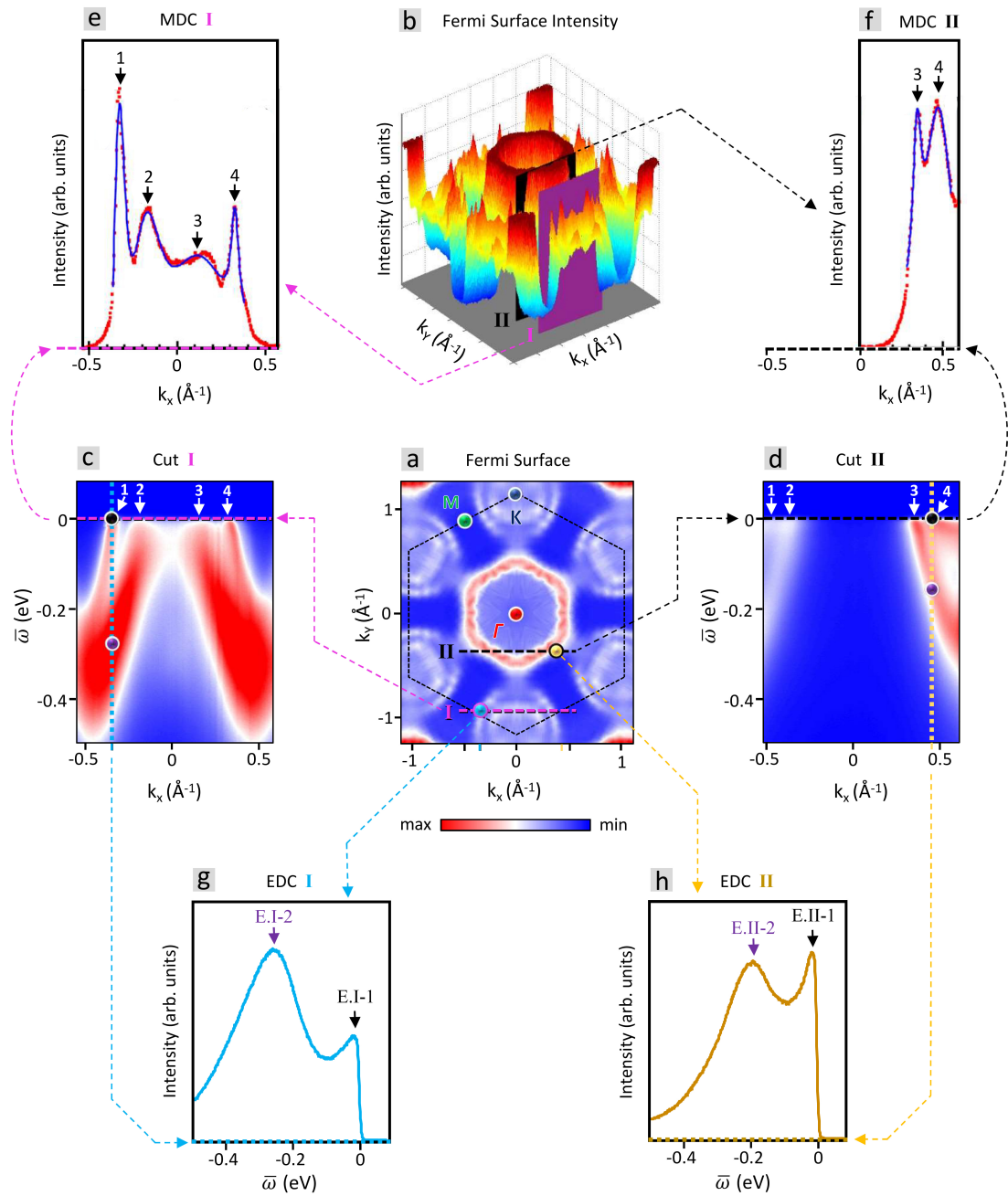
- The *pancake* like intensity profile around  $\Gamma$  point observed for  $2H - \text{NbSe}_2$  as in the Fig. 3.2 (b) seems to be nonexistent for  $2H - \text{TaS}_2$  in the Fig. 3.2 (a). This difference might be more elaborate when comparing Fig. 3.1 (b) against (c), which represents the same data as in Fig. 3.2 (a) and (b), in a symmetrized/normalized manner.

- While the size of the  $\Gamma$  centric barrels stay almost the same for both systems, K centric barrels of  $2H - \text{NbSe}_2$  are larger in size compared to those of  $2H - \text{TaS}_2$ . This dichotomy in the size of the K centric Fermi surface barrels might have a role in determining the charge density wave transition temperature,  $T_{CDW}$ .

### 3.3.2 Fermi Surface Barrels

Consider some ARPES energy-momentum-intensity maps (EMIMs). An EMIM is the electron intensity  $I(k_x, \bar{\omega})$  plotted as a function of a momentum component (say,  $k_x$ ) and energy  $\bar{\omega}$ , taken by fixing the value of the other (say,  $k_y$ ) momentum component. The Fig. 3.3(a) is used as a blueprint to mark momentum locations in the following discussion.

Two EMIMs are shown in Fig. 3.3(c) and (d). The EMIM in the Fig. 3.3(c) is taken along the momentum cut-I, indicated by a pink dashed line on the Fig. 3.3(a). Similarly, the EMIM corresponding to the momentum cut-II, indicated by a black dashed line, is given in the Fig. 3.3(d). These EMIMs clearly display the bi-layer structure around K as well as  $\Gamma$  points.

FIGURE 3.3: Fermi surface of  $2H\text{-TaS}_2$ .

Please see the next page for the details.

**Fermi surface of  $2H$ -TaS<sub>2</sub>.**

Continued from the previous page ...

(a) The Fermi surface of  $2H$ -TaS<sub>2</sub>, pink and black dashed lines denote momentum cuts I and II, respectively. Two momentum points are also marked as yellow and light blue dots. (b) A three-dimensional representation of the Fermi surface, where intensity (height and color) are proportional to the electron occupation. Two planes marked in pink and black indicate momentum cuts I and II as identified on (a). (c) The energy-momentum intensity map (EMIM) along the momentum cut-I, with four Fermi crossings. (d) The EMIM taken along the momentum cuts-II. (e) The momentum distribution curve (MDC) along cut-I, together with Voigt fits indicated in blue. There is one-to-one correspondence between the peaks of the MDC and the Fermi crossings of the bands in (c). (f) The MDC along the momentum cuts-II. Here we only have focused on two rightmost Fermi crossings. (g) The energy distribution curve-I (EDC), at the momentum point marked as a light blue dot on (a) (or the intensity profile along the light blue dotted line on (c)). Peaks identified as E.I-1 and E.I-2 correspond to black and purple points marked on (c), respectively. (h) The EDC-II at the momentum point marked as a yellow dot on (a) (or along the yellow dotted line on (d)). Peaks identified as E.II-1 and E.II-2 correspond to black and purple points on (d).

---

We also observe this bi-layer splitting of energy bands from momentum distribution curves (MDCs), which are line plots of  $I(k_x)$  for a specific value of momentum,  $k_y$  and energy,  $\bar{\omega}$ . Fig. 3.3(e) and (f) are taken at the Fermi level (i.e.: at the chemical potential where  $\bar{\omega} = 0$ ) and they follow double-splittings of the energy bands expected due to the double-barreled nature. The momentum distribution curve in Fig. 3.3(e) clearly displays four peaks associated with four Fermi crossings (numbered 1, 2, 3, 4) and on the MDC in the Fig. 3.3(f), only two right peaks (numbered 3 and 4) are shown due to the weak intensity of left side peaks.

Alternatively, these momentum distribution curves in Fig. 3.3(e) and (f) can be visualized as intensities on the pink (I) and black (II) planes marked on the 3D diagram in Fig. 3.3(b). On both MDCs, experimental data points are represented by red markers while blue lines are the *Voigt* model fits to those data.

Further, we can use energy distribution curves (EDCs) to examine the double-walled structure of the energy bands. An EDC is a plot of ARPES intensity  $I(\bar{\omega})$  or the electron count as a function of energy  $\bar{\omega}$ , taken at a fixed of momentum point  $(k_x, k_y)$ . Fig. 3.3(g) and (h) show EDCs at the momentum locations marked by light-blue and yellow dotted lines on Fig. 3.3(c) and (d), respectively. These momentum locations are marked on the Fermi surface map on Fig. 3.3(a) as light-blue and yellow dots accordingly, as well. Two peak structures of these EDCs are signatures of the bi-layer split bands in each case.

### 3.3.3 Possibility of Fermi Surface Nesting

#### 3.3.3.1 Fermi Surface Nesting as a CDW Mechanism

The most common explanation for the formation of charge density is the Peierls distortion in one-dimensional systems [136, 137]. Consider the Peierls distortion, occurring at  $T = T_{CDW}$  in a hypothetical one-dimensional system as in the Fig. 1.3(a). The energy stored in the electronic bands decreases as the opening up of the gap leads to the removal of the density of states around the chemical potential  $\mu$  (see Fig. 1.3(b)). At the same time, the elastic energy of the system increases due to the underlying periodic lattice distortion (PLD). For the stability and persistence of such a charge density wave order, the reduction in the electronic kinetic energy should always exceed the increase in elastic potential energy of the lattice and thus, the total energy of the system is lowered in overall. In such a case, the system can undergo a transition from a high-temperature metallic phase to a distorted phase.

In case of CDW order driven by Fermi surface nesting, one would expect the following[138]:

- Regions that are sufficiently parallel to each other should be present on the Fermi surface.
- The charge density wave vector,  $\mathbf{q}_{\text{CDW}}$  should be able to join two such parallel regions of the Fermi surface, or in other words, the magnitude (length) of the CDW wave-vector,  $|\mathbf{q}_{\text{CDW}}|$  should match the momentum separation between those parallel regions.

### 3.3.3.2 Nesting Conditions in TMDs

In both  $2H - \text{TaS}_2$  and  $2H - \text{NbSe}_2$ , there exist a number of above mentioned parallel regions with higher electronic occupation on their Fermi surfaces. This is evident from the orientation of red or white colored regions in Fig. 3.1(b) and (c). One possible set of hypothetical nesting vectors are shown as green arrows on Fig. 3.4(a), as an example. Hence, at least in concept, such a nesting phenomenon seems viable in these transition metal dichalcogenides.

However, in contrary, experimental data does not support this idea for both cases of  $2H - \text{TaS}_2$  and  $2H - \text{NbSe}_2$ . The calculated charge density wave vector,  $\mathbf{q}_{\text{CDW}}$  has a magnitude given by the equation 3.1, and are marked with black arrows on a representative Fermi surface of  $2H - \text{TaS}_2$  on Fig. 3.4(b). It is clear that the separation of parallel Fermi surface regions does not agree with this magnitude of the observed CDW wave vectors[11, 45, 92, 134], as the separation between parallel regions on the Fermi surfaces (green arrows) are clearly too large to be self-nested by  $\mathbf{q}_{\text{CDW}}$  (black arrows). From the Fig. 3.4(c), it can be inferred that an identical argument applies for the  $2H - \text{NbSe}_2$  as well.

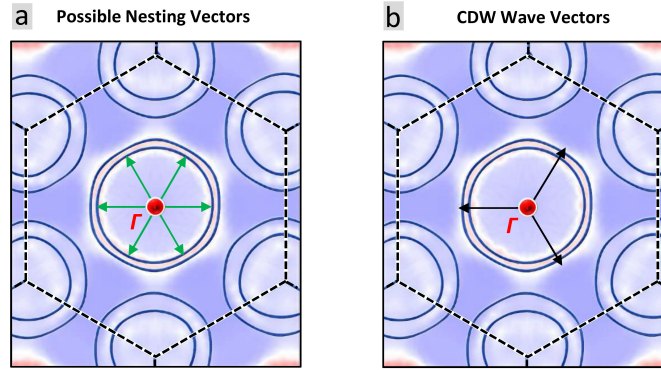


FIGURE 3.4: **Nesting vectors Vs. charge density wave vectors.**

(a) A possible set of hypothetical nesting vectors indicated in green arrows and (b) Observed charge density wave vectors shown in black arrows. Both are marked on identical representative Fermi surface maps of  $2H - \text{TaS}_2$ .

For  $2H - \text{NbSe}_2$ , it has been experimentally shown that the simple Fermi surface nesting is not sufficient to explain its charge density wave instability [133, 139]. But on the other hand, reports do not agree with the applicability of Fermi surface nesting for the case of  $2H - \text{TaSe}_2$  [140, 141]. Even though some nesting conditions appeared to be fulfilled in TMDs (like the existence of parallel regions), the above mentioned simple model of Fermi surface nesting cannot be considered as the mechanism behind charge density wave vector transition metal dichalcogenides.

### 3.3.3.3 Electronic Susceptibility Studies

From another perspective, if such a nesting within parallel sections of the Fermi surface occurs, the phenomenon should manifest itself as significant peaks in both the real and imaginary components of the non-interacting electronic susceptibility (i.e.: Lindhard susceptibility),  $\chi_0(\mathbf{q}, \bar{\omega})$  [138]. These signature peaks are expected when [46],

- The momentum-transfer,  $\mathbf{q} = \mathbf{q}_{\text{cdw}}$  and

- Energy,  $\bar{\omega} = 0$ ,

where  $\bar{\omega} = \omega - \mu$  (i.e.: energy with respect to the chemical potential).

However, theoretical calculations of the Lindhard susceptibility for  $2H - \text{NbSe}_2$  has found that the Fermi surface nesting itself is not a sufficient mechanism in explaining its charge density wave instability, due to the absence of expected susceptibility signatures [142, 143].

### 3.3.3.4 Motivation for a Strong Coupling Approximation

Other attempted explanations in the weak coupling regime have assumed alternate nesting mechanisms such as nesting within the saddle bands near the chemical potential due to Van Hove singularities[144], or a combination of nesting within Fermi surface, explained above, and nesting between such Van Hove singularities [145]. These alternative nesting models still lack the appropriate correlations with experimentally observed energies[92, 133, 145–149]. The consistent lack of experimental support for these candidate nesting models suggest that the weak coupling approach might not be sufficient in explaining the general mechanism of charge density wave formation in transition metal dichalcogenides [45].

On the other hand, An interesting observation has been reported. Namely, the *pseudogap* phenomena which means the persistence of non-zero charge density wave energy gap ( $\Delta_{CDW}$ ) even for temperatures much higher than the charge density wave transition temperature ( $T_{CDW}$ ) [92, 133, 146](see the section 3.4.4). Motivated by this observation, a handful of explanations have been formulated in the strong coupling limit[132, 150–153]. Several experimental studies have shown support for this approach

as well [45, 47, 92, 139, 154, 155], especially for the models in favor of the strong electron-phonon coupling and its momentum anisotropic nature. (see Chapter 4). In this study, high-resolution ARPES data, with energy, momentum, and temperature specificity were analyzed with the objective of developing a concise microscopic explanation of the charge density wave order in layered transition metal dichalcogenides in the strong coupling limit [45, 47, 92].

### 3.4 Charge Density Wave Energy Gap, $\Delta_{CDW}$

#### 3.4.1 Analysis Procedure for the CDW Energy Gap

From the section 1.1.2, it follows that the amplitude of the charge density wave order parameter,  $|\Psi|$  is directly proportional to the charge density wave energy gap,  $\Delta_{CDW}$ . This energy gap can be measured using ARPES[118, 156, 157] (see equations 3.3 and 3.4 as well). To probe this gap:

1. Energy distribution curves (EDCs: graphs of Intensity as a function of energy  $I(\omega)$  for a fixed momentum value) were constructed from the raw data.
2. These EDCs were normalized to account for the finite energy resolution of the detector, as well as for the effect of the Fermi-Dirac distribution function.
3. Resultant graphs are called Fermi function divided EDCs or normalized EDCs in general. Two different methods for this normalization were attempted (see the section 2.2.5). The first method was to divide EDCs by resolution broadened Fermi function [118, 158] while the second method being the Lucy-Richardson iterative

deconvolution [131, 159, 160]. Since both methods lead to similar conclusions, the first method was used thereafter.

4. These Fermi function divided EDCs were then analyzed for the momentum and temperature dependence of the CDW energy gap,  $\Delta_{CDW}$ .

### 3.4.2 Momentum Dependence of the CDW Energy Gap

#### 3.4.2.1 Bogoliubov Dispersion Signatures of the CDW Phase

Observe some energy distribution curves about the  $K^-$  symmetry point, taken in the vicinity of the Fermi momentum ( $k_F$ ) for  $2H - TaS_2$  and compare them to a similar analysis [146] done on  $2H - NbSe_2$ . For  $2H - TaS_2$ , momentum locations where the EDCs were taken, are marked on the schematic diagram in the Fig. 3.5(a) and also on the experimental Fermi surface map on the Fig. 3.5(b) using solid circles. For  $2H - NbSe_2$ , such EDC momentum locations are marked with 'X' marks, on the schematic Fig. 3.5(a) and on the Fermi surface map in the Fig. 3.5(c) as well. In all these EDCs, the color red indicates the Fermi momentum,  $k_F$ . The color purple represents EDCs taken at the locations with slightly lower momentum values than  $k_F$ , which are the points closer to the center and 'inside' of the barrel. Similarly, the color blue denotes EDCs corresponding to momentum values slightly higher than  $k_F$  (i.e., away from the center, and 'outside' of the barrel). Note that, all the reported EDCs are taken at the immediate vicinity of the Fermi momentum and the deviations above and below from the  $k_F$  were small. Also note that in the case of  $2H - TaS_2$  the outer  $K^-$  centric Fermi surface barrel is considered, whereas for the case of  $2H - NbSe_2$ , the inner  $K^-$  centric Fermi surface barrel has been used.

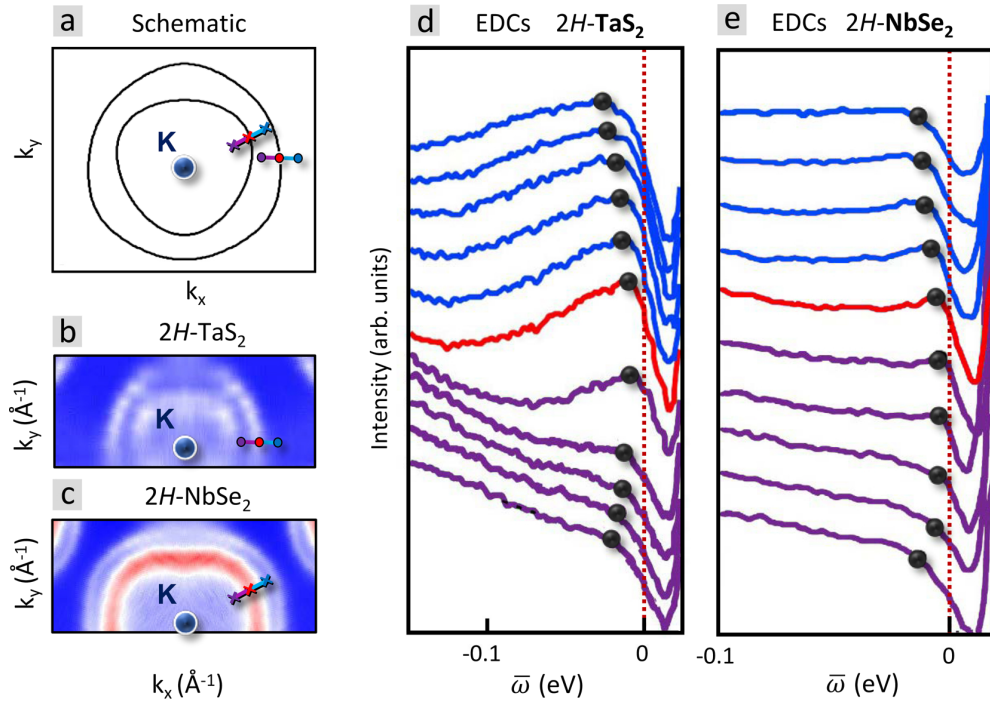


FIGURE 3.5: **Back bending of the bands due to Bogoliubov dispersion.**

(a) The schematic Fermi surface diagram of  $2H - MQ_2$ . Momentum locations in the neighborhood of the K point are marked where energy distribution curves (EDCs) in (d) and (e) are taken. (b) The Fermi surface map for  $2H - TaS_2$ , solid circles indicate momentum locations in the vicinity of the outer Fermi surface barrel where EDCs in (d) are taken. (c) The Fermi surface map for  $2H - NbSe_2$ , X marks indicate momentum locations in the vicinity of the inner barrel where EDCs in (e) are taken. (d) EDCs for  $2H - TaS_2$  at momentum locations denoted on (a) and (b) as solid circles near outer barrel, taken at  $T = 30$  K. (e) EDCs for  $2H - NbSe_2$  at momentum locations denoted on (a) and (c) as X marks near inner barrel, taken at  $T = 26$  K [146]. In both (d) and (e), the chemical potential ( $\bar{\omega} = 0$ ) is indicated as a red dotted line. The red EDC is taken on the barrel (i.e. at the Fermi momentum,  $k_F$ ) while purple and blue EDCs are taken just inside and outside the barrel for slightly lower and higher momenta, respectively. Black dots indicate peak positions of each EDC, which clearly exhibit Bogoliubov like back bending signature.

Relevant EDCs for  $2H - TaS_2$  and  $2H - NbSe_2$  are given in Fig. 3.5(d) and (e), respectively. Peak positions of these EDCs, which correspond to energy values of highest electron populations, are marked with black dots. Fermi energy ( $\bar{\omega} = 0$ ) is marked by red dotted lines. Compare the change in peak position relative to the Fermi energy for different EDCs taken below, on, and above the Fermi momentum. These peaks clearly follow the *Bogoliubov* like back-bending of the electronic dispersion as elaborated in the

section 1.1.2. Similar behavior has been observed in both transition metal dichalcogenides compounds,  $2H - \text{TaS}_2$  and  $2H - \text{NbSe}_2$ .

Note that the unoccupied upper branch of this dispersion (hole band) could not be observed since the ARPES technique is only sensitive to the occupied electronic states[45].

### 3.4.2.2 Momentum Anisotropy of the CDW Energy Gap

Series of energy distribution curves were taken in the K-neighborhood, as marked on the Fig. 3.6(a) and (b). These EDCs, taken along the circumference of both outer and inner K-centric Fermi surface barrels are plotted with marker and EDC color coordination in Fig. 3.6(d) and (e) for each barrel, respectively. Also, another series of EDCs were taken along the cut indicated by a black dotted arrow that spans approximately radially across both barrels, as shown on Fig. 3.6(b). These EDCs were taken at points with equal momentum separation. Corresponding EDCs are shown in the Fig. 3.6(f) in black, while two blue EDCs represent ones taken on the inner and outer Fermi surface barrels.

Observing the locations of the peaks relative to the chemical potential ( $\bar{\omega} = 0$ ) for the EDCs on Fig. 3.6(d), (e) and (f), it is evident that, the energy ( $\bar{\omega}$ ) position of the quasi-particle peak in each EDC, at each momentum location, on both inner and outer K-centric Fermi surface barrels, consistently lie below the chemical potential. This means that the both K-centric Fermi surface barrels are always gapped.

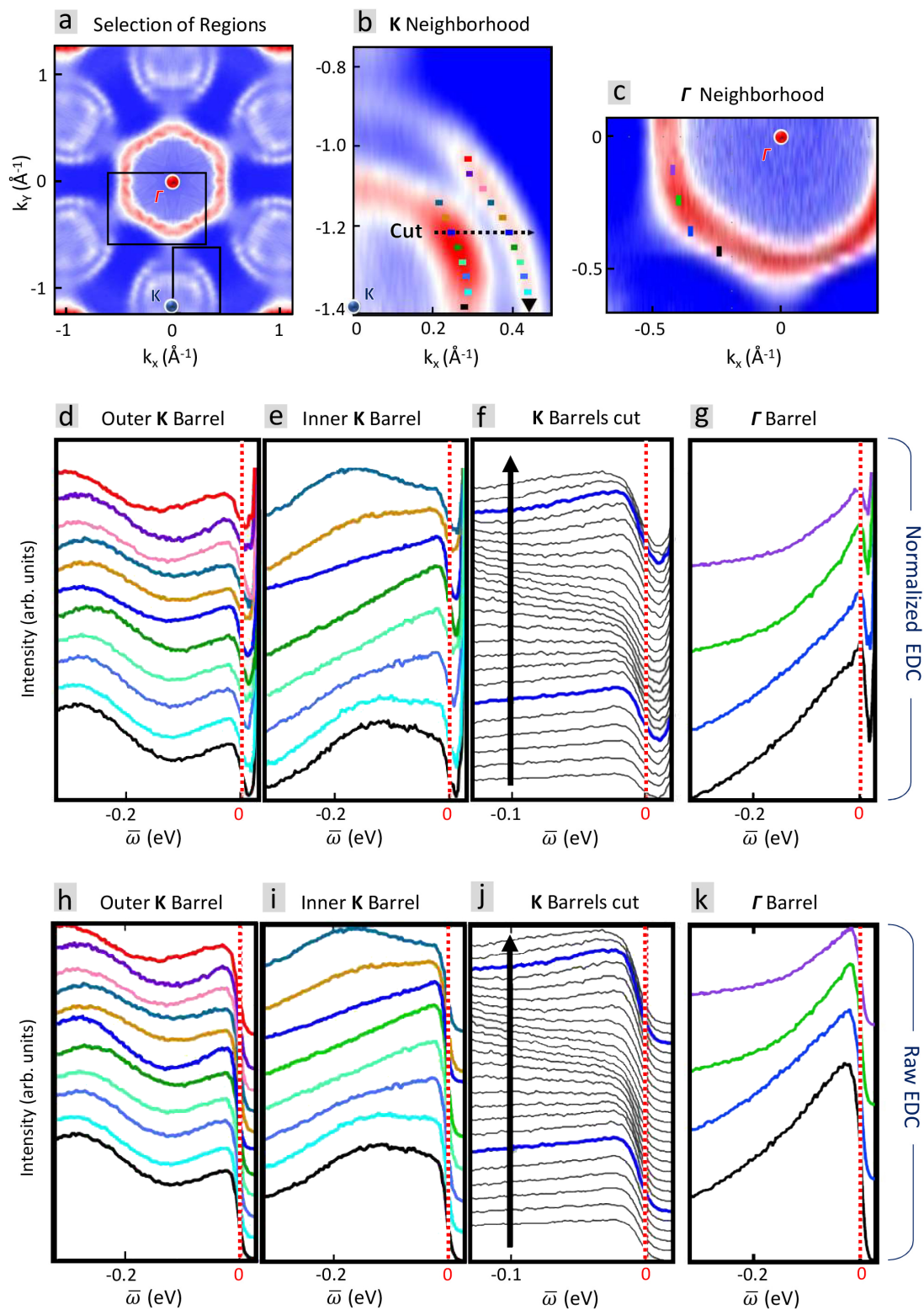


FIGURE 3.6: Energy distribution curves (EDCs) around K and  $\Gamma$  symmetry points in the charge density wave state of  $2H\text{-TaS}_2$ . Please see the next page for the details.

**Energy distribution curves (EDC) around K and  $\Gamma$  symmetry points in the charge density wave state of  $2H$ -TaS<sub>2</sub> ( $T = 45K < T_{CDW}$ , ARPES photon energy,  $h\nu = 22$  eV).**

Continued from the previous page ...

(a) Regions of interest in the neighborhoods of  $\Gamma$  and K points, marked on a normal state ( $> T_{CDW}$ ) Fermi surface map. (b) Color coded momentum locations around K point, where EDCs shown in (d),(e) and (f) are taken. (c) Color coded momentum locations around  $\Gamma$  point, where EDCs shown in (g) are taken. (d) EDCs taken on the outer K centric Fermi surface barrel, corresponding to momentum points marked on (b) with same color. (e) EDCs taken on the inner K barrel, corresponding to points marked on (b). (f) EDCs taken at a series of momentum points along the cut marked as a black dotted line on (b). (g) EDCs taken on the outer  $\Gamma$  centric Fermi surface barrel, corresponding to momentum points marked on (c). (h, i, j, k) Unnormalized EDCs corresponding to (d,e,f,g) respectively. Chemical potential ( $\bar{\omega} = 0$ ) is denoted by a red dotted line. EDCs in (d), (e) and (f), taken in the vicinity of K point always peak below  $\bar{\omega} = 0$  while EDCs in (g), in the vicinity of  $\Gamma$  point peak at  $\bar{\omega} = 0$ . All the EDCs have their minima falling above  $\bar{\omega} = 0$ .

---

A similar analysis was done about the  $\Gamma$  point on the respective Fermi surface region marked on Fig. 3.6(a) and (c). Corresponding color coded EDCs are presented in the Fig. 3.6(g). In contrary to the observations for K-centric Fermi surface barrels, all these EDC peaks align with the red dotted line denoting  $\bar{\omega} = 0$  (the chemical potential). This means  $\Gamma$ -centered Fermi Surface barrels are always gapless (i.e.,  $\Delta_{CDW} = 0$ ).

### 3.4.2.3 Momentum Specificity of the CDW Energy Gap

The charge density wave energy gap can be quantified by the energy separation between the peak of an energy distribution curve -and- the energy location of its minimum. Usually,  $\Delta_{CDW}$  is measured using EDCs taken at Fermi momentum, which means on the Fermi surface barrels, for this case. This follows from the equation 1.3 and can be visualized from the Fig. 1.3(b) as well. In the case of incommensurate CDW order as in  $2H - NbSe_2$  and  $2H - TaS_2$ , this charge density wave energy gap has been reported to

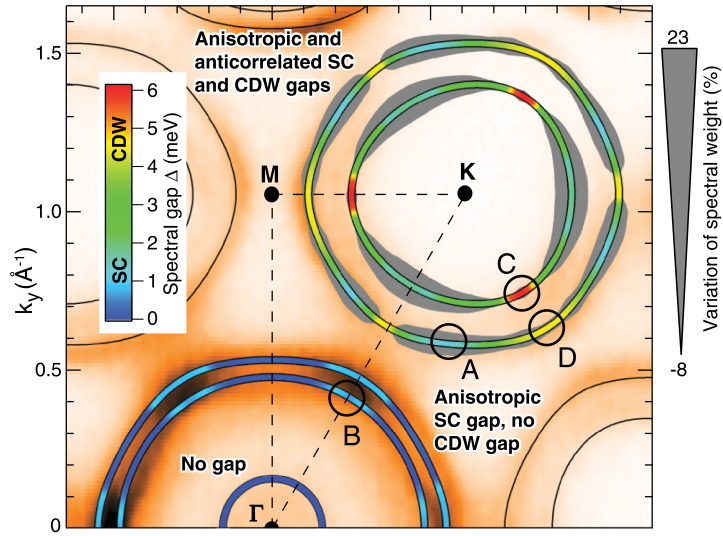


FIGURE 3.7: **Variation of the energy gap in  $2H\text{-NbSe}_2$**  [37]

Spectral gaps corresponding to charge density wave and superconducting phenomena in  $2H\text{-NbSe}_2$ . Observed gaps are anisotropic in momentum. The charge density wave energy gap, colored in yellow-red, opens up only in specific locations in the vicinity of the K-point, as at the intersection of the line joining K-M momentum points and the Inner K-centered Fermi surface barrel (circle - C). Charge density wave gap is non-existent about the  $\Gamma$ -point.

demonstrate a variation of its magnitude, depending on the momentum location it has been measured. [37, 46, 133, 145, 161–167].

In order to probe for a possible momentum dependence of the  $\Delta_{CDW}$ , specific points in the momentum space were chosen about both  $\Gamma$  and K symmetry points. Then energy distribution curves corresponding to these points, taken at the CDW state ( $T < T_{CDW}$ ) were examined. Such normalized (Fermi function divided) EDCs are given in Fig. 3.6(d,e,f, and g), while 3.6(h,i,j, and k) shows raw EDCs before normalization.

Previously reported ARPES studies have also shown evidence for similar preferential existence of  $\Delta_{CDW}$  which opens up only around the K-point, for series of related material including  $2H\text{-NbSe}_2$ ,  $2H\text{-TaS}_2$ ,  $2H\text{-TaSe}_2$  [133, 145, 146] and  $\text{Na}_x\text{TaS}_2$  [164, 165] as well. As discussed above, the fully gapped nature of K-centered Fermi surface barrels in

$2H - \text{TaS}_2$ [92] here is evident by finite down-shift of all the K-centric EDC peaks, with respect to the chemical potential as in Fig. 3.6(d), (e) and (f), for all the circumferential and radial momentum locations measured. In contrast to this, for the case of  $2H - \text{NbSe}_2$ , it has been observed that  $\Delta_{CDW}$  opens up only on some specific momentum locations[37, 133] such as at the intercept of the inner K-barrel and the hypothetical line between K-M symmetry points as in the Fig. 3.7.

In comparison, when accounting for the charge density wave energy gap,  $2H - \text{TaS}_2$  has its K-centered Fermi surface barrels are fully gapped, despite the anisotropic gap-size variation, whereas in  $2H - \text{NbSe}_2$ , the K-neighborhood was only partially gapped. On the other hand, the  $\Gamma$ -centered Fermi surface barrels were gapless in both TMD material.

This difference of gapping between very similar compounds can be attributed to the differences in electronic orbits in candidate compounds[92] as elaborated in the section 3.4.5. In general, it can be concluded that the coexistence of gapped and gapless regions of Fermi surfaces are characteristic for the incommensurate CDW phase in  $2H$ -TMD materials, as similar features have been reported for all three compounds  $2H - \text{TaS}_2$ ,  $2H - \text{NbSe}_2$  and  $2H - \text{TaSe}_2$  [133, 141, 146].

#### 3.4.2.4 Particle – Hole Asymmetry of the CDW Energy Gap

The relative position of the minima of an EDC with respect to the chemical potential can be used to determine whether the CDW energy gap is particle-hole symmetric. Consider some representative EDCs of  $2H - \text{TaS}_2$  in the vicinity of  $\Gamma$  and K points given in Fig. 3.8(b) and (c). These EDCs are taken at the momentum locations denoted on the schematic Fig. 3.8(a); as a yellow dot, on the inner  $\Gamma$ -centered Fermi surface

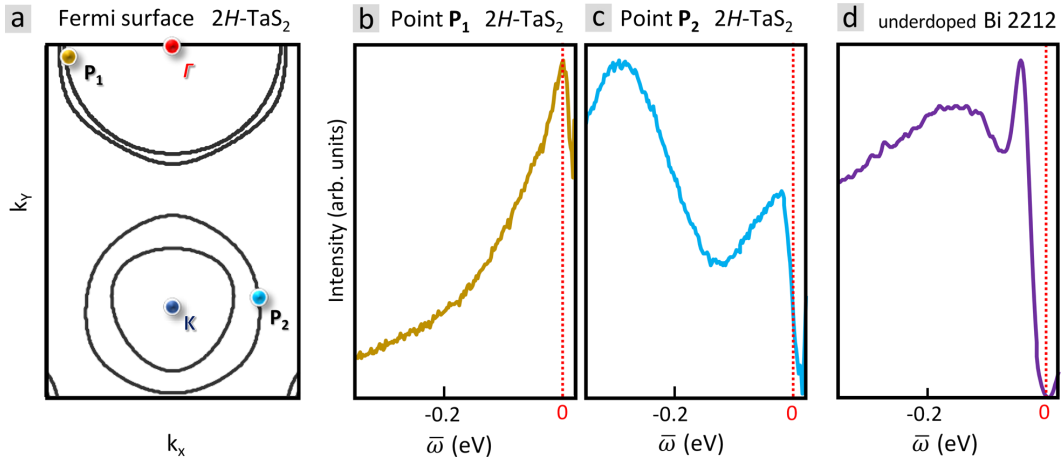


FIGURE 3.8: **Symmetry of energy gaps in charge density wave state Vs. superconducting state.**

(a) Relevant momentum locations for (b) and (c), marked on the schematic Fermi Surface of  $2H - \text{TaS}_2$ . (b) A representative EDC taken on the inner  $\Gamma$ -centric Fermi surface barrel of  $2H - \text{TaS}_2$ , at the momentum point marked as P<sub>1</sub> on (a). (c) An EDC taken on the outer K-barrel of  $2H - \text{TaS}_2$ , at P<sub>2</sub> on (a). (d) An EDC taken at an antinode of the superconducting gap of an underdoped Bi 2212 high temperature superconductor sample. In (b) and (c), the charge density wave energy gap is asymmetric while in (d), the superconducting energy gap is symmetric about the chemical potential,  $\bar{\omega} = 0$  (marked by a red dotted line).

barrel and as a light blue dot on the outer  $\Gamma$ -centered Fermi surface barrel, respectively. It is clear that for both K and  $\Gamma$ -centric Fermi surface barrels, minima of all the EDCs are shifted above from the chemical potential ( $\bar{\omega} > 0$ ). This is evident from both Fig. 3.8(b and c), as well as from Fig. 3.6(d,e,f, and g). This shift reveals that the charge density wave energy gap,  $\Delta_{CDW}$  is particle - hole asymmetric with respect to the the chemical potential[92]. Such an asymmetry is expected for these systems as a charge density wave instability involves a finite momentum ( $\mathbf{q}$ ) transfer[45], where the  $\mathbf{q}$  does not match with one of the CDW wavevectors. Similar asymmetry of  $\Delta_{CDW}$  has been observed for  $2H - \text{NbSe}_2$  as well [46, 132, 146, 150].

The behavior of the charge density wave energy gap is quite different from a superconducting energy gap, which is particle-hole symmetric because it is a zero-momentum transfer ( $\mathbf{q} = 0$ ) instability[45]. Compare these EDCs on Fig. 3.8(b) and (c) from charge

density wave material with an EDC from a superconducting material, shown on the Fig. 3.8(d). This system is underdoped BISCO (Bi 2212:  $\text{Bi}_2\text{Sr}_2\text{CaCu}_2\text{O}_{8+\delta}$ ) cuprate high temperature superconductor (HTSC) with superconducting critical temperature  $T_C = 87\text{K}$ [45]. (Note: the superconducting energy gap of such a cuprate HTSC is anisotropic along the Fermi surface and the shown EDC is taken at an antinode where this superconducting gap attains its maximum value.) Further, the absence of Fermi surface nesting in transition metal dichalcogenides as stated in the section 3.3.3 can be understood in terms of this particle–hole asymmetry of the  $\Delta_{CDW}$  as well.

### 3.4.3 Temperature Dependence of the CDW Energy Gap

In search of any temperature evolution of the charge density wave energy gap, a momentum point on the outer Fermi surface barrel around the K–point was selected as indicated on the Fig. 3.9(a) with a light blue point,  $P_a$ . A series of EDCs for this point was taken for a range of temperatures from 12 K to 100 K [92] and are shown in the Fig. 3.9(b). In the charge density wave phase, For  $T < T_{CDW}$ , the CDW coherence peak was significant. When temperature was increased, peak height got decreased, and eventually diminished when  $T = T_{CDW}$ . This behavior is expected.

For the further increase in temperature above  $T_{CDW}$ , the energy distribution curve was expected to transform into a peak-less EDC, as no charge density wave is observed at these elevated temperatures. But in contrary to the expected behavior, a ‘*kink*’ feature was visible even in higher temperature EDCs. A kink indicates a suppression of density of states, as can easily be seen in the Fig. 3.9. This kink appeared at the same energy  $\bar{\omega}$  location where the low-temperature peak used to appear. For much higher temperatures, further evolution of the EDC stopped, but the kink remained in place

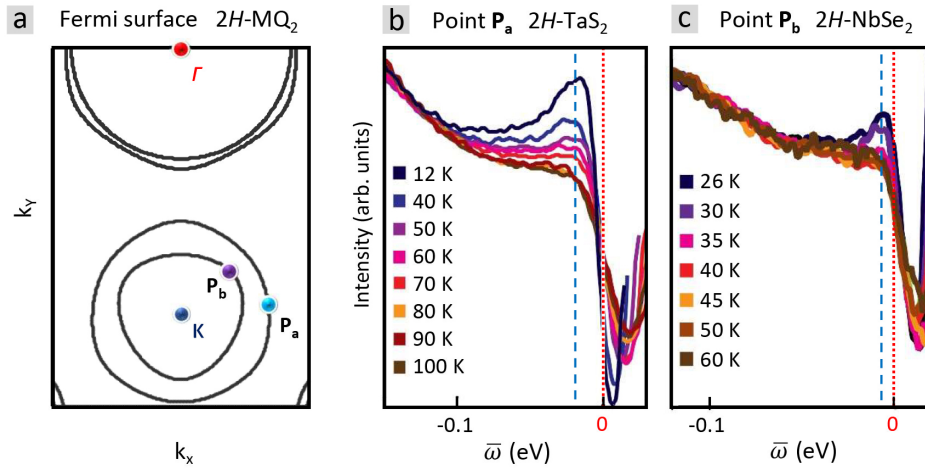


FIGURE 3.9: **Temperature dependence of the energy distribution curves.** (a) Fermi surface schematic of  $2H - MQ_2$ , indicating momentum locations where EDCs in (b) and (c) are taken. (b) Series of EDCs taken at different temperatures for  $2H - TaS_2$  at the momentum point  $P_a$ , marked as a light blue dot on (a) on the outer K-centered Fermi surface barrel. (c) Series of EDCs taken at different T for  $2H - NbSe_2$  at the momentum point  $P_b$ , marked as a purple dot on (a) on the inner K barrel[146]. In both (b) and (c) for both samples, when  $T < T_{CDW}$ , the CDW coherence peak is pronounced and diminishes When  $T$  is increased. For  $T > T_{CDW}$ , the peak evolves in to a kink feature. Both the peak and the kink lie approximately on the same energy location for all the temperatures, as marked by a blue dashed line.

for the range of temperatures observed. The existence of a low-energy suppression of spectral weight, even for temperature  $T > T_{CDW}$ , is commonly known as the *pseudogap* behavior. Besides the pseudogap, the particle-hole asymmetry of the charge density wave energy gap, mentioned in the section 3.4.2 was also significant for the entire range of temperatures investigated.

Similar observations have been reported for  $2H - NbSe_2$  [133, 146] and for  $2H - TaSe_2$  [140] as well. Fig. 3.9(c) shows a series of EDCs over a comparable range of temperatures for  $2H - NbSe_2$ [146]. These were taken on the inner K-centric Fermi surface barrel, indicated as a purple point  $P_b$  on Fig. 3.9(a). Apart from the material class of transition metal dichalcogenides, This kind of pseudogap behavior has been observed in other

materials such as under-doped cuprate high temperature superconductors (HTSCs)[168–171] as well.

### 3.4.4 Origin of the Pseudogap

A charge density wave state, as elaborated in the section 1.1.2, can be characterized with an order parameter,  $\Psi$  as followed from the equation 1.3.

$$\Psi = \rho_0 \cos(\mathbf{q}_{CDW} \cdot \mathbf{r} + \phi) \quad (3.3)$$

with an amplitude  $\rho_0$  given by,

$$\rho_0 = \frac{2\Delta_{CDW}}{g(|\mathbf{q}|)} \quad (3.4)$$

where,  $\Delta_{CDW}$  is the charge density wave energy gap,  $\mathbf{q}_{CDW}$  is the CDW wave vector,  $\mathbf{r}$  is a position vector,  $\phi$  is the phase factor, and parameter  $g(|\mathbf{q}|)$  is a measure of momentum dependent electron-phonon coupling.

Such a charge modulation can disappear due to the loss of either the amplitude,  $\rho_0$  or the randomization of the phase,  $\phi$ . In weak coupling theory, destruction of CDW order via phase randomization is unlikely. However, this can, in principal, happen in a strongly coupled CDW system.

for  $T < T_{CDW}$ , the charge density wave energy gap  $\Delta_{CDW}$  exists in association with a true long-range ordered CDW phase. On the other hand, for  $T > T_{CDW}$ , though the phase coherence is diminished in the long range, the local amplitude,  $\rho_0$  may still remain

finite. As above equation 3.4 reveals, CDW energy gap is proportional to this local amplitude ( $\Delta_{CDW} \propto \rho_0$ ) So, even for  $T > T_{CDW}$ , a short range charge density ordering can still be expected, despite the long range phase coherence being suppressed. Therefore, a pseudogap can be observed due to such a short-range modulations as discussed in the section 3.4.3.

Supporting observations for such short range charge ordering have been reported in previous studies of  $2H - \text{TaS}_2$  [11] and  $2H - \text{NbSe}_2$  [146] where transmission electron microscopy (TEM) and scanning tunneling microscopy (STM) studies have identified peaks related to a charge density wave super-lattice, even for temperatures,  $T > T_{CDW}$  in respective systems.

It can be suggested that the transition from long-ranged CDW state to the higher temperature pseudogap state in both incommensurate charge density wave systems and underdoped cuprate HTSCs can thus be viewed as “a coherent and gapped electronic state in low temperature, transforming to an incoherent, yet still gapped state in a higher temperature, by means of losing the long-range phase coherence while holding some reminiscent local ordering”.

### 3.4.5 Orbital Selectivity and the Anisotropy of the CDW Energy Gap

In the context of superconductivity, BCS theory explains the weak coupling limit, while the Eliashberg theory explains the strong coupling limit. Analogous to this, in the context of charge density wave phenomenon, Peierls like Fermi surface nesting is the general model for the weak coupling limit (see the section 3.3.3). At least for the charge density wave phenomena in transition metal dichalcogenides [45, 47, 92], a more specific tight binding model[132, 150] which considers both the orbital dependence of electrons,

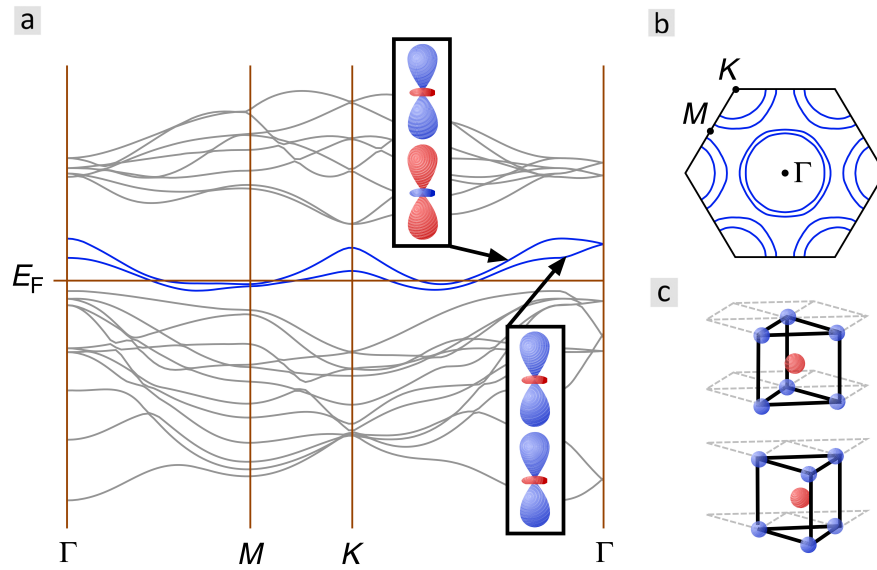


FIGURE 3.10: **Tight binding model band structure for 2H-NbSe<sub>2</sub>[150].** (a) Blue lines indicate two band crossing the Fermi level. These arise from Nb- $d_{z^2}$  orbitals which are aligned with crystallographic  $c$  axis as shown as insets. (b) The Fermi surface schematic of 2H - TaS<sub>2</sub>,  $d_{z^2}$ . (c) The layered atomic structure, with two transition metal (Nb) atoms per unit cell, which gives rise to bonding and anti-bonding orbitals and bands highlighted on (a).

participate in charge density wave pairing -and- the momentum dependence of electron-phonon interactions can sufficiently explain above observations. It can tackle both the similarities among candidate TMD compounds, 2H - TaS<sub>2</sub> and 2H - NbSe<sub>2</sub> as well as the differences between them[92].

As explained in the section 3.3.1,  $d_{z^2}$  electronic orbitals of transition metal (Ta and Nb) cations give rise to K-centered Fermi surface barrels. The modeled band structure[150] for 2H - NbSe<sub>2</sub> and the nature of these constituting orbitals are shown in the Fig. 3.10. Two bands, corresponding to two barrels are expected because, two transition metal atoms exist in a unit cell. On the Fermi surface, near the K-symmetry point, Inner Fermi surface barrel is derived from bonding orbitals, and the outer barrel comes from anti-bonding orbitals. Here, for the case of 2H - NbSe<sub>2</sub>, these  $d_{z^2}$  orbitals are oriented

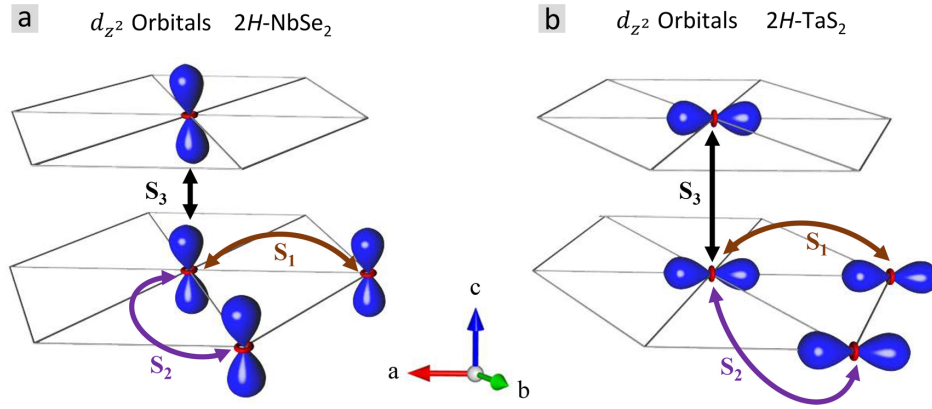


FIGURE 3.11: **Possible orientations for  $d_{z^2}$  orbitals of three neighboring transition metal cations** (Nb and Ta in this context). These orbitals are associated with K-centered Fermi surface barrels. Overlap integrals appear in the tight-binding description are marked as  $S_1$ ,  $S_2$  and  $S_3$  (values of these integrals are given in the Table 1). **(a)** In  $2H - \text{NbSe}_2$ ,  $d_{z^2}$  orbitals are aligned with crystallographic  $c$  axis. note that  $S_1 = S_2$  due to the geometry. **(b)** In  $2H - \text{TaS}_2$ ,  $d_{z^2}$  orbitals lie on the  $a$ - $b$  plane.

along the  $c$ -axis of the crystallographic coordinate system. This band structure and orbital orientations are elaborated in the Fig. 3.11(a).

But in the case of,  $2H - \text{TaS}_2$  the smaller size of the Fermi surface barrel and the proximity to a high-symmetry point cause its  $d_{z^2}$  orbitals to lie on the crystallographic  $ab$ -plane [134, 150, 172, 173] as shown in comparison to the former case, on the Fig. 3.11(b). This rotation of the orbital orientation in  $2H - \text{TaS}_2$  has been previously considered to give rise to some other phenomena such as the presence of a hidden one-dimensional order[172], and specific orbital order type[173], as well.

This drastic difference of  $d_{z^2}$  orbital orientation results in a difference of strengths of the electron-phonon coupling for K-centered Fermi surface barrels between  $2H - \text{TaS}_2$  and  $2H - \text{NbSe}_2$ . In the table 3.1, Orbital overlap Integrals  $S_1, S_2$  and  $S_3$  are expressed in terms of  $d-d$  orbital character ( $\sigma, \pi$  and  $\delta$ ). When considering only the nearest neighbor overlaps at the K- momentum point, diagonal entries of the overlap matrix  $S(k)$  has

the value  $(1 + 2S_2 - S_1)$  while off-diagonal elements are  $S_3$ [92]. In general, in-plane interactions are represented by the diagonal elements while out-of-plane interactions are determined by off-diagonal elements. Relative magnitudes of electron-phonon couplings are determined by the squared ratio of these components in  $S(k)$ . Once this method is applied to K-centered inner and outer Fermi surface barrels, the ratio of charge density wave energy gap sizes between both barrels can be determined[132, 150].

TABLE 3.1: Comparison of orbital overlap integrals in  $2H-NbSe_2$  and  $2H-TaS_2$ .

S	$2H - NbSe_2$	$2H - TaS_2$
$S_1$	$\frac{1}{4}(dd\sigma)_1 + \frac{3}{4}(dd\delta)_1$	$(dd\sigma)_1$
$S_2$	$\frac{1}{4}(dd\sigma)_1 + \frac{3}{4}(dd\delta)_1$	$\frac{1}{64}(dd\sigma)_1 + \frac{9}{16}(dd\pi)_1 + \frac{27}{64}(dd\delta)_1$
$S_3$	$(dd\sigma)_2$	$\frac{1}{4}(dd\sigma)_2 + \frac{3}{4}(dd\delta)_2$

Composition of the orbital overlap integrals  $S_1, S_2$  and  $S_3$  are expressed in terms of  $(dd\sigma), (dd\delta)$  and  $(dd\pi)$  orbital character for K-centric Fermi surface barrels in  $2H-NbSe_2$  and  $2H-TaS_2$ . Spacial orientations of these orbital overlap integrals are as shown in the schematic diagram, Fig. 3.11.

Such a tight-binding model to the band structure was utilized to estimate the strength of this effect[174]. For both  $2H - TaS_2$  and  $2H - NbSe_2$ , the same set of orbital overlap integrals between adjacent  $d$ -orbitals were used. To compare gap ratio between inner and outer barrels within both material around the K-point, the procedure was to set integral  $S_1$  of  $2H - TaS_2$  equal to  $S_3$  of  $2H - NbSe_2$ . More specifically, as understood from the table 3.1, set  $(dd\sigma)_1 = (dd\sigma)_2 \approx 0.5$  and set all others integrals to be zero. For  $2H - NbSe_2$  this analysis predicted a CDW energy gap ratio of 6.8 between inner and outer barrels. This value agrees with ARPES studies[37, 133] of  $2H - NbSe_2$  where

$\Delta_{CDW}$  opens up only in the inner barrel. On the other hand, for  $2H - \text{TaS}_2$ , this gap ratio was smaller ( $\sim 2.7$ ) compared to partially gapped  $2H - \text{NbSe}_2$ . This calculation also supports experimental observations[92] mentioned in the section 3.4.2, since both barrels are fully gapped throughout the K-centric barrel system in  $2H - \text{TaS}_2$ .

### 3.5 Summary

In summary, an ARPES study on the charge density wave (CDW) phenomenon in the transition metal dichalcogenide (TMD) compound  $2H - \text{TaS}_2$ , with emphasis on momentum and temperature dependencies is being reported. This analysis was done in comparison to similar TMDs,  $2H - \text{NbSe}_2$ , and  $2H - \text{TaSe}_2$ .

Several universal phenomena, generalizable among the entire family of layered transition metal dichalcogenides with  $2H$  polytype, were found.

- i** In the momentum space, Fermi pockets of electrons and holes were segregated into concentric double barrel patterns about K and  $\Gamma$  high symmetry points.
- ii** The charge density wave energy gap ( $\Delta_{CDW}$ ) existed only on some of the Fermi surface barrels; K-centric Fermi surface barrels were fully, or at least partially gapped while  $\Gamma$ -centric barrels remains ungapped.
- iii** Simple Peierls like Fermi surface nesting model was not sufficient in the explanation of the charge density wave formation in transition metal dichalcogenides.
- iv** The charge density wave energy gap was particle-hole asymmetric with respect to the chemical potential, whenever the gap opens up.

- v The *Pseudogap* behavior (persistence of the  $\Delta_{CDW}$  for  $T > T_{CDW}$ ) was observed due to short-range charge ordering in local neighborhoods, despite the long-range phase coherence being diminished at elevated temperatures.

Apart from the general features listed above, noticeable differences between comparable transition metal dichalcogenide compounds were observed as well,

- i In the case of  $2H - \text{TaS}_2$ , The charge density wave energy gap opened up at each momentum location on both k-centric Fermi surface barrels. This is in drastic contrast to the CDW energy gap of  $2H - \text{NbSe}_2$ , where existence and magnitude of  $\Delta_{CDW}$  was observed to be momentum specific and so, even K-barrels were only partially gapped.
- ii When expressed with respect to their own lattice dimensions,  $\Gamma$ -centric Fermi surface barrels were almost the same size among both compounds, while the size of K-centric Fermi surface barrels for  $2H - \text{TaS}_2$  were observed to be smaller than the size of K-barrels in  $2H - \text{NbSe}_2$ .

These differences can be understood using a tight binding model with strong electron-phonon coupling which takes the differences of orbital orientations between these materials into account. These differences in orbital arrangements and its consequences on the momentum space might be the determining factor of the charge density wave transition temperature.

---

## Chapter 4

# Electron–Phonon Coupling in $2H\text{-TaS}_2$

### 4.1 Background

Information regarding interactions between an electron and some collective excitations in a system, such as phonons, magnons, plasmons, etc., can be extracted by carefully analyzing electronic dispersion. Typically, such interactions are expected to renormalize electronic dispersion. The shift in this renormalized band dispersion with respect to the bare dispersion can be considered as a measure of the strength of the coupling between electrons and the collective excitation.

In addition, a modification to electronic state lifetimes will follow. Hints for the existence of such collective modes can be captured using techniques like heat capacity measurements and tunneling spectroscopy, but these methods inherently provide information averaged over the entire Fermi surface of the system. On the other hand, ARPES can resolve momentum specific features making it a unique probe of mapping finer details of the Fermi surface with energy and momentum resolution.

As followed from the previous chapter 3, Angle Resolved Photo-Emission Spectroscopy (ARPES) was used to observe energy, momentum[45] and temperature[92] dependence of the electronic structure of 2H – TaS<sub>2</sub> in order to investigate the general and compound-specific features of its charge density wave energy gap. Upon further observations into the same material system, a strong coupling of band electrons to some collective modes which lead to the renormalization of the energy dispersion was observed. Hence, a detailed analysis of the electronic band renormalization in momentum space was called for, in order to gather the details on these underlying collective modes.

The study presented here depicts direct evidence for strong coupling between electrons and phonons. The observation of temperature independence of these renormalization signatures further support this phononic origin. Similar signatures of electron-phonon coupling have been observed in other 2H-Polytypes. Phonons are the quasi-particle representation of quantized lattice vibrations. In general, phonons occur in two different categories, *optical* and *acoustic*. Acoustic phonons exhibit a phonon dispersion;  $\omega(k) \rightarrow 0$  as  $k \rightarrow 0$ . On the other hand, optical phonons occur only above a certain cut-off frequency.

Beyond the material class of transition metal dichalcogenides, such signatures of electronic band renormalization have been observed in a wide range of materials including conventional superconductors[175], cuprate[118, 158, 176] and pnictide[177] high temperature superconductors, metals [178, 179] and Manganites [180]. In the case of TMDs, band renormalizations in 2H – NbSe<sub>2</sub>[37, 181] and 2H – TeSe<sub>2</sub> [181, 182] has been reported. This study employees self-energy analysis[47] on ARPES data to identity band renormalizations in 2H – TaS<sub>2</sub> and then characterize observed features to be due to a phononic origin.

## 4.2 Self-Energy of the Band Renormalization

### 4.2.1 Self-Energy and the Spectral Function

The effect exerted by a collective mode, via coupling to the electronic dispersion of a system can be captured using the a microscopic attribute called ‘single particle self-energy’, symbolized as  $\Sigma(\mathbf{k}, \bar{\omega})$ . In general, self-energy is a function of both energy,  $\bar{\omega}$  and momentum,  $\mathbf{k}$ . and is complex valued [127].

- The real part:  $\Sigma'(\mathbf{k}, \bar{\omega})$ , is a measure of the deviations from the bare electronic dispersion due to the interaction with collective modes.
- The imaginary part:  $\Sigma''(\mathbf{k}, \bar{\omega})$ , is the modification of the life-times of electronic states due to the electron-collective mode coupling.

Note that, the energy parameter  $\bar{\omega}$  here is the energy with respect to the chemical potential,  $\mu$ .

$$\bar{\omega} = \omega - \mu \quad (4.1)$$

The intensity  $I(\mathbf{k}, \bar{\omega})$  of an ARPES signal can generally be approximated as:

$$I(\mathbf{k}, \bar{\omega}) = M(\mathbf{k})A(\mathbf{k}, \bar{\omega})f(\bar{\omega}) \quad (4.2)$$

where  $M(\mathbf{k})$  is the dipole matrix element and  $A(\mathbf{k}, \bar{\omega})$  is the spectral function, while  $f(\bar{\omega})$  is the Fermi Dirac distribution function.

$$f(\bar{\omega}) = \frac{1}{1 + e^{\frac{\bar{\omega}}{kT}}} = \frac{1}{1 + e^{\frac{(\omega - \mu)}{kT}}} \quad (4.3)$$

The spectral function can be further expanded in terms of both the real and imaginary self-energy components as [69, 118, 158, 176]:

$$A(\mathbf{k}, \bar{\omega}) = \frac{\Sigma''(\mathbf{k}, \bar{\omega})}{(\bar{\omega} - \epsilon_{\mathbf{k}} - \Sigma'(\mathbf{k}, \bar{\omega}))^2 + \Sigma''(\mathbf{k}, \bar{\omega})^2} \quad (4.4)$$

where,  $\epsilon_{\mathbf{k}}$  is the un-renormalized (bare) electronic dispersion in the absence of any collective mode interactions.

### 4.2.2 Extraction of the Self-Energy Components from ARPES Data

Consider one-dimensional line graph representations of ARPES data (see the section 2.2). A momentum distribution curve (MDC), is an intensity map,  $I(k_x)$  for a specific value of  $k_y$  and  $\bar{\omega}$ . On the other hand, an energy distribution curve (EDC) is another type of a line graph,  $I(\bar{\omega})$  for a fixed coordinate of  $k_x$  and  $k_y$ . In principle both line graphs EDCs, and MDCs can be used to extract quasi-particle self-energies responsible for band renormalization. An MDC analysis near the chemical potential was employed in this study.

In principle, both of the real ( $\Sigma'$ ) and imaginary ( $\Sigma''$ ) components of the self-energy can be found from ARPES data. However, in practice, such an evaluation can be very difficult to handle if the self-energy depends on both energy and momentum. The extraction of useful information on self-energy becomes rather straightforward when the self-energy behaves practically momentum-independent.

Given this condition is satisfied, and further, if the data were taken in the neighborhood of the Fermi momentum  $k_F$ , or in other words in the low binding energy region near chemical potential, it is safe and simple to approximate the above stated bare electronic dispersion,  $\epsilon_{\mathbf{k}}$  as:

$$\epsilon_{\mathbf{k}} \sim v_F^0 (|\mathbf{k}| - k_F) \quad (4.5)$$

here,  $k_F$  is the Fermi momentum and  $v_F^0$  is the bare Fermi velocity.

### 4.2.3 Self-Energy and the Lineshapes of MDC Peaks

If the following two conditions are satisfied for ARPES momentum distribution curves (MDCs):

- The real,  $\Sigma'(\mathbf{k}, \bar{\omega})$  and imaginary,  $\Sigma''(\mathbf{k}, \bar{\omega})$  components of the self-energy, as well as the dipole matrix elements,  $M(\mathbf{k})$  shows no significant dependence on the momentum,  $\mathbf{k}$ .
- The region where MDCs were taken is strictly in the vicinity of the chemical potential of the system, or in other words;  $|\mathbf{k}| \sim k_F$ , where  $k_F$  is the Fermi momentum.

The peaks in such an MDC can be successfully approximated with simple Lorentzian line shapes. To further clarify this point, consider the definition of the simple Lorentzian model:

$$L(x) \sim \frac{\sigma}{(x - x_0)^2 + \sigma^2} \quad (4.6)$$

where,  $x$  is the independent variable,  $x_0$  is the center of the peak and  $\sigma$  is the line width (FWHM).

Comparison of this form (equation 4.6) to the spectral function expressed in the equation 4.4 reveals the following features about self-energy components.

- The real part of the self-energy,  $\Sigma'(\mathbf{k}, \bar{\omega})$  is a measure of the deviation from the bare electronic dispersion and so,  $\Sigma'(\mathbf{k}, \bar{\omega})$  can be found by subtracting the expected bare dispersion ( $\epsilon_{\mathbf{k}}$ ) from the experimentally observed (i.e.: renormalized) dispersion,  $\bar{\omega}(\mathbf{k})$ .

$$\Sigma'(\mathbf{k}, \bar{\omega}) = \bar{\omega}(\mathbf{k}) - \epsilon_{\mathbf{k}} \quad (4.7)$$

- The imaginary part of the self-energy,  $\Sigma''(\mathbf{k}, \bar{\omega})$  serves as a width parameter( $\sigma$ ).

$$\Sigma''(\mathbf{k}, \bar{\omega}) \sim \sigma \quad (4.8)$$

Call the widths obtained from the Lorentzian fits to momentum distribution curves:  $W(\bar{\omega})$ . It can be expressed as[69, 118, 158, 176]:

$$W(\bar{\omega}) = \frac{\Sigma''(\bar{\omega})}{v_F^0} \quad (4.9)$$

Which is a measure of the modification of electronic state lifetimes as mentioned above.

It should be noted that, in reality, the ARPES data will be subjected to additional broadening other than due to the lifetimes, upon various physical and systematic factors such as the detector resolution. If these broadening mechanisms are considered to be of Gaussian type, The *Voigt* model, which is a convolution of a Gaussian with a Lorentzian, happens to be a better fitting model for experimental MDC peaks. This model is characterized by two independent width parameters (one Gaussian width and one Lorentzian), and several analysis methods can be utilized to isolate the Lorentzian width, which holds electronic state lifetime information (see the section 2.1.5.1).

### 4.3 Identification of the Phonon Modes in 2H-TaS<sub>2</sub>

#### 4.3.1 Tracing the Electronic Band Dispersion

Consider the momentum cut marked on the Fermi surface blueprint as a red dashed line on the Fig. 4.1(a). A series of momentum distribution curves (MDCs) along this momentum cut, as well as along similar cuts on energy iso-surfaces (CEIMs) with stronger binding energies ( $\bar{\omega} < 0$ ) were taken. Orientations of these MDC-cuts are visualized on the Fig. 4.1(b) where few representative energy iso-surfaces (i.e., constant energy intensity maps - CEIMs) are stacked. Resultant representative MDCs are shown on the Fig. 4.1(c), with arbitrary baseline shifts along the vertical (energy) axis.

Such MDCs were taken for a series of CEIMs of energies ranging from  $\bar{\omega} = 0$  (i.e., on the Fermi surface), all the way past -0.13 eV. Resultant MDCs are shown on the Fig. 4.1(c). Data points which are represented with blue markers were then fitted with Voigt fits, given as red lines. The momentum locations of these fitted peaks can be identified for each MDC. (i.e., for each energy).

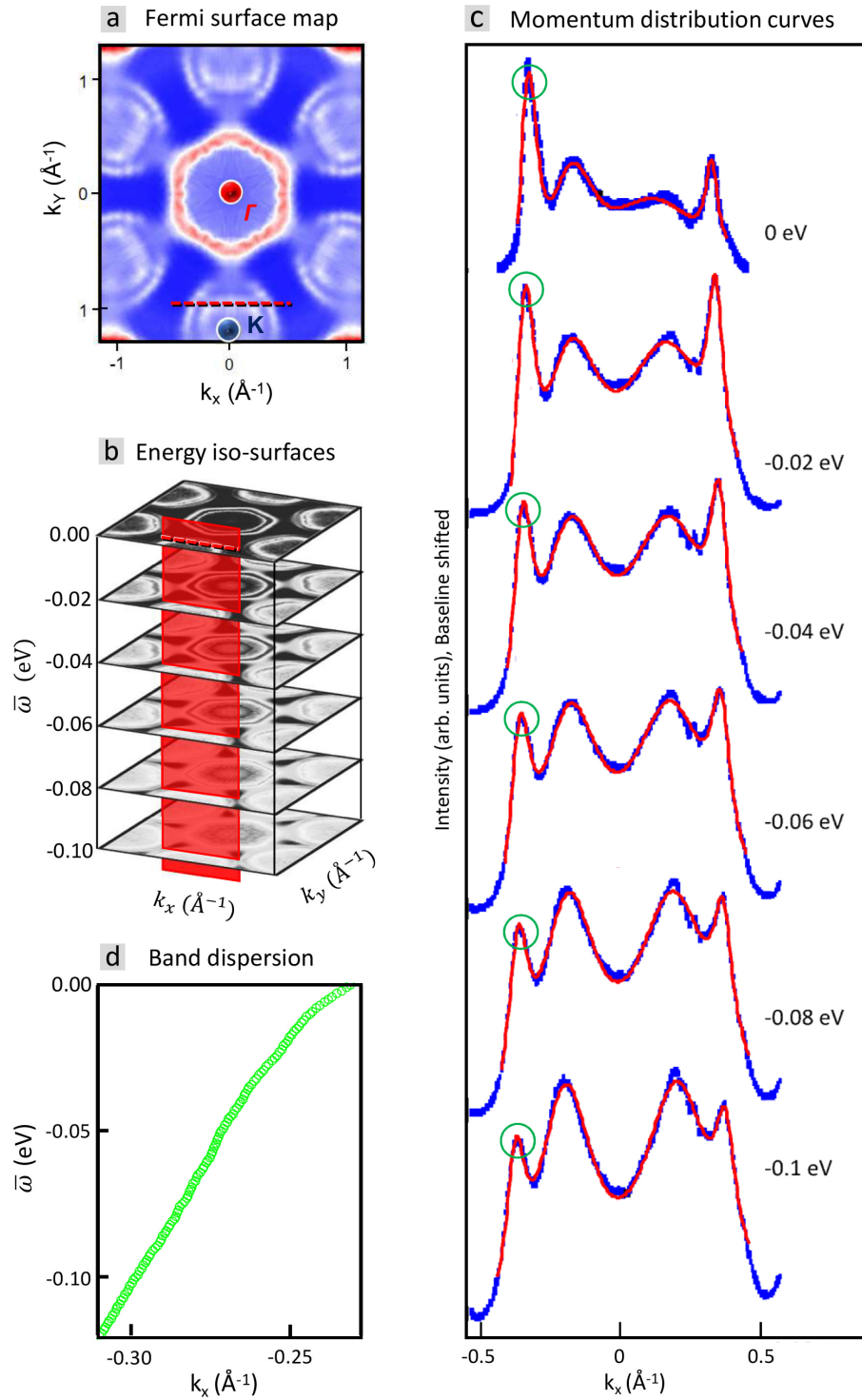


FIGURE 4.1: **Band reconstruction of 2H-TaS<sub>2</sub> using momentum distribution curves (MDCs).**

Please see the next page for the details.

### Band reconstruction of 2H-TaS<sub>2</sub> using momentum distribution curves (MDCs).

Continued from the previous page...

(a) The Fermi surface map with a momentum cut (red dashed line) indicated. Momentum distribution curves (MDCs) shown in (c) were taken along this momentum cut, for a series of energy ( $\bar{\omega}$ ) values. (b) The stack of energy iso-surfaces (CEIMs) considered for the MDC analysis. The red plane is defined by a  $K_y$  momentum held constant, and MDCs taken on this plane, for each energy value ( $\bar{\omega}$ ) are shown in (c). Note that the top CEIM at  $\bar{\omega} = 0$  is the same as the Fermi surface in (a). (c) Some representative MDCs taken for few different energy values. Data are represented as blue markers, while *Voigt* fits are given as red lines. curves are baseline shifted for the visual clarity. Momentum  $K_x$  is the independent variable, while  $K_y$  momentum component was constant throughout. Each MDC is characterized by the the energy. (d) Observed electronic band dispersion (green circles) of the left most peak, traced by tracking the corresponding peak locations of MDCs, such as the curves shown in (c) for a range of energies. (Note: this is the band due to the outer K-centric Fermi surface barrel)

---

The experimental band dispersion for the corresponding peak,  $\bar{\omega}(k)$  can be obtained by plotting the MDC energy values (in eV), against corresponding peak positions in momentum (in  $\text{\AA}^{-1}$ ). An example band trace constructed using this method is plotted on the 4.1(d), in green circles. The band depicted is the left outer K-centered Fermi surface barrel of 2H - TaS<sub>2</sub>.

### 4.3.2 Renormalization Signatures in the Electronic Band Dispersion

Experimental band trace above is superimposed on an EMIM (energy momentum intensity map) on the Fig. 4.2(b). The EMIM depicts the intensity profile of the barrel wall corresponding to the band. A zoomed-out EMIM which shows the experimental band profile of the entire K-centric Fermi barrel system is given on the Fig. 4.2(a) as a reference. The MDC mapped band dispersion (green circles) shows a good agreement with this intensity profile. Note that, this EMIM can be alternatively visualized as the ARPES intensity profile on the red colored intersection plane marked on the Fig. 4.1(b).

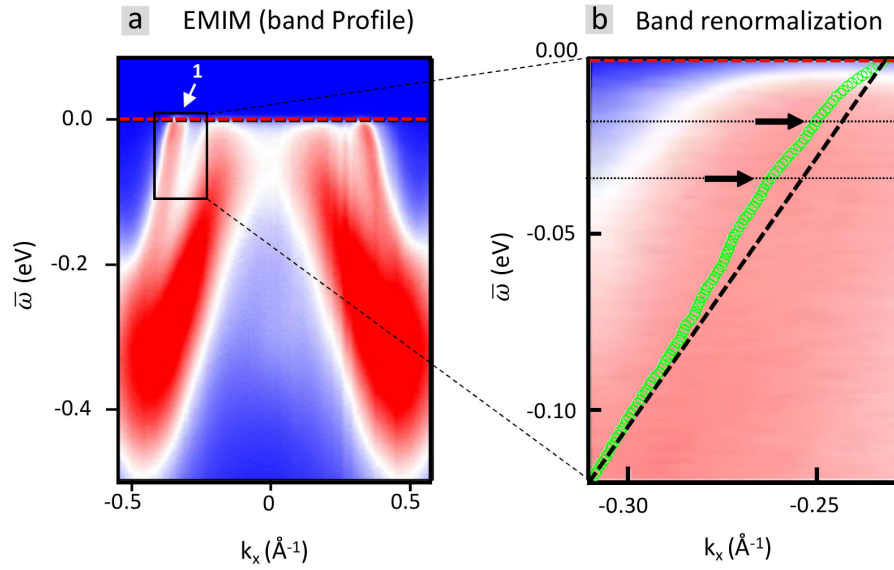


FIGURE 4.2: **Band renormalization signatures of 2H–TaS<sub>2</sub> due to the presence of collective modes** (a.k.a., *kinks*).

(a) An ARPES energy–momentum intensity map (EMIM) depicting the band profile of the K–centric Fermi surface barrel system of 2H – TaS<sub>2</sub>. (b) Line of green circles is the experimental electronic dispersion trace, due to the band corresponding to the outer K–centric Fermi surface barrel. Approximated bare band dispersion is shown by black dashed line. Band renormalization signatures (i.e.: the *kink* locations) are marked with horizontal black arrows. Band traces are superimposed on a portion of the EMIM shown on (a), zoomed in to the neighborhood of the Fermi crossing 1. Fermi level is marked with a red dashed line on both figures.

An elaborate discussion on the experimental band structure of 2H – TaS<sub>2</sub> is provided in the section 3.3 while the Fig. 3.3 summarize the details.

Expected bare-band dispersion is also plotted as a black dashed line on the Fig 4.2(b). Note that this kind of MDC analysis is valid only in the vicinity of the chemical potential as given by the equation 4.5. In this tight region under analysis, the bare band can be approximated with a straight line segment with a slope equal to the Fermi velocity ( $v_F^0$ ). The bare band (black dashed line) will pass through the same Fermi crossing (i.e., same energy-momentum coordinate) as the experimentally observed renormalized band (trace of green circles). Finer details of this band dispersion show multiple places with drastic slope changes with significant deviations from the bare dispersion. These

renormalization features are known as *kinks* and are due to the scattering of electrons from the collective modes in the system. Out of several renormalization signatures, two of the most prominent kinks are indicated with black horizontal arrows on Fig. 4.2(b), These kinks are identified at energies  $\bar{\omega} \sim 18$  meV and  $\sim 35$  meV.

Reported observations from Raman spectroscopy data [183] and calculations of theoretical phonon energies[184, 185] predict phonon modes at energies 24.8 meV, 28.2 meV, 34.7 meV and 49.59 meV for  $2H - \text{TaS}_2$ . Given the agreement between this ARPES

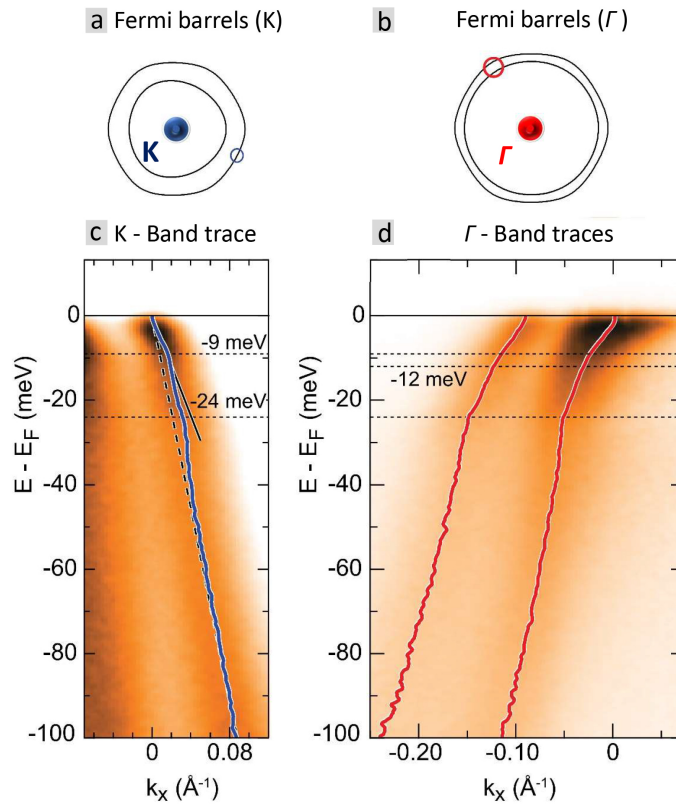


FIGURE 4.3: **Band renormalization signatures of  $2H - \text{NbSe}_2$** [37].

(a,b) Fermi surface schematics of  $2H - \text{NbSe}_2$ , showing both  $\Gamma$  and K centric Fermi barrel systems, respectively. (c) Experimental band dispersion trace, due to the band corresponding to the outer K-centric Fermi surface barrel, taken at the point indicated with blue circle on (a). Approximated bare band dispersion is shown as a black dashed line. (d) Band traces, due to the inner and outer  $\Gamma$ -barrels, taken at the point indicated with a red circle on (b). Locations of band renormalizations (i.e., the *kinks*) are marked with horizontal dashed lines. Band traces are superimposed on ARPES energy momentum intensity maps (EMIMs)

analysis and the phonon energies, band renormalizations identified above can be related to phonon modes coupling to the electronic band dispersion. This conclusion is in line with ARPES studies of 2H - NbSe<sub>2</sub> where, again, underlying collective modes were found to be phonons[37, 181]. Fig. 4.3 shows such renormalized bands obtained for 2H - NbSe<sub>2</sub> via a similar MDC analysis procedure[37]. In the case of 2H - TaSe<sub>2</sub>, comparable signatures of collective modes have been observed but yet to be identified[181, 182]. Beyond transition metal dichalcogenide materials, similar renormalizations due to collective modes including, but not limited to phonons have been reported for a variety of materials[175, 178–180] including high temperature superconductors [118, 158, 176, 177].

### 4.3.3 Renormalization Signatures in the Self-Energy

The behavior of real,  $\Sigma'(\bar{\omega})$  and imaginary,  $\Sigma''(\bar{\omega})$  parts of the self-energy due to above identified electronic band renormalizations can be characterized as well. Admitting to a method repeatedly used in the proceeding literature[37, 118, 158, 175–177, 180], bare electronic band dispersion( $\epsilon_{\mathbf{k}}$ ) was approximated as a straight line in a tight region of energy and momentum in the vicinity of the kinks.

In the light of the Fig. 4.2(b) (or the Fig. 4.4(a)), notice the following behaviors of both bare -and- renormalized electronic bands, in high and low energy limits.

- At higher electronic binding energies than kink energies, the bare dispersion (represented by a black dashed line), aligns with the experimentally observed renormalized dispersion (plotted as green circles). Observe this behavior at deep binding energy region ( $\bar{\omega} \sim -0.1$  eV) on any of the band diagram.

- At the Fermi level,  $\bar{\omega} = 0$  eV, both bare and renormalized dispersion curves pass through the Fermi momentum  $k_F$ . In other words, both band traces should share the same Fermi crossing, as discussed in the section 4.3.2 above.
- In the intermediate energy range between above two extremes, renormalized dispersion deviates from the bare dispersion, giving rise to signature kinks.

As elaborated in the section 4.2, the real part of the self-energy,  $\Sigma'(\mathbf{k}, \bar{\omega})$  can be found as the difference between experimentally observed (line of green circles) and approximated bare band (black dashed line) dispersions, using the equation 4.7. Accordingly, in the Fig. 4.4(b), the plot of filled red circles associated with the right (red) vertical axis shows the variation of  $\Sigma'(\mathbf{k}, \bar{\omega})$  vs energy,  $\bar{\omega}$ .

Also, the imaginary part of the self-energy,  $\Sigma''(\mathbf{k}, \bar{\omega})$  can be found via the equation 4.9 using fitted widths of MDC peaks,  $W(\bar{\omega})$ . These widths are plotted on the same Fig. 4.4(b) as open blue circles in association with the left (blue) vertical axis. Two kink locations are marked with two black horizontal arrows on the renormalized band diagram on the Fig. 4.4(a). These locations fall in excellent agreement with vertical black arrows on the Fig. 4.4(b) indicating,

- Clearly identifiable peaks on the real part of the self-energy ( $\Sigma'$  data), given in red filled circles.
- Locations of drastic slope changes of the width ( $W$  data), given as blue open circles on the same diagram.

Conclusively, the renormalizations identified via observing the bands in the section 4.3.2, are further confirmed via self-energy analysis, as expected[127].

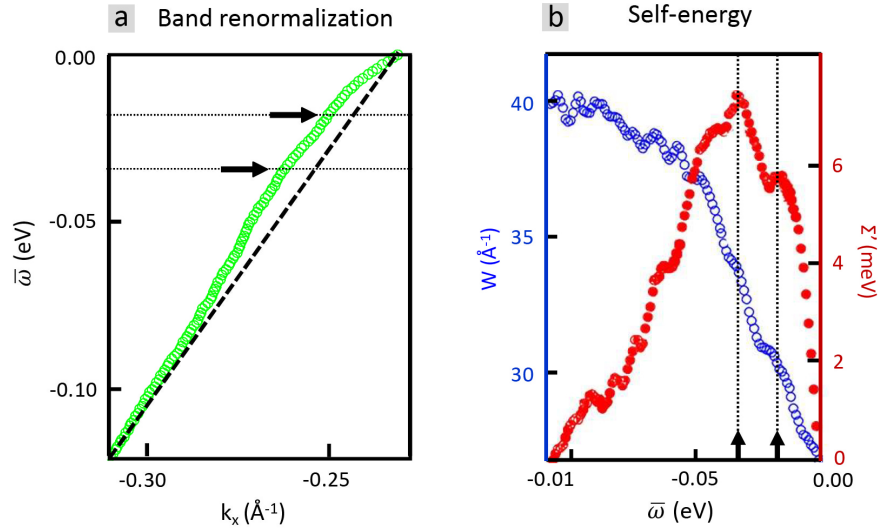


FIGURE 4.4: **Renormalization signatures in self-energy.**

(a) Experimental electronic band dispersion for the outer K-centric Fermi surface barrel of  $2H - \text{TaS}_2$ . Two reorganizations are identified with black horizontal arrows at energies  $\bar{\omega} \sim 18$  meV and  $\sim 35$  meV. (b) Self energy analysis of the band dispersion in (a). The real part of the self-energy,  $\Sigma'(\bar{\omega})$  is plotted as filled red circles and should be read with respect to the right axis (colored in red). Widths of MDC peaks ( $W(\bar{\omega})$ ) are given in open blue circles, with respect to the left axis (colored in blue). Note that the imaginary part of the self energy,  $\Sigma''(\bar{\omega})$  is directly proportional to  $W(\bar{\omega})$ . Prominent peak locations of the  $\Sigma'(\bar{\omega})$  coincide with significant changes in the slope of  $W(\bar{\omega})$  data, marked with black vertical arrows.

#### 4.3.4 Renormalizations Due to the Unidentified Collective Modes

Two prominent kinks at energies  $\bar{\omega} \sim 18$  meV and  $\sim 35$  meV identified above can easily be related to independently confirmed phonon modes as discussed in the section 4.3.2. Apart from these two, several other renormalization signatures are also significant on the experimental band trace as well as on both the real and imaginary plots of self-energy. As per examples, on the real component of the self-energy  $\Sigma'(\mathbf{k}, \bar{\omega})$  plot on the Fig. 4.4(b, red filled circles), observe the features in the energy range of  $-0.1$  eV  $< \bar{\omega} < -0.05$  eV. The cutoff energy for phonon modes in  $2H - \text{TaS}_2$  is 49.59 meV, as confirmed from both calculations and experimental observations [183, 184]. Therefore, any kink feature below this cutoff energy cannot be a consequence of phonon modes coupling to

the electronic structure.

The feature closer to -0.1 eV might be due to any imperfections of the method of data analysis, as the validity of the MDC based self-energy analysis procedure may fall apart for energies further from the chemical potential, as discussed in the section 4.2.2. On the other hand, the peak in the vicinity of -0.07 eV appears interesting. A signature of an unresolved collective mode at a similar energy has been reported for 2H - TaSe<sub>2</sub> as well[181, 182]. However, at this point, the origin of this feature is left as an open question and requires further examination.

## 4.4 Momentum and Temperature Dependence of the Band Renormalization

### 4.4.1 The Electron-Phonon Coupling Parameter, $\lambda(\mathbf{k})$

The parameter  $\lambda(\mathbf{k})$  is a measure of the electron-phonon coupling strength. It is also known as the ‘mass enhancement parameter’[37]. Assuming that the entire mass renormalization is due to electron-phonon interactions, the following relationship can be utilized to calculate  $\lambda(\mathbf{k})$  [37, 118, 158, 176]:

$$\lambda = \frac{v_F^0}{v_F^*} - 1 \quad (4.10)$$

where,  $v_F^0$  is the bare Fermi velocity which can be found as the slope of the bare band dispersion, and  $v_F^*$  is the renormalized Fermi velocity, which is the slope of the renormalized band dispersion, evaluated at the chemical potential,  $\bar{\omega} = 0$ .

#### 4.4.2 Momentum Dependence of the Band Renormalization

For 2H – TaS<sub>2</sub>, several representative dispersion plots were analyzed at the outer Fermi surface barrel about the K–point using the method outlined in above section 4.3.1. Locations of the respective Fermi crossings of each band are marked with green dots, numbered from 1 to 4 on the Fig. 4.5(a). Renormalized dispersions corresponding to these points are given in the Fig. 4.5(c) as plots of green circles. Similarly, Red dots from 5 to 10, marked on the inner  $\Gamma$ –centered Fermi surface barrel on Fig. 4.5(a) indicate momentum locations corresponding to dispersion plots traced with red circles in the Fig. 4.5(b).

All the dispersion traces depicted in both Fig. 4.5(b) and (c), in the neighborhoods of  $\Gamma$  and K high symmetry points, possess consistent multiple kink signatures discussed in sections 4.3.2 and 4.3.3. corresponding kink energies are positioned within the range of 10 meV to 40 meV, and kink locations align with expected phonon energies.

In order to determine the electron–phonon coupling,  $\lambda(\mathbf{k})$ , the following procedure was carried out for each trace.

- 1 The bare band was fitted with a black solid line at higher binding energies, and was forced to pass through the respective Fermi crossing. Slope of this line represented the bare Fermi velocity,  $v_F^0$ .
- 2 A black dotted line was fitted to the front side of the kink, which is closest to the chemical potential, and also was constrained to pass through the Fermi crossing. The slope of this fit gave the renormalized Fermi velocity,  $v_F^*$ .
- 3 Then, the  $\lambda(\mathbf{k})$  value for the dispersion trace was calculated using the equation 4.10.

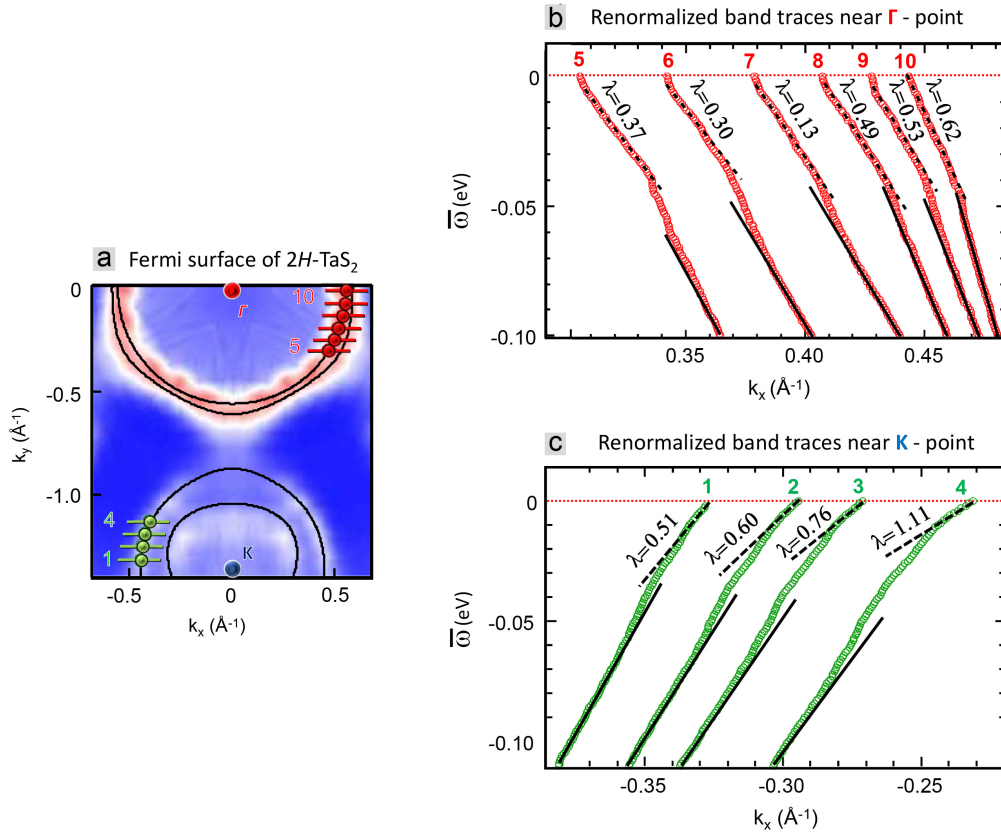


FIGURE 4.5: **Momentum dependence of the electron-phonon coupling in 2H–TaS<sub>2</sub>.**

(a) Fermi surface of 2H – TaS<sub>2</sub> with momentum cuts used in finding band dispersions shown in (b),(c) marked. Series of momentum density curves (MDC) for various energies were taken at each location along the momentum cuts indicated and then, peak locations of them were plotted to get respective electronic band dispersions. Momentum locations of the Fermi crossings for each dispersion is marked as a colored dot. (b) Band dispersions for the green cuts marked 1–4 on (a), corresponding to the outer K–centric Fermi surface barrel. (c) Band dispersions for the red cuts marked 5–10 on (a), corresponding to the inner  $\Gamma$ –centric Fermi surface barrel. The chemical potential is marked as a red dotted line. Corresponding value of the electron-phonon coupling parameter ( $\lambda$ ) is marked near each dispersion trace.

These  $\lambda(\mathbf{k})$  values are marked on the Fig. 4.5(b) and (c) accordingly. Variation of these values reveals a gentle momentum dependence in a range from 0.30 to 1.11[47]. Qualitatively similar observations have been reported for 2H – NbSe<sub>2</sub> as well[37, 186], and some results are shown in the Fig. 4.6.

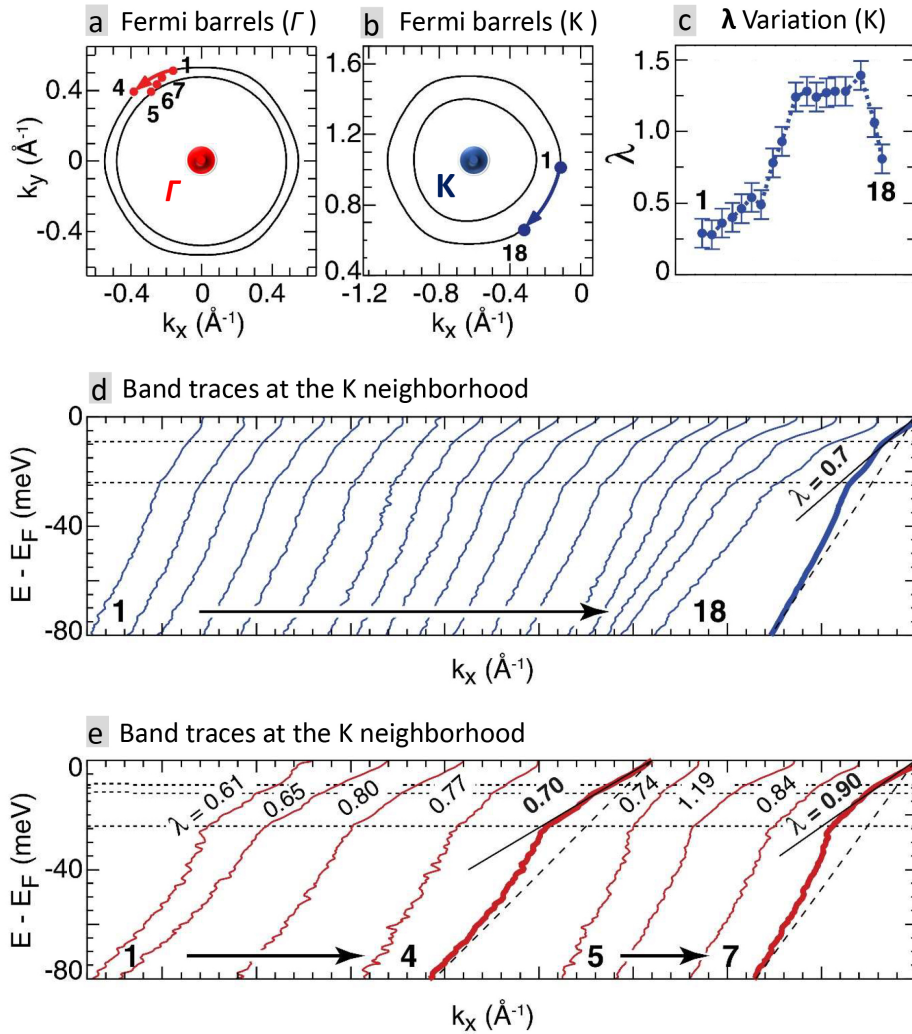


FIGURE 4.6: **Momentum dependence of the electron-phonon coupling in  $2H-NbSe_2$ .** [37]

(a,b) Fermi surface schematics of concentric barrels in  $2H - NbSe_2$ , in the  $\Gamma$  and K neighborhoods, respectively. Momentum locations of the Fermi crossings corresponding to band traces in (d) and (c) are marked and numbered. (c) Variation of the electron-phonon coupling parameter ( $\lambda$ ) for band traces 1 through 18, shown on (c). (d) Series of 18 band dispersions on the outer K-centered Fermi surface barrel. Corresponding momentum locations are marked on (b). Thick blue band with  $\lambda = 0.7$  is the averaged dispersion.  $\lambda$  values for individual traces are plotted on (c). (e) Series of band dispersions in the  $\Gamma$ - and K-neighborhoods, taken at the points indicated on (a). Points 1 to 4 lie on the outer  $\Gamma$ -Fermi surface barrel and averaged dispersion is shown as a thick trace. Traces 5 to 7 correspond to points on and within the barrels, and their average dispersion is shown as well. For each averaged dispersion curve shown as thick traces have the bare band approximation, indicated as a black dashed line. Black solid lines indicate fits done for the kinks in order to extract renormalized Fermi velocity.

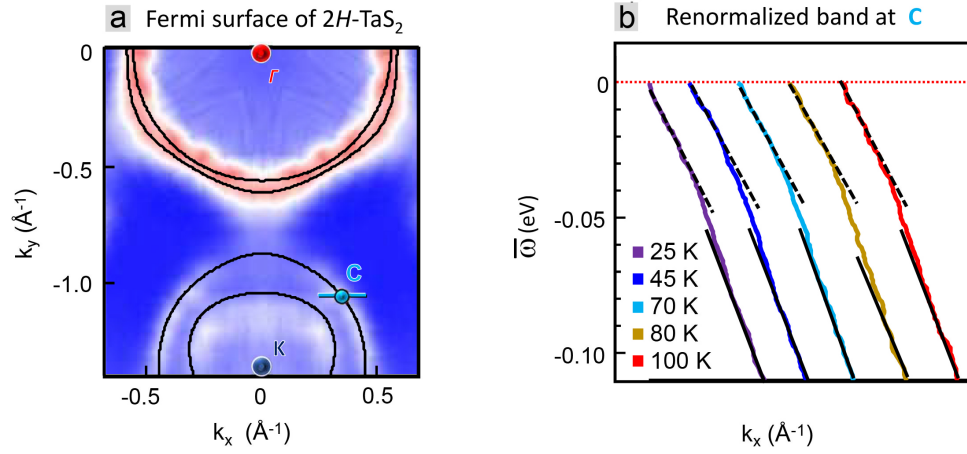


FIGURE 4.7: **Temperature dependence of the electron-phonon coupling.** (a) Fermi surface of  $2H - \text{TaS}_2$  with the momentum cuts used in finding band dispersions shown in (b) marked in light blue. Point **C** on the outer K-centered Fermi surface barrel indicate the momentum location of the Fermi crossing of the band traces. (b) Series of band dispersions on the cut marked on (a), taken at a range of temperatures. solid black lines are the fits to the bare band and dashed black lines are the fits done on the renormalization kink closed to the chemical potential. The chemical potential is marked as a red dotted line. Slopes and thus the electron-phonon coupling parameter  $\lambda$ , shows no significant temperature dependence.

In a future study, it would be interesting to explore whether this momentum-anisotropy of  $\lambda(\mathbf{k})$  results in any momentum-dependence of the CDW and/or the superconducting energy gap of  $2H - \text{TaS}_2$ .

#### 4.4.3 Temperature Dependence of the Band Renormalization

Finally, the Fig. 4.7(d) shows a series of band dispersions taken at the location ‘C’, marked with light blue on the outer K-barrel as indicated on the Fig. 4.7(a). These MDCs correspond to the range of temperatures from 25 K to 100 K which spans across the CDW transition temperature ( $T_{CDW}$ ) for  $2H - \text{TaS}_2$ . The observed temperature independent nature of the  $\lambda(\mathbf{k})$  also supports the idea of electron-phonon coupling being the responsible for electronic band renormalization in  $2H - \text{TaS}_2$ .

## 4.5 Summary

An elaborate analysis of the many-body renormalizations of electronic band dispersion in  $2H - \text{TaS}_2$  was conducted using ARPES. The observations were as follows:

- i Renormalizations of the electronic dispersion were observed throughout the momentum space.
- ii Many-body renormalizations were identified to be due to electron-phonon interactions.
- iii The electron-phonon coupling was slightly momentum dependent, and a similar momentum-anisotropy has been detected in the case of related compound, namely  $2H - \text{NbSe}_2$ .
- iv Temperature independence of the band-renormalizations corroborated the idea of electron-phonon interactions driving the many-body renormalizations.

In the proceeding chapter 3, it was concluded that the ‘Fermi surface nesting’ mechanism is unlikely to be the origin of the charge density wave transition in  $2H - \text{TaS}_2$ . Rather, based on the findings of this chapter, one could argue that the momentum anisotropy of the electron-phonon coupling in the system is important to stabilize the CDW wave vector. Given the similarity between  $2H - \text{TaS}_2$  and other related incommensurate CDW materials with 2H poltypes, such as  $2H - \text{NbSe}_2$  and  $2H - \text{TaSe}_2$ , it is likely that the relevance of the momentum anisotropy of the electron-phonon coupling to the CDW instability is generic to all these materials.

---

## Chapter 5

# Thermoelectric Performance of Lead Chalcogenides

### 5.1 Background

The figure of merit,  $ZT$  of a thermoelectric material is intimately related to its electronic structure. Therefore the understanding of the temperature dependence of the electronic structure is crucial in predicting and fine-tuning the performance of a thermoelectric material. Being able to simultaneously measure both energy and momentum of the occupied electronic states in a solid, temperature dependent ARPES is a well-suited probe for this task [69].

#### 5.1.1 The Band Structure of PbQ

The valence band structure of Lead chalcogenides (PbQ, where Q stands for S, Se, or Te) consists of two hole bands, known as upper valence band (UVB) and lower valence band (LVB). Maximum of the UVB occurs at the L symmetry point (see the Fig. 1.6 for the Brillouin zone diagram of PbQ). Moreover, the UVB has extended electronic states,

presumably due to a flat secondary valence band, which is the LVB. This lower valence band lies along  $\Gamma$ -K line, with its maximum at lower energies compared to that of the UVB [187–189]. Even though some elaborate investigations have been done on Lead chalcogenides, the exact mechanism behind their high thermoelectric efficiency is yet unresolved. In particular, the connection between temperature dependent thermopower and the temperature evolution of the electronic structure is in controversy.

In a number of reports[77, 78, 188, 190–192], the temperature dependence of the thermopower of PbQ has been interpreted in terms of a relative shift between upper and lower valence bands. In particular, the enhancement of thermopower in PbTe and PbSe at elevated temperatures has been attributed to the dominant contribution from the highly degenerate LVBs, associated with a greater effective mass than that of the UVBs. This shift leads to the eventual crossover of bands, upon the increase of temperature. So far, this band convergence has been predominantly inferred indirectly from Hall experiments, where the Hall coefficient exhibits a maximum at the convergence, with no direct experimental evidence for such a temperature dependent change in valence band structure.

Even though the salient features of the findings in these studies are similar, there is a marked disagreement among the reported values for the crossover temperatures. For example, early studies dating back to the 1960's along with some recent work predicted a crossover temperature  $\sim 450\text{K}$  in PbTe. This extrapolation prevailed in the literature until it was shown to happen at much higher temperatures ( $\sim 750\text{K}$ ), via very recent results from magnetic field dependent Hall coefficient measurements at elevated temperatures [190, 191]. More importantly, there are no direct experimental observations for temperature dependent evolution of valence bands. Furthermore, recent reports based

on first-principle calculations cast serious doubts on the very notion of this two-band analysis of thermopower data [193, 194] and thus, the models based on temperature dependent valence band shift. This void invites for an in-depth examination of the temperature evolution of electronic structures of Lead chalcogenides using ARPES.

It should be noted that there are several important ARPES studies conducted on both PbTe and PbSe [82–84, 195, 196]. However, their emphasis has been on entirely different aspects of the electronic structure. Via temperature dependent ARPES measurements on PbQ, we attempt to resolve the following lingering issues in the field:

- What is the valence band structure of these materials?
- How does the rising temperature impact their valence bands?

### 5.1.2 Samples

Temperature dependent ARPES experiments were carried out on several *n*- and *p*-doped single crystal Lead chalcogenide samples. They are labeled as follows.

- two *n*-type PbS (referred to as PbS-#1, PbS-#2)
- two *n*-type PbSe samples (referred to as PbSe-#1, PbSe-#2)
- one *n*- and, two *p*- type PbTe samples (referred to as PbTe-#1, PbTe-#2)

PbQ samples were prepared by melting mixtures of Pb and Q (S, Se, and Te) at 100K to 150K above individual melting points of PbQ inside evacuated fused silica tubes. PbI<sub>2</sub> was used for achieving *n*-type doping and Na was used for *p*-type doping. Typical carrier concentrations of *n*- and *p*- type samples ranged from  $2 \times 10^{19} \text{ cm}^{-3}$  to  $5 \times 10^{19} \text{ cm}^{-3}$  and

$0.2 \times 10^{19} \text{ cm}^{-3}$  to  $2 \times 10^{19} \text{ cm}^{-3}$ , respectively. These samples were then cleaved *in situ* to expose fresh surface (001) of the crystal for ARPES measurements.

## 5.2 Hole Pockets in the Momentum Space

Momentum space geometry of a generic Lead chalcogenide is explained in the section 1.2.2. Since all samples were preferentially cleaved along the (001) crystallographic plane, the projection of the Brillouin zone onto the (001) plane, as shown in the Fig. 5.1(a), will be practically useful. This diagram will serve as a momentum space map for the interpretation of subsequent data. Note that the  $\Gamma$  and L symmetry points in the bulk Brillouin zone are projected on to the  $(\bar{\Gamma})$  and  $(\bar{X})$  points on the surface Brillouin zone.

### 5.2.1 Analysis of Constant Energy Intensity Maps

Shown in Fig. 5.1(b – g) are some constant energy intensity maps (CEIMs). CEIMs are, ARPES data as a function of in-plane momentum components  $k_x$  and  $k_y$  at fixed  $\bar{\omega}$ , where  $\bar{\omega}$  stands for the electronic energy with respect to the chemical potential. The method of constructing the CEIMs, starting from the raw ARPES data is as follows.

1. The constant signal at  $\bar{\omega} > 0$ , which occurs due to the second order light, was subtracted from the raw data.
2. Each ARPES spectrum was normalized by the area enclosed by itself and the energy axis, between measured values of  $\bar{\omega}$ .

3. The raw data captured more than 50% of the surface Brillouin zone for each sample. For a better visualization, the CEIMs for the entire Brillouin zone were reconstructed by reflections, using interpolations to uniform grids.
4. Alternate normalization procedures have also been tried but, no qualitative differences either in the structure or the evolution of these intensity maps were found.

### 5.2.2 High and Low Energy Hole Pockets

For each doped PbQ sample, CEIMs at lower energies (i.e., near the chemical potential) and higher energies (i.e., at deeper binding energies) were taken. Fig. 5.1(b) and (e) correspond to the CEIMs at  $\bar{\omega} = -0.04$  eV and  $-0.2$  eV, respectively for a *p*-type PbTe sample (PbTe-#1). In the lower energy CEIM given in the Fig. 5.1(b), the hole pockets derived from the upper valence band centered at *L* points are clearly visible around  $\bar{X}$ . The topology of CEIMs at higher energies change noticeably via the appearance of tubular regions connecting these isolated pockets as seen in the Fig. 5.1(e). This happens due to the contribution from the electronic states of the secondary valence bands (LVBs) lying deeper in binding energies.

Qualitatively similar evolution of the CEIMs with  $\bar{\omega}$  can be seen in the case of *n*-type PbSe in Fig. 5.1(c) and (f), and for *n*-type PbS in Fig. 5.1(d) and (g), as well. Appearance of these tubular regions in CEIMs at higher  $\bar{\omega}$  has been predicted in several band structure calculations [194, 197, 198] and they have also been observed in recent ARPES experiments on related material like  $\text{Pb}_{1-x}\text{Sn}_x\text{Te}$  [82] and SnTe [199].

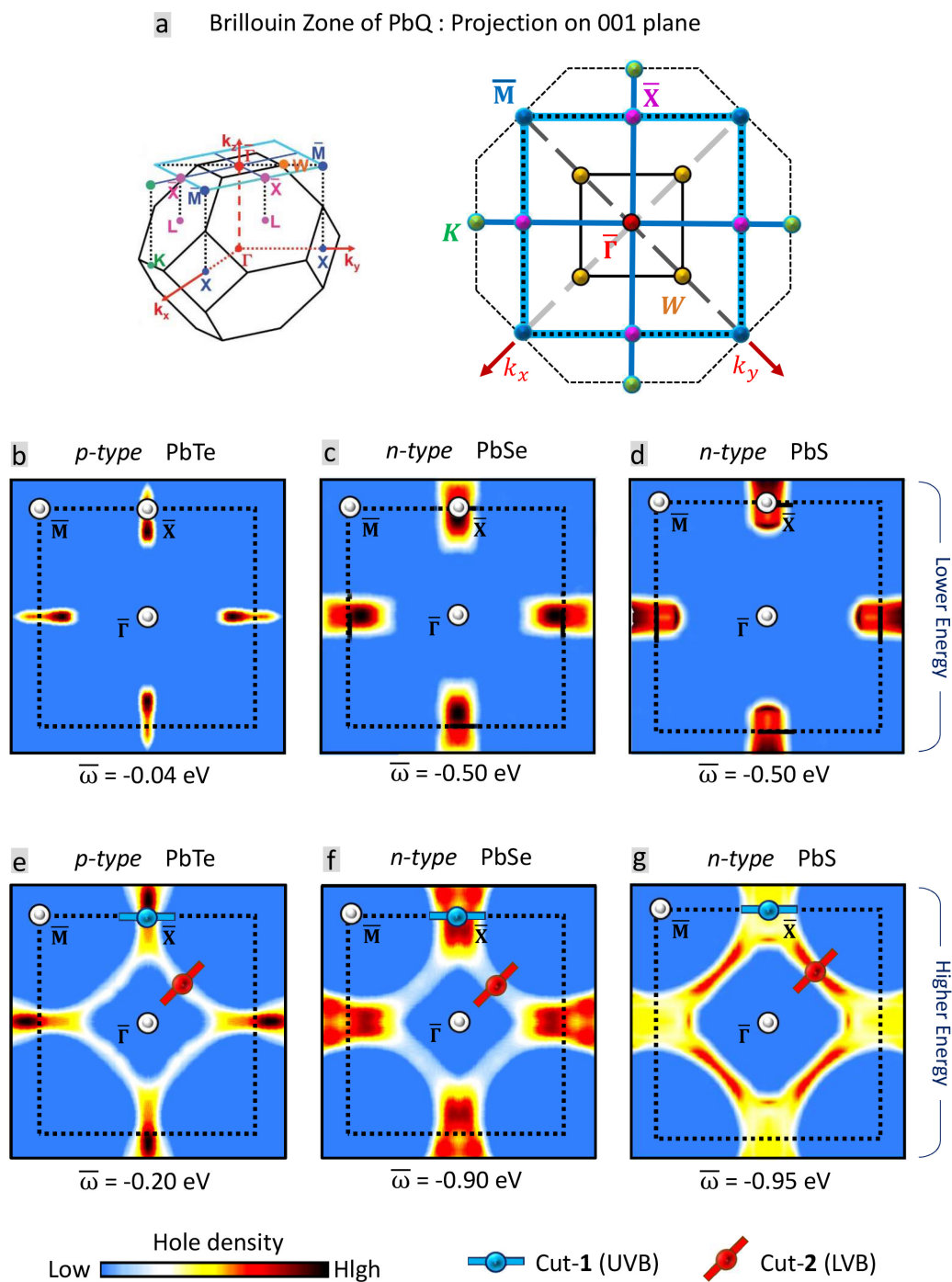


FIGURE 5.1: Low and high energy hole pockets of doped PbTe, PbSe and PbS.

Please see the next page for the details.

**Low and high energy hole pockets of doped PbTe, PbSe and PbS.**

Continued from the previous page ...

(a) The bulk Brillouin zone of a Lead chalcogenide and its projection on to (001) crystallographic plane (light blue square). High symmetry points and their projections are as marked;  $\Gamma$ , L and X points in the bulk Brillouin zone are projected to  $\bar{\Gamma}$ ,  $\bar{X}$  and  $\bar{M}$  points on the surface Brillouin zone. Black dotted square is the momentum space reference for subsequent CEIMs (constant energy intensity maps). (b, c, d) Lower energy CEIMs, taken closer to the Fermi energy level near the top of upper valence bands (UVBs). Hole pockets near  $\bar{X}$  points, on  $\bar{\Gamma} - \bar{X}$  lines are due to the UVBs projected from the vicinity of the L symmetry point on the line  $\Gamma - K$  in the bulk Brillouin zone. (e, f, g) Higher energy CEIMs, taken at deeper binding energies. Hole pockets form UVBs grow and get connected via tubular regions due to the lower valence bands (LVBs). Comparable features in  $n$ - type samples (c),(d),(f) and (g) lie deep in energy than  $p$ - type samples (b) and (e). On (e),(f) and (g) higher energy CEIMS, Momentum cuts indicated in light blue (Cut-1) and red (Cut-2) are marked for further analysis of UVBs and LVBs accordingly. Blue and red dots on these cuts correspond to the momentum locations of the top of the UVBs and LVBs respectively.

---

Another observation is, the CEIMs depicting comparable features, have more negative energies for  $n$ -type samples than in the  $p$ -type sample. This means both the upper and lower valence bands of  $n$ -type samples (Fig. 5.1(c), (d), (f) and g)) lie deeper in energy compared to the valence bands of the  $p$ -type sample (Fig.5.1(b) and (e)), as expected by the relevant doping.

### 5.3 Energy- Momentum Dispersion

For each PbQ sample, two momentum cuts are marked on Fig. 5.1(e), (f), and (g). Cut-1, marked in light blue are selected to capture the upper valence bands (UVBs), and light blue dots on these figures indicate the position of the maxima of each UVB. Cut-2, chosen to capture the lower valence bands (LVBs) are indicated in red, with red dots denoting the maxima locations of the LVBs. Energy momentum intensity plots along these cuts can be used to determine band edges, as explained below.

Note: Energy momentum intensity maps (EMIMs) are plots of intensity as a function of energy ( $\bar{\omega}$ ) and a selected momentum component, while other momentum components are held fixed. Selected momentum components for UVBs and LVBs are denoted as  $k_1$  and  $k_2$ , respectively in subsequent figures. Precise definitions of these variables  $k_1$  and  $k_2$  will be given in the section 5.3.3.

### 5.3.1 Resolution of the Band Edges

1. A momentum cut was determined on an energy iso-surface (CEIM) ‘blueprint’ in order to analyze desired features. Consider the  $n$ -type PbS sample, measured at 125K as an example. In this case, CEIM in the Fig. 5.1(g) was used as a blueprint to mark cut-1 and cut-2 to probe UVBs and LVBs, respectively.
2. EMIMs were taken along these cuts. Fig. 5.2(a) and (e) show EMIMs for Cut-1 (UVB) and Cut-2 (LVB), respectively. Note that the EMIM in the Fig. 5.2(a) has captured both UVB and the bottom of the conduction band (CB) as well.
3. Vertical cuts were taken for a series of momentum values on each EMIM. These cuts are energy distribution curves (EDCs), which are the line graphs of intensity vs. energy,  $\bar{\omega}$  for a fixed value of momentum. An EDC taken at the green dashed line on the Fig. 5.2(a) is shown in solid green on the Fig. 5.2(c). Corresponding momentum location, which marks the UVB maxima (and also the CB minima) will be referred to as  $\mathbf{k}_U$  in the following discussion.

Another EDC, taken along the pink dashed line on the Fig. 5.2(d) is shown in solid pink on the Fig. 5.2(f). This momentum location which marks the momentum at which the LVB maxima occur, will be labeled as  $\mathbf{k}_L$ .

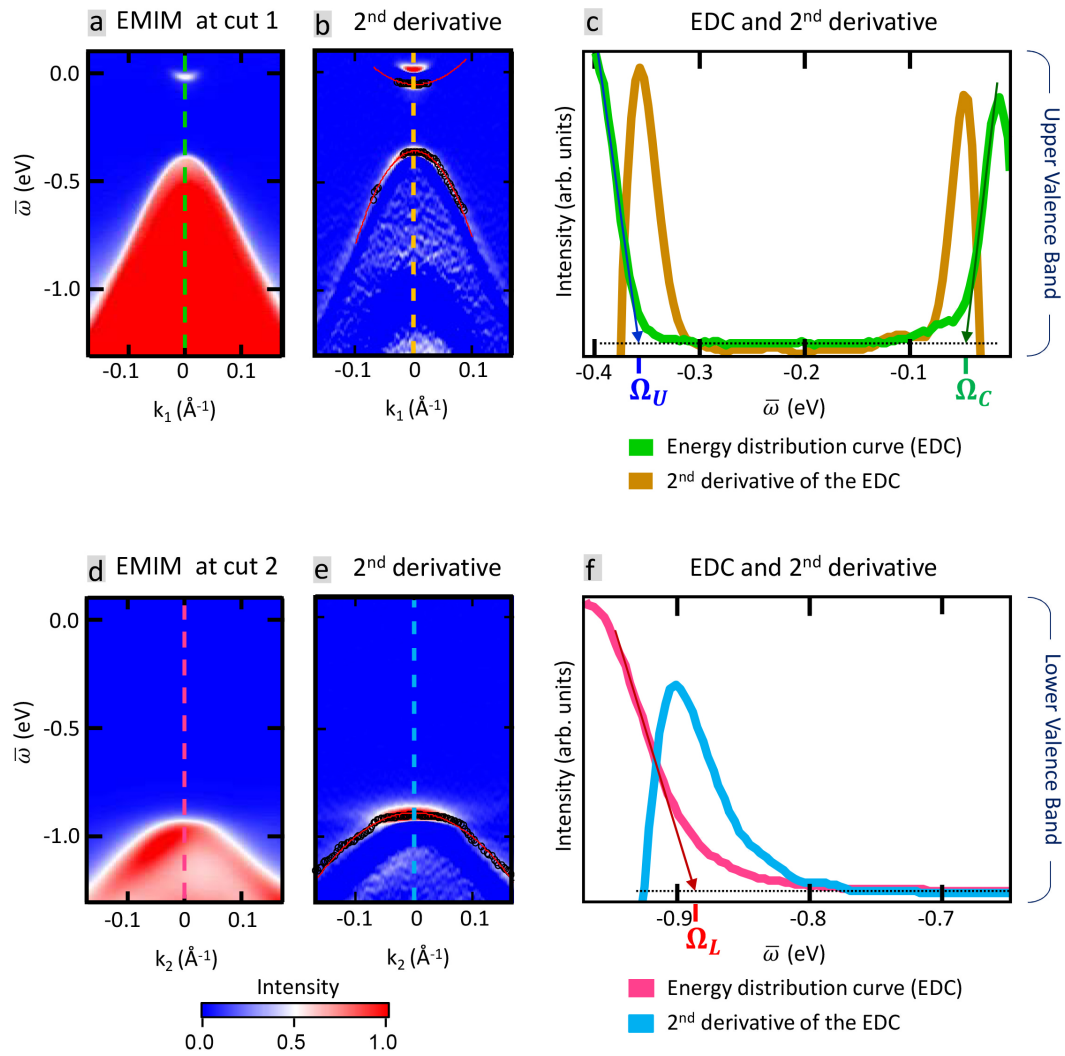


FIGURE 5.2: 2<sup>nd</sup> derivative analysis of band edges. Please see the next page for the details.

**2<sup>nd</sup> derivative analysis of band edges.**

Continued from the previous page ...

An  $n$ -type PbS sample, analyzed at 125K is used. **(a)** The energy momentum intensity map (EMIM) taken at the cut-1 marked on Fig.5.1(d). This EMIM captures the upper valence band (UVB) edge as well as the conduction band edge near the Fermi level. **(b)** 2<sup>nd</sup> derivative of the EMIM shown on (a), with respect to energy ( $\bar{\omega}$ ). Black circles indicate band edges determined by individual energy distribution curves (EDCs) while the red curve is the fitted band across black circles. **(c)** EDC taken at the green dashed line on (a) is plotted in solid green. 2<sup>nd</sup> derivative of this EDC (w.r.t  $\bar{\omega}$ ), which is the line profile indicated as an orange dotted line on (b) is plotted in solid orange. Edge of the UVB and the conduction band (CB) are denoted as  $\Omega_U$  and  $\Omega_C$  respectively. These edges can be identified on EDCs by extrapolations of the slopes (blue and green arrows) -or- as peaks of the EDC 2<sup>nd</sup> derivative, which are in agreement. Location of this EDC (green dashed line on (a)) and its derivative (orange dashed line on (b)) corresponds to momentum position  $k_U$ . **(d)** The EMIM taken at the cut-2 marked on Fig.5.1(g). This EMIM captures the lower valence band (LVB) edge. **(e)** 2<sup>nd</sup> energy derivative of the EMIM shown on (d), Black circles denote band edges from individual EDCS and the fit to the LVB is given in Red. **(f)** EDC taken at the pink dashed line on (d) is plotted in solid pink. 2<sup>nd</sup> energy derivative of this EDC or the line profile indicated as a light blue dotted line on (e) is plotted in light blue. Edge of the LVB, denoted as  $\Omega_L$ , can be consistently identified by EDC slope extrapolation (red arrow) or as the peak of the 2<sup>nd</sup> energy derivative if EDC. Location of this EDC (pink dashed line on (d)) and its derivative (light blue dashed line on (e)) corresponds to momentum position marked by  $k_L$ .

---

4. These EDCs have abrupt slope changes which can be pinpointed by, first, fitting tangents to regions of different slopes on the EDC, then extrapolating those fitted lines, and finally finding their intersecting points. Such constructions for upper valence band and conduction band edges have been performed on the Fig. 5.2(c) and are shown in blue and green arrows, respectively. Energy corresponding to UVB maximum is denoted as  $\Omega_U$ , while  $\Omega_C$  is the CB minimum. Similarly, using the pink EDC on the Fig. 5.2(f), the LVB maximum was found and denoted by  $\Omega_L$ .
5. As an alternative method, The second derivative of EDCs with respect to energy,  $\bar{\omega}$  were also used to find band edges where distinct peaks were observed at band edges. In both Fig. 5.2(c) and (f), such EDC derivative plots are shown with

peaks which correspond to the band edges. Energy locations for band edges ( $\Omega_U$ ,  $\Omega_C$  and  $\Omega_L$ ), found by means of both methods (EDC slope changes -and- peaks on EDC  $2^{nd}$  energy derivatives) are in very good agreement, as seen in the Fig. 5.2.

6. By taking the  $2^{nd}$  energy derivative of the entire EMIM in the Fig. 5.2(a), a ‘ $2^{nd}$  derivative intensity plot’ was created as given in the Fig. 5.2(b). This graphically shows band edges as ‘ridges’ for both UVB and CB. Similar  $2^{nd}$  derivative intensity plot for the EMIM in the Fig. 5.2(d) is given in the Fig. 5.2(e), with clearly identifiable LVB band edge signatures.
7. This edge resolving procedure was repeated for a series of other EDCs taken at different momentum locations near band maxima/minima. Resolved band edges (energy locations vs. EDC momenta) for each EDC were plotted as black circles on  $2^{nd}$  derivative intensity plots in Fig. 5.2(b) and (e).
8. Parabolic curves were fitted for band edge locations found via above EDC analysis. These curves, indicated in red on Fig. 5.2(b) and (e) are the reconstructed bands.
9. These parabolic band fits were used for further analysis like finding the effective particle mass, using the curvature and will be discussed separately in the section 5.3.4.

### 5.3.2 Band Edges of PbQ

EDCs and relevant EDC  $2^{nd}$  energy derivatives for three samples:  $p$ -type PbTe at 100 K,  $n$ -type PbSe at 100 K and  $n$ -type PbS at 125 K are shown in the Fig. 5.3. EDCs and their derivatives, taken along the momentum  $\mathbf{k}_U$  are depicted in Fig. 5.3(a), (b) and (c), respectively as light green and orange traces. On these figures, a solid blue line is fitted

to the forward slope of the upper valence band on each EDC. The extrapolated slopes of these EDCs and the related peaks on  $2^{nd}$  derivative traces were used to determine the energy position of UVB maxima,  $\Omega_U$  which are denoted by blue vertical dashed lines.

To find the energy position of the CB minima,  $\Omega_C$ , corresponding backward slopes were extrapolated as indicated in green solid lines. Using these extrapolations and the peaks in  $2^{nd}$  derivative traces,  $\Omega_C$  locations were found and are marked with green vertical dashed lines on Fig. 5.3(b) and (c). Additionally, in  $n$ -type samples, the topmost filled level of each conduction band were also observed. Purple solid lines indicate fits associated with the forward slopes of EDCs. Such extrapolated fits and relevant peaks on  $2^{nd}$  derivatives were used to locate associated energy values ( $\Omega'_C$ ), marked with purple vertical dashed lines. Note that, for the  $p$ -type PbTe sample, conduction band signatures were not detected. The reason for this is because, the  $p$ -doping has shifted the band structure up in energy, and as a result, more energetic CB states were not occupied at the measured sample temperature of 100 K. ARPES can only detect occupied electronic states.

Similarly, on Fig.5.3(d), (e) and (f), pink traces are the EDCs taken along the momentum  $\mathbf{k}_L$ , and respective  $2^{nd}$  derivatives are shown in light blue. In order to find the energy position corresponding to maxima of the lower valence bands( $\Omega_L$ ) extrapolated fits on forward LVB slopes were used as indicated with red solid lines. These, along with peaks in the  $2^{nd}$  derivatives were used to locate  $\Omega_L$ . These energies are marked as red vertical dashed lines on Fig. 5.3(d), (e) and (f).



### 5.3.3 Reconstructed Band Dispersions of PbQ

To further investigate the band structure of Lead chalcogenides, EMIMs, taken along the momentum cut-1 and cut-2, indicated on the Fig. 5.1(e), (f), and (g) were used. Cut-1 captured the upper valence band (UVB), and a momentum variable  $k_1$  was defined with respect to the UVB maxima (i.e.,  $\mathbf{k}_U$ ). As seen on the Fig. 5.1, this cut is parallel to the  $k_x$ , or in other words, perpendicular to the  $\bar{\Gamma} - \bar{X}$  line on the Brillouin zone as marked on the Fig. 5.1(a).

$$k_1 = k_x - (\mathbf{k}_U)_x \quad (5.1)$$

Here, the  $k_1$  is the relative momentum variable used for the horizontal axis on subsequent figures (Fig. 5.4 and Fig. 5.5) wherever the UVBs are involved. The  $k_x$  is the absolute  $x$ -momentum component in the Brillouin zone. The parameter  $(\mathbf{k}_U)_x$  represents the  $x$ -component of the momentum coordinate of  $\mathbf{k}_U$ , which is the location of the UVB maxima (and also the CB minima). Similarly, another momentum variable  $k_2$  was defined relative to the LVB maxima (i.e.,  $\mathbf{k}_L$ ). As in Fig. 5.1, the unit vector along this cut was defined as  $\hat{\mathbf{e}}$ , and  $k_2$  was measured along this  $\hat{\mathbf{e}}$  direction.

$$k_2 = \mathbf{k} \cdot \hat{\mathbf{e}} - \mathbf{k}_L \cdot \hat{\mathbf{e}} \quad (5.2)$$

This  $k_2$  was used as the relative momentum variable for the horizontal axis on subsequent figures whenever an LVB is depicted. The  $\mathbf{k}$  is a general momentum variable with respect to the Brillouin zone and  $\mathbf{k}_L$  represents the absolute momentum coordinate of the LVB maxima.

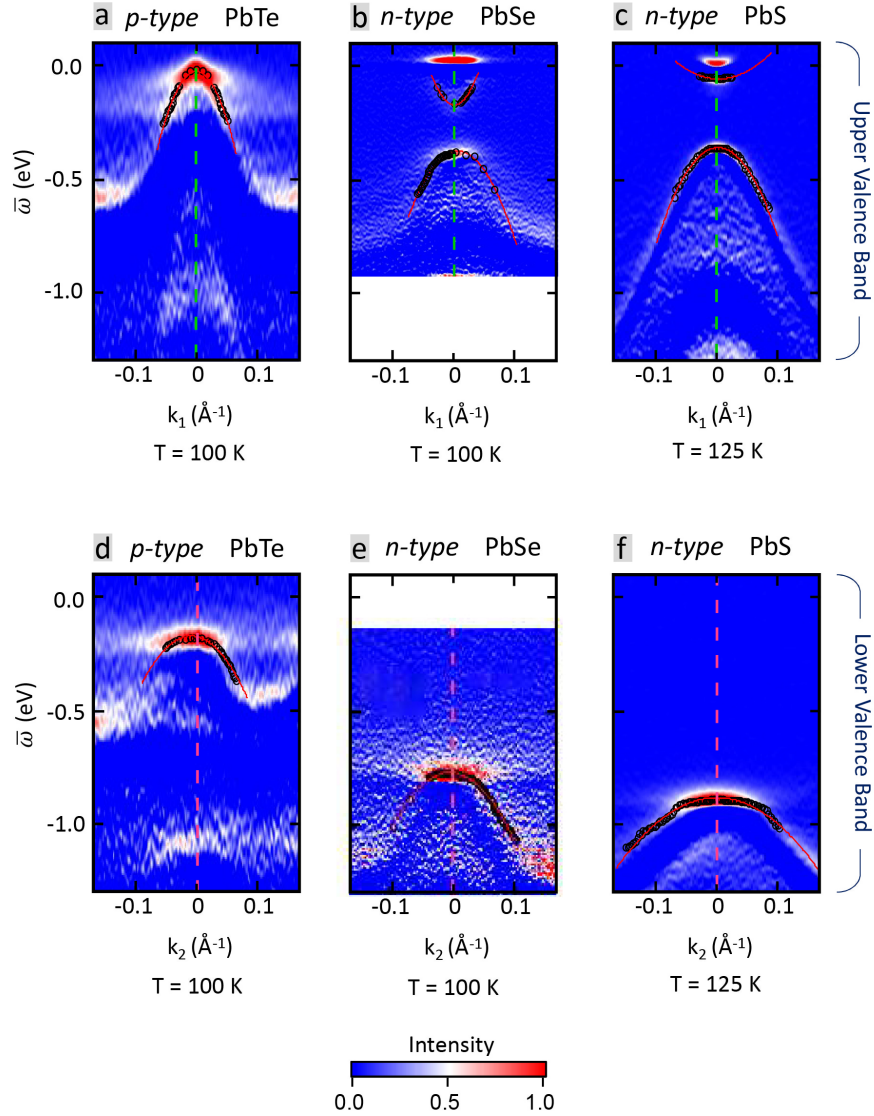


FIGURE 5.4: **2<sup>nd</sup> derivatives of energy momentum intensity maps.**

(a, b, c) 2<sup>nd</sup> derivatives with respect to energy,  $\bar{\omega}$  for energy momentum intensity maps (EMIMs) taken at momentum cut-1 as marked on Fig. 5.1(e), (f), and (g). These depict the upper valence band (UVB) near its maxima. On (b) and (c), conduction band (CB), near its minima is also shown. Light green dashed lines indicate the momentum location  $\mathbf{k}_U$ , corresponding to UVB maxima and CB minima. (d, e, f) 2<sup>nd</sup> energy derivatives of EMIMs taken at momentum cut-2, marked on Fig. 5.1(e), (f), and (g). These depict the lower valence band (LVB) near its maxima. Pink dashed lines mark the momentum location  $\mathbf{k}_L$ , corresponding to LVB maxima. Energy values of the vertical axis,  $\bar{\omega}$ , are given with respect to the chemical potential and, horizontal (momentum) axis values  $k_1$  (for UVBs) and  $k_2$  (for LVBs) are shown the momenta relative to the respective band maxima, as defined in the section 5.3.3. On all the figures, black circles denote band edges found with EDC analysis, and red curves are the parabolic fits to these band edge locations.

The EMIMs capturing lower and upper valence band maxima are shown in the Fig. 5.5. The 2<sup>nd</sup> derivatives of these EMIMs for the three samples in the discussion so far, (i.e., derivatives of Fig. 5.5(a)-through-(f)), are shown in the Fig. 5.4. On these diagrams, band dispersions,  $\bar{\omega}(k)$  extracted for individual momentum,  $k$ , are superimposed as black open circles. These locations can be visualized as band edges found on individual energy distribution curves for each momentum,  $k$ , as discussed in the section 5.3.2. Red solid curves shown are the parabolic fits to these dispersions.

The Fig. 5.5 shows EMIMs of UVBs (on the left), and EMIMs for LVBs (on the right), for all three samples discussed so far:  $p$ -type PbTe,  $n$ -type PbSe, and  $n$ -type PbS. Additionally, EMIM data for another  $n$ -type PbTe sample is also shown in Fig. 5.5(g) and (h). Alongside these EMIMs, band dispersions (marked in open circles) and parabolic fits to those dispersions (solid curves) are shown for the first three samples. Fig. 5.5(a), (c), (e), and (g) clearly show how the upper hole valence band dispersion behaves. Also, an electron band, separated in energy and momentum from this hole band is observed as in Fig. 5.5(c), (e), and (g). This is the conduction band (CB). The minima of the CB lies directly above the UVB, along the green dashed line denoting the momentum  $\mathbf{k}_U$ , thus opening a direct band gap. (This CB is not detectable on  $p$ -type samples as it is unoccupied at the probed temperature, as discussed above.)

Furthermore, in Fig. 5.5(b), (d), (f), and (h), another hole band is detected along cut-2, centered at a different location in the momentum space. This band was identified as the so-called ‘lower valence band’ which was so far undetected. The LVB maximum is located at the momentum  $\mathbf{k}_L$ , which lies away from the  $\bar{\Gamma} - \bar{X}$  (i.e., away in momentum from the UVB maximum and CB minimum).

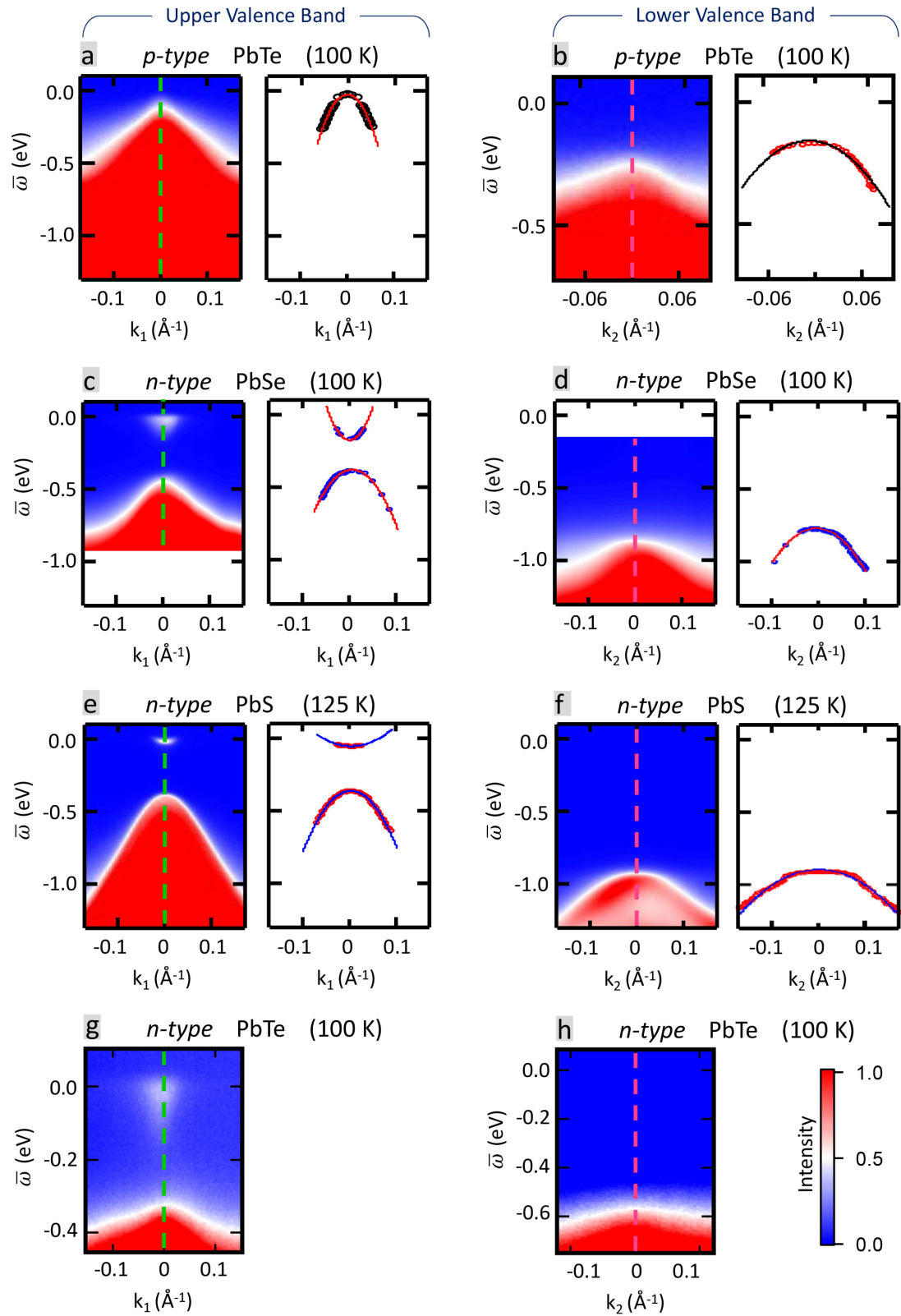


FIGURE 5.5: Energy momentum intensity maps, and upper and lower band dispersions of PbQ.

Please see the next page for the details.

### Energy momentum intensity maps, and upper and lower band dispersors of PbQ.

Continued from the previous page ...

Energy momentum intensity maps (EMIMs), and fitted band dispersors for upper valence bands (UVBs) are shown on left, and similar EMIMs and dispersors for upper valence bands (UVBs) are given on the right. **(a)** EMIM along the cut-1 on the Fig.5.1(e) and the fitted UVB dispersor for *p*-type PbTe at 100K. **(b)** EMIM along the cut-2 on the Fig.5.1(e) and the fitted LVB dispersor for *p*-type PbTe at 100K. **(c, d)** EMIMs along the cut-1 and cut-2 on the Fig.5.1(f) and the fitted conduction band (CB) UVB and LVB dispersors, respectively for *n*-type PbSe at 100K. **(e, f)** EMIMs along the cut-1 and cut-2 on the Fig.5.1(g) and the fitted band dispersors of CB, UVB and LVB, respectively for *n*-type PbS at 125K. **(g, h)** EMIMs capturing UVB and LVB of a *n*-type PbTe sample at 100K. Vertical axis energy values,  $\bar{\omega}$ , are given with respect to the chemical potential and, horizontal (momentum) axis values  $k_1$  (for UVBs) and  $k_2$  (for LVBs) are shown as relative momenta, as defined in the section 5.3.3. Band dispersors are shown by open circles and parabolic fittings of the dispersors are shown by solid curves. On the EMIMs capturing UVBs and CBs (shown on the left), the vertical green dashed lines corresponds to the momentum  $k_U$  where as, on the EMIMs capturing LVBs (shown on the right), the vertical pink dashed lines corresponds to the momentum  $k_L$ .

---

It is useful to point out that, several high symmetry lines from the three-dimensional Brillouin zone, including  $\Gamma$ -X,  $\Gamma$ -K, K-W and W-X get projected onto the  $\Gamma$ -M in the (001) surface Brillouin zone. Because of this overlap, association of this second valence band to a specific bulk electronic state would require a detailed study of the electronic structure in three-dimension, beyond the scope of this ARPES study.

Nevertheless, the discussion so far, together with the Fig. 5.5, leads to a clear visualization of the two-band picture of the valence band structure of Lead chalcogenides.

#### 5.3.4 Effective Masses

Effective particle masses corresponding to each band can be approximated using parabolic fitting of dispersion curves in the vicinity of its band maximum. Table 5.1 lists such effective masses,  $m^*$ , as fractions of the bare electron mass,  $m_e$ , for PbTe, PbSe and PbS.

These values consistently show that the holes in the lower valence bands are heavier than

TABLE 5.1: Values of effective mass of the UVB ( $m_{UVB}^*$ ), and that of the LVB ( $m_{LVB}^*$ ) in units of electronic mass  $m_e$ 

Material	$\frac{m_{UVB}^*}{m_e}$	$\frac{m_{LVB}^*}{m_e}$
PbTe	0.045	0.121
PbSe	0.087	0.141
PbS	0.093	0.349

the holes of the upper valence bands in Lead chalcogenides. This can be qualitatively inferred by visual comparisons of EMIMs corresponding to upper and lower valence bands in Fig.5.4 (top row vs bottom row) or 5.5 (left column vs right column) as well.

### 5.3.5 Identification of the Band Gaps

A generalized two-dimensional sketch of the above inferred band structure is presented in the Fig. 5.6. Maximum of the upper valence band and the minimum of the conduction band occur at the momentum location  $\mathbf{k}_U$ . According to the Fig. 5.1(a), this position lies on the  $\bar{\Gamma}-\bar{X}$ , in close proximity to the point  $\bar{X}$ , which is the projection of the L point from the bulk Brillouin zone. The energy gap between the conduction band minimum,  $\Omega_C$ , and the upper valence band maximum,  $\Omega_U$ , is denoted as  $\Delta_U$ . This is a direct band gap (at  $\mathbf{k}_U$ ).

$$\Delta_U = \Omega_C - \Omega_U \quad (5.3)$$

Maximum of the lower valence band occurs at a different momentum location,  $\mathbf{k}_L$ . The energy gap between the conduction band minimum,  $\Omega_C$ , and the upper valence band

maximum,  $\Omega_U$ , is denoted as  $\Delta_L$ . Since these points are located at different momenta,  $\mathbf{k}_U$  and  $\mathbf{k}_L$ , respectively,  $\Delta_L$  is an indirect band gap.

$$\Delta_L = \Omega_C - \Omega_L \quad (5.4)$$

The energy separation between upper and lower valence bands would then be,

$$\Delta = \Delta_L - \Delta_U \quad (5.5)$$

In cases where the conduction band is not detected, (e.g., as in *p*-type samples) the following equation is applicable.

$$\Delta = \Omega_U - \Omega_L \quad (5.6)$$

### 5.3.6 Variation of the Band Gap Among PbQ

The table 5.2 contains  $\Delta_U$  and  $\Delta_L$  for various *n*-type PbQ samples for temperatures  $\sim 100$  K. Data for the PbSe sample listed here are shown in Fig. 5.5(c) and (d), or in Fig. 5.5(b) and (e), while PbS sample data are shown in Fig. 5.5(e) and (f), or in Fig. 5.5(b) and (f). The *n*-type PbTe sample EMIMs can be found in Fig. 5.5(g) and (h). The samples under this study did not have the exact same carrier concentration, and thus, the useful quantity to be compared among PbQs is the difference between energy

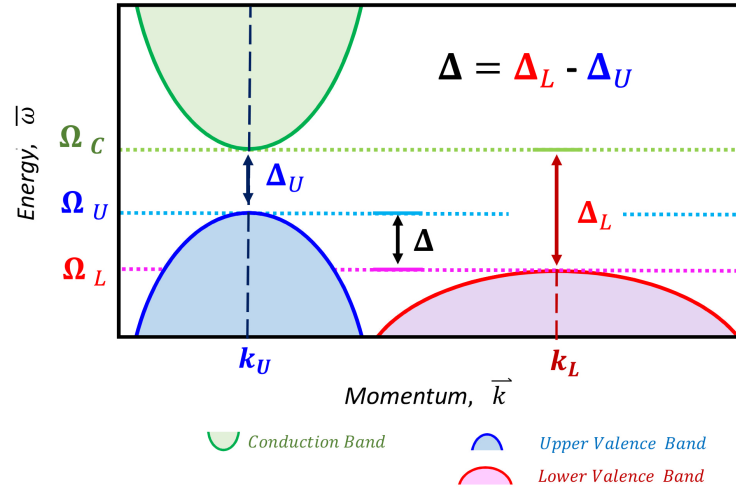


FIGURE 5.6: **Schematic band structure of PbQ.**

The general band structure of Lead chalcogenides with significant energy, momentum values and band gaps. Conduction band (CB) which is an electron band, is centered at the momentum  $\mathbf{k}_U$  and drawn in green. The upper hole valence band (UVB), drawn in blue is also centered at the same momentum  $\mathbf{k}_U$ . The minimum of the CB is  $\Omega_C$  and the maximum of the UVB is  $\Omega_U$ . The direct band gap between CB and UVB is denoted by  $\Delta_U$ . The lower hole valence band (LVB), drawn in red is centered at the momentum  $\mathbf{k}_L$  and the maximum of the LVB is  $\Omega_L$ . The indirect band gap between CB and LVB is denoted as  $\Delta_L$ . The difference between  $\Delta_L$  and  $\Delta_U$  is marked as  $\Delta$ , and it is the energy separation between UVB and LVB. Note: the curvature of the LVB is less than that of the UVB; hence the holes in the LVB are heavier compared to the holes in UVB.

gaps of lower and upper bands which is the parameter  $\Delta$ . Table 5.2 shows that the  $\Delta$  is largest for PbS and smallest for PbTe, while in between for PbSe.

TABLE 5.2: Values of  $\Delta_L$ ,  $\Delta_U$ , and  $\Delta$  obtained from  $n$ -type PbTe, PbSe, and PbS samples at  $T \sim 100\text{K}$

Material	$\Delta_U$ (meV)	$\Delta_L$ (meV)	$\Delta$ (meV)
PbTe	190	320	130
PbSe	204	594	390
PbS	309	838	529

## 5.4 Temperature Evolution of the Bands

In order to investigate the relationship between the temperature dependent thermopower, and the temperature evolution of the band structure, the above procedure for determining band gaps ( $\Delta_U$ ,  $\Delta_L$ ) and relative positions ( $\Delta$ ) was repeated for a range of temperatures, for each Lead chalcogenide (PbQ) sample. Subsequent temperature dependent energy density curves (EDCs) are summarized in Fig. 5.7. Samples used in obtaining these EDCs are as follows.

For Fig. 5.7(a) and (b), PbTe-#1 was used while for (c) and (d), another PbTe sample (#2) was analyzed. All PbTe samples depicted here are of *p*-type. In terms of *n*-type data, respectively for Fig. 5.7(e) and (f), samples labeled PbTe-#1 and PbTe-#2 were used. Similarly, in Fig. 5.7(g) and (h) PbS samples labeled #1 and #2 were considered.

According to the procedures explained in the section 5.3.1 and the section 5.3.2, band edges of UVBs,  $\Omega_U$  were determined using EDCs shown on the left side of the Fig. 5.7. Related constructions are marked in blue lines and arrows. For the case of *n*-type PbSe and PbS samples on Fig. 5.7(e) and (g), CB edges,  $\Omega_C$  were also detectable, as shown in green slope fits. As shown with the aid of black lines and arrows on the EDCs on the right side of the Fig. 5.7, band edges of LVBs,  $\Omega_L$  were determined as well.

With temperature dependent energies corresponding to the band edges,  $\Omega_U(T)$ ,  $\Omega_L(T)$ , and  $\Omega_C(T)$  in hand, equation 5.3 and equation 5.4 were used to obtain temperature dependent band gaps,  $\Delta_U(T)$  and  $\Delta_L(T)$  for both *n*-type PbSe and PbS. These results are presented in the Fig. 5.8(a) and (b), respectively.

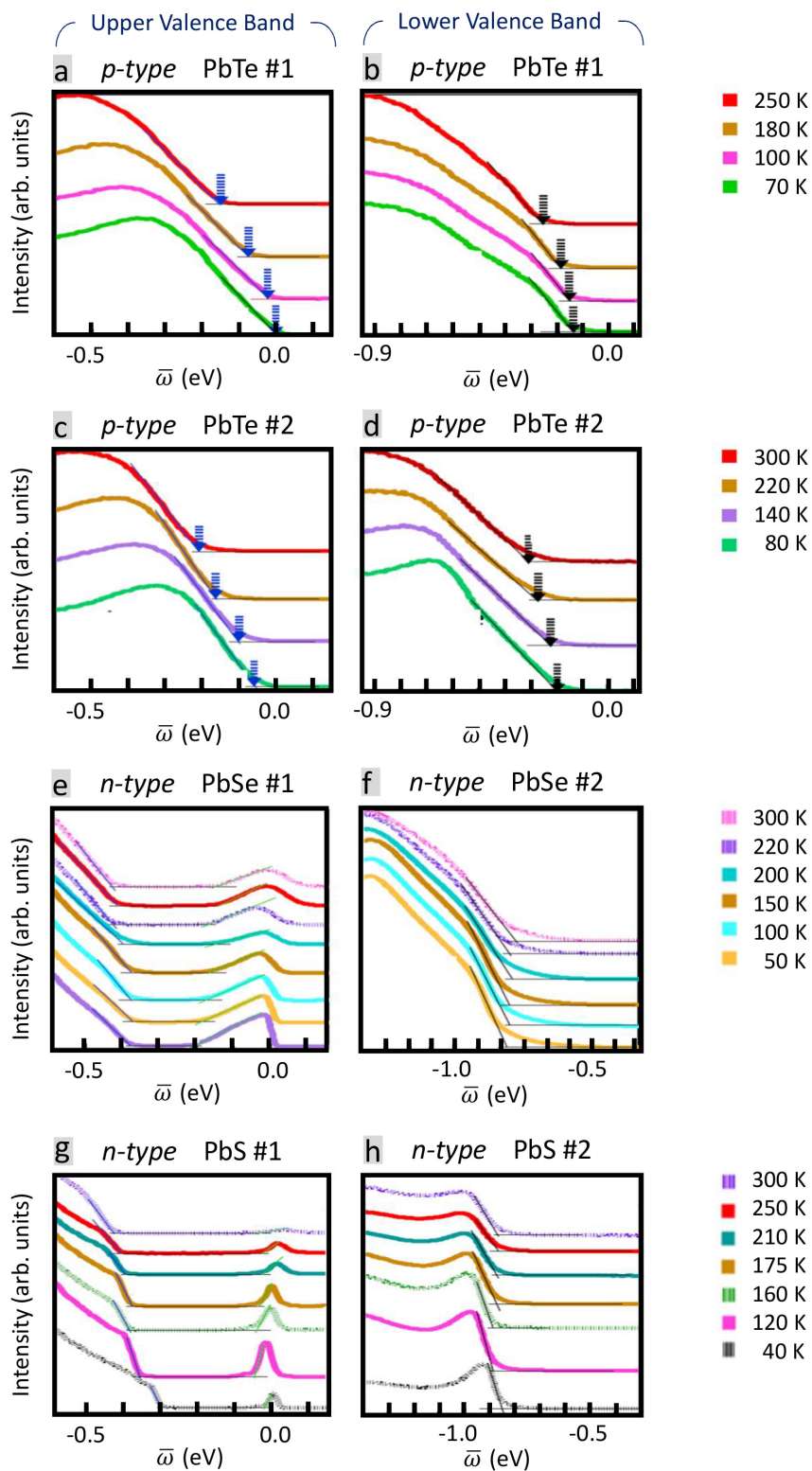


FIGURE 5.7: Temperature evolution of the band edges in Lead Chalcogenides.

Please see the next page for the details.

**Temperature evolution of the band edges in Lead chalcogenides.**

Continued from the previous page ...

Energy distribution curves (EDCs) as a function of temperature are shown. EDCs on the Left are taken at the momentum location  $\mathbf{k}_U$ , and contain band edges of upper valence band (UVB). for  $n$ - type samples, the conduction band (CB) edges are also captured. EDCs on the right are taken at the momentum location  $\mathbf{k}_L$ , and contain band edges of lower valence band (LVB). **(a, b)** The  $p$ -type PbTe#1 sample was used to determine UVB (a) and LVB (b) edges. **(c, d)** The  $p$ -type PbTe#2 sample was used to determine UVB (c) and LVB (d) edges. **(e)** The  $n$ -type PbSe#1 sample was used in determining UVB an CB edges. **(f)** The  $n$ -type PbSe#2 sample was used in determining LVB edge. **(g)** The  $n$ -type PbS#1 sample was used in determining UVB an CB edges. **(h)** The  $n$ -type PbS#2 sample was used in determining LVB edge. On (a), (c), (e) and (g), fits (blue lines) through foward slopes and flat background are used to extrpolate UVB maxima at  $\bar{\omega} \sim \Omega_U$ . Similarly on (e) and (g), green lines were fitted to identify CB minima at  $\bar{\omega} \sim \Omega_C$ . On (b), (d), (f) and (h), similar abrupt changes in slope of the EDCs at  $\bar{\omega} \sim \Omega_L$  were identified as LVB maxima. on (a), (c), (b) and (d), blue and black arrows point  $\Omega_U$ 's and  $\Omega_L$ 's, respectively.

---

From these data, or via the qualitative observation of EDCs in Fig. 5.7, it is clear that the lower valence band gap  $\Delta_L$  depends rather weakly on temperature compared to the upper valence band gap,  $\Delta_U$  which grows significantly with the rising temperature. These band gap values were then used to plot the temperature evolution of the upper and lower valence band separation  $\Delta$ , for  $n$ -type PbSe and PbS using the equation 5.5. The temperature dependent behavior of  $\Delta$  values are as shown in Fig.5.8(c).

Since  $\Omega_C$  of the  $p$ -type PbTe samples can't be determined as its conduction band lies in the un-occupied side of its band structure,  $\Delta_U(T)$  and  $\Delta_L(T)$  values for these  $p$ -type samples can not be directly evaluated. However, The upper and lower valence band separation,  $\Delta$  can still be determined by means of  $\Omega_U(T)$  and  $\Omega_U(T)$ , using the equation 5.6 and  $\Delta(T)$  evolution for all three Lead chalcogenides were found as in Fig.5.8(c).

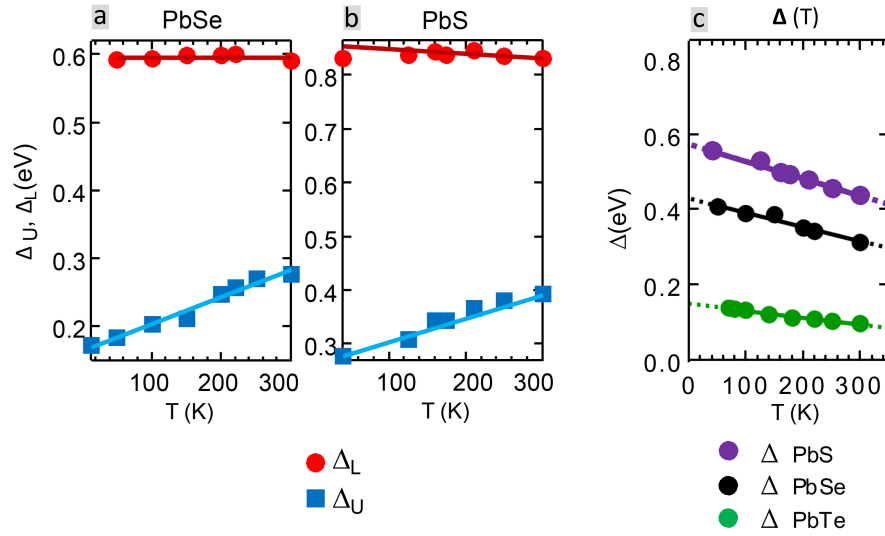


FIGURE 5.8: **Temperature evolution of band gaps in Lead Chalcogenides.** (a, b) Temperature dependence of the upper band gap,  $\Delta_U (= \Omega_C - \Omega_U)$  and the lower band gap,  $\Delta_L (= \Omega_C - \Omega_L)$  for (a) PbSe and (b) PbS. (c) Gap separation  $\Delta (= \Omega_U - \Omega_L)$  as a function of temperature,  $T$  for PbSe, PbS and PbTe.  $\Delta$  shows a linear monotonic decrease over temperature for all the Lead chalcogenides.

## 5.5 Explanation of the Thermoelectric Efficiency of Lead Chalcogenides

The observation of the temperature dependent increase of the upper valence band gap,  $\Delta_U$  is consistent with the positive temperature coefficients of the fundamental band gap found by optical experiments of Lead chalcogenides [191, 200–202]. It should be noted that such a positive rate of change in the band gap with temperature in Lead chalcogenides (PbQ) is opposite to the behavior of most other semiconductors. This anomaly is what helps PbQ in achieving high thermoelectric efficiency at elevated temperatures, as explained below.

From the Fig. 5.8(c), it is evident that the valence band separation,  $\Delta$  of each PbQ sample decreases monotonically with increasing temperature in the temperature range of the presented measurements. This downward trend of  $\Delta(T)$  can be well represented by

straight lines. A characteristic *band crossover temperature*,  $T^*$ , at which the maximum of the LVB is expected to level with the UVB maximum, can be defined. This  $T^*$  can be estimated via linear extrapolation of  $\Delta(T)$  to zero, and such estimated values for PbQ were found to be;

- PbTe:  $T^* \sim 813$  K
- PbSe:  $T^* \sim 1148$  K
- PbS :  $T^* \sim 1296$  K

Although such an estimation of  $T^*$  involves an extrapolation over a broad temperature range, the values of  $T^*$  obtained from this ARPES study agree reasonably well with recent magnetic and optical measurements [190, 191]. Further details on the connection between various attributes of above presented temperature dependent ARPES measurements and those from the proceeding literature are summarized in the table 5.3.

The monotonic temperature dependence of  $\Delta$  discussed above suggests that the PbQs should become semiconductors with indirect band gap for  $T > T^*$ , where the heavy hole LVB maximum rises in energy above the maximum of the light hole UVB. This is illustrated in the Fig. 5.9(b). As the temperature approaches  $T^*$  and the valence band separation becomes  $\Delta(T = T^*) \sim k_{\mathbf{B}}T^*$ , the charge transport in PbQ should be dominated by the heavy holes from the LVB, created due to the thermal excitations. This band convergence increases the density of states of heavier holes, as within the same energy window of  $k_{\mathbf{B}}T$ , more carriers are accessible on a flat band like LVB, compared to a band of higher curvature like UVB, As illustrated in the Fig. 5.9. This number enhancement of carriers results in an enhanced *Seebeck coefficient* and *thermoelectric power factor* at higher temperatures.

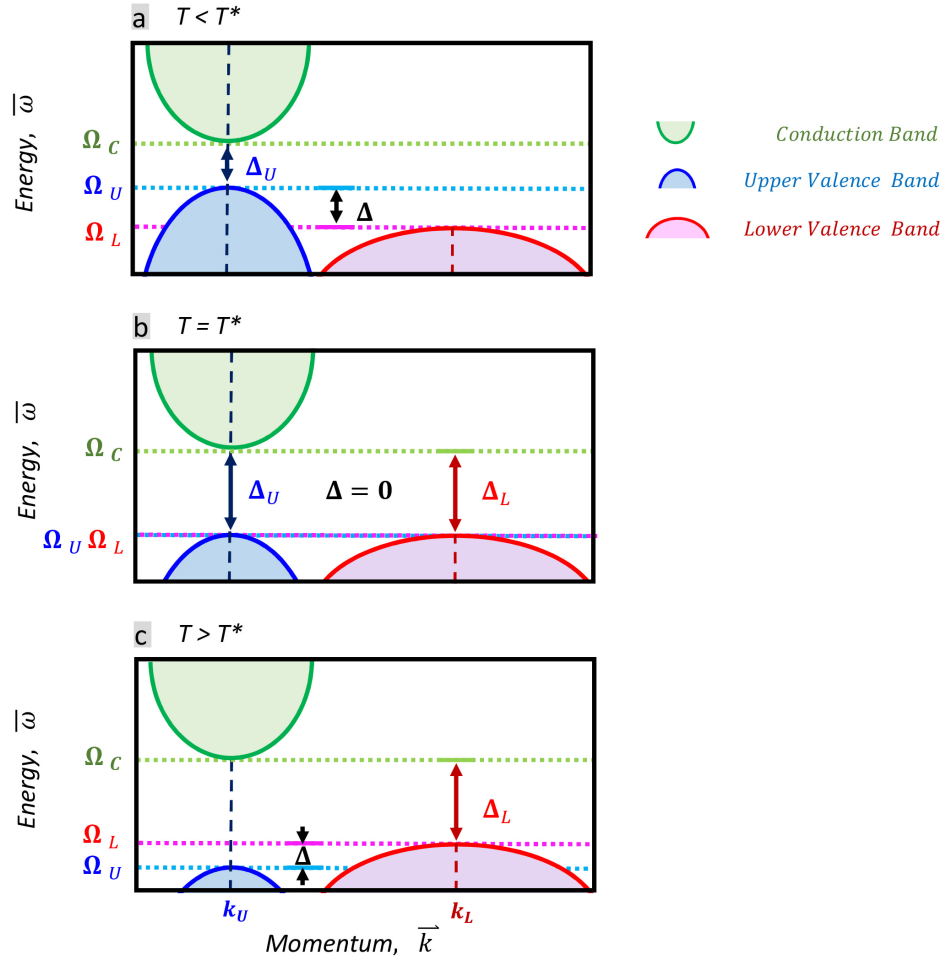


FIGURE 5.9: **Temperature evolution of the band structure of Lead Chalcogenides.**

Conduction electron band (CB) in green, and the upper hole valence band (UVB) in blue are centered at the momentum,  $\mathbf{k}_U$  and are separated in energy with a direct band gap of  $\Delta_U$ . The lower hole valence band (LVB) in red is centered at a different momentum,  $\mathbf{k}_L$  and is separated from the CB with an indirect band gap of  $\Delta_L$ . The diagram illustrates how these bands in a generic Lead chalcogenide (PbQ) evolve with temperature,  $T$  compared to the characteristic band crossover temperature,  $T^*$ . (a) At lower temperatures,  $T < T^*$ , the LVB lies below the UVB and PbQ is a direct bandgap semiconductor. (b) At the crossover temperature,  $T = T^*$ , both LVB and UVB maxima align to the same energy ( $\Omega_U = \Omega_L$ ). (c) At higher temperatures,  $T > T^*$ , the LVB rises above the UVB and PbQ becomes an indirect bandgap semiconductor. The LVB has less curvature and thus heavy holes compared to that of the UVB, and such a flat band can accommodate more holes for a given  $k_B T$  energy window.

TABLE 5.3: Comparison of various parameters from this study with existing data for PbTe, PbSe and PbS.

	This study				Other studies			
	$\Delta_U$ (meV)	$\Delta$ (meV)	$\frac{d\Delta_U}{dT}$ (meV/K)	$\frac{d\Delta}{dT}$ (meV/K)	$\Delta_U$ (meV)	$\Delta$ (meV)	$\frac{d\Delta}{dT}$ (meV/K)	$\frac{d\Delta_U}{dT}$ (meV/K)
PbQ								
PbTe	100K: 190	0K: 150 100K: 130 300K: 96	0.19		4K: 190 [203] 191 [204] 100K: 220, 235 [201] 300K: 290, 320 [205] 296 [191] 297, 320 [201]	0K: 170 [206] 140 [192, 207] 165 [201] 150~200 [208] 150K: 140 [201] 100 [209] 300K: 40 [201] 80 [210, 211]	0.41 [201] 0.45 [212] 0.32 [191]	0.32 [191] 0.19 [213] 0.2 [214]
PbSe	4K: 167 100K: 204 300K: 278	0K: 428 100K: 390 300K: 312			4K: 165 [203] 140 [204] 77K: 176 [203] 165 [215] 300K: 270 [191] 260, 290 [205] 275 [215]	0K: 250~350 [216] 300 [217]	0.45 [215] 0.41 [218] 0.32 [191]	0.32 [191]
PbS	4K: 267 125K: 309 300K: 393	0K: 591 125K: 529 300K: 438	0.45	0.44	4K: 286 [203] 281 [204] 77K: 307 [203] 300 [216] 300K: 370, 410 [205] 412 [191]	300 [217]	0.45 [219]	0.32 [191]

Also, in another perspective, bipolar effects arising from the intrinsic carrier activation is usually a factor that negatively affects the *thermoelectric figure of merit*,  $ZT$  at high temperatures. The indirect nature of the bandgap for high temperature  $T > T^*$  will mitigate these bipolar effects by reducing the probability of exciting electron–hole pairs with equal momenta, by de-tuning susceptible holes states in the upper valence band, from the electronic states with similar momentum in the conduction band.

All these mechanisms are responsible for the superior thermoelectric performance of Lead chalcogenides at elevated temperatures, and are rooted in the temperature influenced convergence of light (upper) and heavy (lower) hole valence bands.

## 5.6 Summary

A temperature dependent Angle Resolved Photoemission Spectroscopy (ARPES) investigation was conducted in order to probe electronic structures of Lead chalcogenides; PbTe, PbSe, and PbS. Several  $n$ - and  $p$ - type samples of these narrow bandgap semiconductors were analyzed toward an objective of explaining their extraordinary thermoelectric performances at elevated temperatures, by understanding the general electronic band structure. First, the valence band structure was probed, and then, the temperature evolution of this structure was investigated. The main observations are as follows.

- The band structure of Lead chalcogenides:
  - i. An upper hole valence band (UVB) was detected which lies directly below the conduction electron band (CB), establishing a direct bandgap.

- ii. A previously undetected lower hole valence band (LVB) was experimentally observed for the first time. Due to its location on the momentum space being different from the UVB, this band has an indirect gap with the CB.
  - iii. The curvature of the LVB was smaller than that of the UVB, making holes in the LVB heavier than the holes in the UVB.
  - iv. The energy separation between band maxima of the LVBs and the UVBs at  $T \sim 100\text{K}$  was largest in PbS and smallest in PbTe.
- The temperature evolution of the band structure:
    - i. For  $T < T^*$  : The upper valence band (UVB) was located above the lower valence band (LVB) in energy. Thus, Lead chalcogenides for lower energies are direct bandgap semiconductors.
    - ii. With the rise of the temperature, the UVB moved down in energy while any shift in LVB was insignificant. The UVB–CB (direct) gap increased with temperature while the LVB–CB (indirect) gap was practically stationary. The difference between UVB and LVB maxima decreased monotonically with the increase of temperature, which is referred to as valence band convergence. This is an anomalous phenomenon compared to the usual behavior of semiconductors.
    - iii. For  $T = T^*$  : Band maxima of both upper and lower hole valence bands aligned in energy. The characteristic *band crossover temperature*,  $T^*$ , is defined as the temperature which this phenomenon occurs.

- iv.** For  $T > T^*$  : The LVB shifts above UVB maximum, moving closer to the CB. As a result, in such elevated temperatures, Lead chalcogenides behave as indirect bandgap semiconductors.

The phenomena of band convergence has long been debated to be the driving factor behind extraordinary thermoelectric performances of these Lead chalcogenide compounds at elevated temperatures. Above reported study confirms this mechanism by means of the direct experimental observation of the LVB, and the temperature dependent valence band shifts leading to their convergence and subsequent crossover. This has two main implications on the enhancement of the thermometric efficiency.

- i.** The relative flatness of the LVB, compared to the UVB, enables the excitation of more carriers per same  $k_{\mathbf{B}}T$  energy window. Therefore, for  $T \geq T^*$ , where this flatter LVB lies close to the CB, the carrier (hole) density of states is enhanced.
- ii.** Bipolar effects arising from intrinsic carrier activation reduces thermometric performance. In general, these effects become more pronounced with the increase of temperature. Contrary to this general tendency, in this special case of Lead chalcogenides, the primary bandgap for  $T > T^*$  (i.e., the LVB–CB gap) becomes indirect, reducing the probability of electron-hole excitations occurring at the same momentum.

The outstanding thermoelectric efficiency of Lead chalcogenides is thus explained with the aid of temperature dependent ARPES band structure analysis.

It should be noted that the ARPES in this study was used as a probe sensitive to a two-dimensional surface Brillouin zone, which was the projection on the crystallographic

(001) plane in this particular case. There were several high symmetry points and lines from the bulk Brillouin zone corresponding to the region on the surface Brillouin zone projection, where the LVB was observed. This prevented the mapping of a one-to-one correspondence of surface-to-bulk Brillouin zones in the case of LVB. More experiments sensitive to three dimensional band structure are necessary to relate the LVB to a unique momentum coordinate in the bulk Brillouin zone of Lead chalcogenides.

---

## Chapter 6

# Conclusions

### 6.1 Charge Density Wave Phase of Transition Metal Dichalcogenides

Properties of the incommensurate charge density wave (CDW) order in the quasi-two-dimensional transition metal dichalcogenide (TMD) compound  $2H - \text{TaS}_2$  were investigated in comparison to  $2H - \text{NbSe}_2$ , and  $2H - \text{TaSe}_2$ . Angle resolved photoemission spectroscopy (ARPES) was primarily used as the experimental technique in the reported band structure studies. Analysis was carried out in energy, momentum and temperature domains and the majority of the observations are qualitatively generalizable over the whole family of layered  $2H -$  TMDs. In these materials, electron and hole Fermi pockets in the momentum space are in the shape of concentric double-walled barrels about both K and  $\Gamma$  high symmetry points.

The first study was focused on the CDW energy gap which is observed to be momentum specific.  $\Gamma$ -centric Fermi surface barrels exhibit no gap, while K-centric Fermi surface

barrels are entirely or at least partially gapped depending on the TMD material. Moreover, this energy gap is particle-hole asymmetric with respect to the chemical potential.

A peculiar observation regarding this energy gap is its existence at temperatures higher than the CDW transition temperature. This phenomena, known as *pseudogap*, can be explained using the behaviors of the amplitude and phase components of the CDW order parameter. In elevated temperatures, even though the long-range CDW phase coherence goes extinct, a short-range ordering of charge could persist in certain regions of the sample. This non-zero local amplitude of the CDW order parameter would manifest as a pseudogap.

Some systematic differences between several properties of comparable TMD compounds are observed as well. When considering the momentum specificity of the CDW energy gap, in  $2H - \text{TaS}_2$ , the gap is observed at all the momentum locations on both K-centric inner and outer Fermi surface barrels whereas in  $2H - \text{NbSe}_2$ , the gap opens up only in specific locations on K-centric Fermi barrels. The size of the  $\Gamma$ -centric Fermi surface barrels, relative to the lattice dimensions of each compound, are almost the same among both compounds. In contrast, the size of K-centric Fermi surface barrels in  $2H - \text{TaS}_2$  is smaller compared to that of  $2H - \text{NbSe}_2$ .

The universal features of the incommensurate charge density wave (CDW) phase in  $2H -$  TMD family, as well as the differences among members, can be explained with a tight binding model with strong electron-quasiparticle coupling which takes the differences of orbital orientations between these materials into account. These differences in orbital arrangements and its consequences on the momentum space might be the determining factor of the CDW transition temperature as well.

The traditional explanation of the formation of CDWs, namely, the Fermi surface nesting due to Peierls instability, can be ruled out as the CDW mechanism of  $2H$ -TMDs since the observed CDW wave vectors in these TMD compounds were not compatible with the predicted nesting vectors. This opened up an investigation to other potential mechanisms.

An extended ARPES study on the renormalization signatures in the electronic band dispersion of  $2H$ -TaS<sub>2</sub> was conducted with the objective of identifying the nature of underlying collective modes. These renormalizations are observed throughout the momentum space, and the energies of several such signatures agree with published phonon frequencies. The magnitude of this electron-phonon coupling is slightly momentum dependent and is in qualitative agreement with similar studies on  $2H$ -NbSe<sub>2</sub>. The temperature independent nature of these renormalization signatures corroborates the phononic origin as well. Therefore, the work presented in this thesis suggests that the mechanism behind the incommensurate charge density wave phase of the  $2H$ -polytype of transition metal dichalcogenides is the momentum-anisotropic electron-phonon coupling, rather than the Fermi surface nesting.

## 6.2 Thermoelectric Performance of Lead Chalcogenides

Angle resolved photoemission spectroscopy (ARPES) was utilized in order to study the temperature evolution of the valence band structure of lead chalcogenides (PbQ). The objective of the experiment was to investigate the reason behind the remarkable improvement of the thermoelectric performance of these narrow bandgap semiconductors at elevated temperatures. Several *n* and *p* doped samples of PbTe, PbSe, and PbS were analyzed.

The valence band structure of PbQ consists of an upper valence band (UVB) and a lower valence band (LVB). These hole bands are centered at different momentum locations in such a way that the UVB establishes a direct bandgap with the conduction band (CB), while the LVB-CB bandgap is indirect. This is the first reported experimental observation of the LVB in PbQ. The curvatures of the valence bands are different and therefore imply that the holes in the LVB are heavier than the holes in the UVB. Also, the LVB lies deeper in energy with respect to the UVB at normal (room) temperatures. The separation between the maxima of LVB and UVB, measured at  $\sim 100$  K, is the largest in PbS and the smallest in PbTe, following the converse of the size of the chalcogen.

At room temperature, the UVB maximum is above the LVB maximum in energy. Therefore, PbQ are direct bandgap semiconductors in normal temperatures. When the temperature is raised, the UVB sinks in energy, but any significant shift of the LVB is not observed. This led to the convergence of valence hole bands, as the difference between UVB and LVB maxima decreased monotonically with the increase of temperature. This band convergence is anomalous with respect to usual semiconductors. At a certain crossover temperature, characteristic to each compound, the maxima of both the UVB

and the LVB will align. Beyond this crossover temperature, the LVB will rise above the UVB, effectively transforming the PbQ sample to an indirect bandgap semiconductor comprising of a valence band with heavier holes.

At elevated temperatures, more carriers per given  $k_{\mathbf{B}}T$  energy window can be excited from the LVB which is flatter compared to the UVB. This enhancement of carrier density is the primary effect toward improved thermoelectric efficiency. Also, the indirect nature of the bandgap at higher temperatures is unfavorable for intrinsic carrier activation, which would otherwise reduce the thermoelectric performance. Thus, the superior thermoelectric efficiency of lead chalcogenides can be explained by the temperature dependent convergence of light and heavy hole valence bands.

---

# Bibliography

- [1] P. Miro, M. Audiffred, and T. Heine. An atlas of two-dimensional materials. *Chem. Soc. Rev.*, 43:6537, 2014.
- [2] K. S. Novoselov, A. K. Geim, S. V. Morozov, D. Jiang, Y. Zhang, S. V. Dubonos, I. V. Grigorieva, and A. A. Firsov. Electric field effect in atomically thin carbon films. *Science*, 306:666–669, 2004.
- [3] A. Castellanos-Gomez. Why all the fuss about 2D semiconductors. *Nature Photonics*, 10:202–204, 2016.
- [4] S. Manzeli, D. Ovchinnikov, D. Pasquier, O. V. Yazyev, and A. Kis. 2D transition metal dichalcogenides. *Nature Reviews Materials*, 2:17033, 2017.
- [5] M. Chhowalla, H.S. Shin, G. Eda, L.J. Li, K.P. Loh, and H. Zhang. The chemistry of two-dimensional layered transition metal dichalcogenide nanosheets. *Nature Chemistry*, 5:263–275, 2013.
- [6] J. A. Wilson, F. J. Di Salvo, and S. Mahajan. Charge-density waves and superlattices in the metallic layered transition metal dichalcogenides. *Adv. Phys.*, 24:117, 1974.
- [7] J. A. Wilson and A. D. Yoffe. The transition metal dichalcogenides discussion and interpretation of the observed optical, electrical and structural properties. *Adv. Phys.*, 18:193, 1969.
- [8] P. Monceau. Electronic crystals: an experimental overview. *Adv. Phys.*, 61:325, 2012.
- [9] R. H. Friend and A. D. Yoffe. Electronic properties of intercalation complexes of the transition metal dichalcogenides. *Adv. Phys.*, 36:1, 1987.
- [10] K. Rossnagel. On the origin of charge-density waves in select layered transition-metal dichalcogenides. *J. Phys.: Condens. Matter*, 23:213001, 2011.

- [11] K. E. Wagner, E. Morosan, Y. S. Hor, J. Tao, Y. Zhu, T. Sanders, T. M. McQueen, H. W. Zandbergen, A. J. Williams, D. V. West, and R. J. Cava. Tuning the charge density wave and superconductivity in  $\text{Cu}_x\text{TaS}_2$ . *Phys. Rev. B*, 78:104520, 2008.
- [12] E. Morosan, H. W. Zandbergen, B. S. Dennis, J. W. G. Bos, Y. Onose, T. Klimczuk, A. P. Ramirez, N. P. Ong, and R. J. Cava. Superconductivity in  $\text{Cu}_x\text{TiSe}_2$ . *Nat. Phys.*, 2:544, 2006.
- [13] E. Morosan, K. E. Wagner, Liang L. Zhao, Y. Hor, A. J. Williams, J. Tao, Y. Zhu, and R. J. Cava. Multiple electronic transitions and superconductivity in  $\text{Pd}_x\text{TiSe}_2$ . *Phys. Rev. B*, 81:094524, 2010.
- [14] F. J. Di Salvo, J. A. Wilson, and J. V. Waszczak. Localization of conduction electrons by Fe, Co, and Ni in 1T-TaS<sub>2</sub> and 1T-TaSe<sub>2</sub>. *Phys. Rev. Lett.*, 36:885, 1976.
- [15] S. J. Hillenius, R. V. Coleman, E. R. Domb, and D. J. Sellmyer. Magnetic properties of iron-doped layer-structure dichalcogenides. *Phys. Rev. B*, 19:4711, 1979.
- [16] J. Kuneš, L. Baldassarre, B. Schächner, K. Rabia, C. A. Kuntscher, Dm. M. Korotin, V. I. Anisimov, J. A. McLeod, E. Z. Kurmaev, and A. Moewes. Metal-insulator transition in  $\text{NiS}_{2-x}\text{Se}_x$ . *Phys. Rev. B*, 81:035122, 2010.
- [17] L. J. Li, X. D. Zhu, Y. P. Sun, H. C. Lei, B. S. Wang, S. B. Zhang, X. B. Zhu, Z. R. Yang, and W. H. Song. Superconductivity of Ni-doping 2H-TaS<sub>2</sub>. *Physica C*, 470:313, 2010.
- [18] N. Barišić, I. Smiljanić, P. Popčević, A. Bilušić, E. Tutiš, A. Smontara, H. Berger, J. Jaćimović, O. Yuli, and L. Forró. High-pressure study of transport properties in  $\text{Co}_{0.33}\text{NbS}_2$ . *Phys. Rev. B*, 84:075157, 2011.
- [19] J. M. E. Harper, T. H. Geballe, and F. J. Di Salvo. Thermal properties of layered transition metal dichalcogenides at charge density wave transitions. *Phys. Rev. B*, 15:2943, 1977.
- [20] M. H. van Maaren and H. B. Harland. An energy band model of Nb - and Ta -dichalcogenide superconductors. *Phys. Lett. A*, 29A:571, 1969.
- [21] S. Nagata, T. Aochi, T. Abe, S. Ebisu, T. Hagino, Y. Seki, and K. Tsutsumi. Superconductivity in the layered compound 2H-TaS<sub>2</sub>. *J. Phys. Chem. Solids*, 53:1259, 1992.
- [22] D. C. Freitas, P. Rodière, M. R. Osorio, E. Navarro-Moratalla, N. M. Nemes, V. G. Tissen, L. Cario, E. Coronado, M. García-Hernández, S. Vieira, M. Nú

- nez Regueiro, and H. Suderow. Strong enhancement of superconductivity at high pressures within the charge-density-wave states of  $2H\text{-TaS}_2$  and  $2H\text{-TaSe}_2$ . *Phys. Rev. B*, 93:184512, 2016.
- [23] E. Navarro-Moratalla, J. O. Island, S. Ma nas Valero, E. Pinilla-Cienfuegos, A. Castellanos-Gomez, J. Quereda, G. Rubio-Bollinger, L. Chirolli, J. A. Silva-Guillén, N. Agraït, G. A. Steele, F. Guinea, H. S. J. van der Zant, and E. Coronado. Enhanced superconductivity in atomically thin  $\text{TaS}_2$ . *Nat. Commun.*, 7:11043, 2016.
- [24] X. Zhu, Y. Sun, S. Zhang, J. Wang, L. Zou, L. E. DeLong, X. Zhu, X. Luo, B. Wang, G. Li, Z. Yang, and W. Song. Anisotropic intermediate coupling superconductivity in  $\text{Cu}_{0.03}\text{TaS}_2$ . *J. Phys.: Condens. Matter*, 21:145701, 2009.
- [25] L. Fang, Y. Wang, P. Y. Zou, L. Tang, Z. Xu, H. Chen, C. Dong, L. Shan, and H. H. Wen. Fabrication and superconductivity of  $\text{Na}_x\text{TaS}_2$  crystals. *Phys. Rev. B*, 72:014534, 2005.
- [26] A. Lerf, F. Sernetz, W. Biberacher, and R. Schöllhorn. Superconductivity in layered ternary chalcogenides  $\text{A}_x\text{TaS}_2$  and  $\text{A}_x\text{NbS}_2$  and influence of topotactic solvation. *Mater. Res. Bull.*, 14:797, 1979.
- [27] F. J. Di Salvo, G. W. Hull Jr., L. H. Schwartz, J. M. Voorhoeve, and J. V. Waszczak. Metal intercalation compounds of  $\text{TaS}_2$ : Preparation and properties. *J. Chem. Phys.*, 59:1922, 1973.
- [28] F. R. Gamble, J. H. Osiecki, and F. J. DiSalvo. Some superconducting intercalation complexes of  $\text{TaS}_2$  and substituted pyridines. *J. Chem. Phys.*, 55:3525, 2003.
- [29] R. M. Fleming and R. V. Coleman. Superconductivity in dilute alloys of  $\text{TaS}_2$  with Fe. *Phys. Rev. Lett.*, 34:1502, 1975.
- [30] J. van den Berg and P. Cossee. Structural aspects and magnetic behaviour of  $\text{NbS}_2$  and  $\text{TaS}_2$  containing extra metal atoms of the first transition series. *Inorg. Chim. Acta*, 2:143, 1968.
- [31] L. J. Li, W. J. Lu, X. D. Zhu, L. S. Ling, Z. Qu, and Y. P. Sun. Fe doping induced superconductivity in the charge-density-wave system  $1T\text{-TaS}_2$ . *Europhys. Lett.*, 97:29902, 2012.
- [32] L. Li, W. Lu, X. Zhu, and Y. Sun. Effect of Fe doping on charge density wave in  $1T\text{-TaS}_2$ : Instability and induced superconductivity. *J. Phys.: Conf. Ser.*, 400:022061, 2012.

- [33] Y. Yu, F. Yang, X.-F. Lu, Y.-J. Yan, Y.-H. Cho, L. Ma, X. Niu, S. Kim, Y.-W. Son, D. Feng, S. Li, S.-W. Cheong, X.-H. Chen, and Y. Zhang. Gate tunable phase transitions in thin flakes of 1T-TaS<sub>2</sub>. *Nat. Nanotechnol.*, 10:270, 2015.
- [34] D. Bhoi, S. Khim, W. Nam, B. S. Lee, Chanhee Kim, B.-G. Jeon, B. H. Min, S. Park, and K. H. Kim. Interplay of charge density wave and multiband superconductivity in 2H-Pd<sub>x</sub>TaSe<sub>2</sub>. *Sci. Rep.*, 6:24068, 2016.
- [35] M. Porer, U. Leierseder and J. M. Ménard, H. Dachraoui, L. Mouchliadis, I. E. Perakis, U. Heinzmann, J. Demsar, K. Rossnagel, and R. Huber. Non-thermal separation of electronic and structural orders in a persisting charge density wave. *Nature Materials*, 13:857–861, 2014.
- [36] J. G. Checkelsky, Minhyea Lee, E. Morosan, R. J. Cava, and N. P. Ong. Anomalous Hall effect and magnetoresistance in the layered ferromagnet Fe<sub>14</sub>TaS<sub>2</sub>: The inelastic regime. *Phys. Rev. B*, 77:014433, 2008.
- [37] D. J. Rahn, S. Hellmann, M. Kalläne, C. Sohrt, T. K. Kim, L. Kipp, and K. Rossnagel. Gaps and kinks in the electronic structure of the superconductor 2H-NbSe<sub>2</sub> from angle-resolved photoemission at 1 K. *Phys. Rev. B*, 85:224532, 2012.
- [38] L. F. Mattheiss. Band structures of transition metal dichalcogenide layer compounds. *Phys. Rev. B*, 8:3719, 1973.
- [39] X. Xi, L. Zhao, Z. Wang, H. Berger, L. Forró, J. Shan, and K. F. Mak. Strongly enhanced charge-density-wave order in monolayer NbSe<sub>2</sub>. *Nature Nanotechnology*, 10:765–769, 2015.
- [40] G. Y. Guot and W. Y. Liang. Electronic structures of intercalation complexes of the layered compound 2H-TaS<sub>2</sub>. *J. Phys. C: Solid State Phys.*, 20:4315, 1987.
- [41] Bilbao crystallographic server. URL <http://www.cryst.ehu.es/cgi-bin/cryst/programs/nph-kv-list?gnum=194&fig=f6ommp&what=data>.
- [42] J. C. Campuzano, H. Ding, M. R. Norman, M. Randeira, A. F. Bellman, T. Yokoya, T. Takahashi, H. Katayama-Yoshida, T. Mochiku, and K. Kadowaki. Direct observation of particle-hole mixing in the superconducting state by angle-resolved photoemission. *Phys. Rev. B*, 53:R14737–R14740, 1996.
- [43] H. Matsui, T. Sato, T. Takahashi, S.-C. Wang, H.-B. Yang, H. Ding, T. Fujii, T. Watanabe, and A. Matsuda. Bcs-like bogoliubov quasiparticles in high-T<sub>c</sub> superconductors observed by angle resolved photoemission spectroscopy. *Phys. Rev. Lett.*, 90:217002, 2003.

- [44] A. Kanigel, U. Chatterjee, M. Randeria, M.R. Norman, G. Koren, K. Kadowaki, and J.C. Campuzano. Evidence for pairing above the transition temperature of cuprate superconductors from the electronic dispersion in the pseudogap phase. *Phys. Rev. Lett.*, 101:137002, 2008.
- [45] J. Zhao, K. Wijayarathne, C. D. Malliakas, M. G. Kanatzidis, D. Y. Chung, G. Gu, and U. Chatterjee. Spectroscopic study of the charge density wave order in 2H-TaS<sub>2</sub>. *Proc.SPIE (Spintronics X)*, 10357:8, 2017.
- [46] A. Soumyanarayanan, M. M. Yee, Y. He, J. van Wezel, D. J. Rahn, K. Rossnagel, E. W. Hudson, M. R. Norman, and J. E. Hoffman. Quantum phase transition from triangular to stripe charge order in NbSe<sub>2</sub>. *Proc. Natl. Acad. Sci. USA*, 110:1623, 2013.
- [47] K. Wijayarathne, J. Zhao, C. Malliakas, D. Y. Chung, M. G. Kanatzidis, and U. Chatterjee. Spectroscopic signature of moment-dependent electron-phonon coupling in 2H-TaS<sub>2</sub>. *J. Mater. Chem. C*, 5:11310–11316, 2017.
- [48] G. Grüner. The dynamics of charge-density waves. *Rev. Mod. Phys.*, 60:1129, 1988.
- [49] J. G. Bednorz and K. A. Müller. Possible highT<sub>c</sub> superconductivity in the Ba–La–Cu–O system. *Z. Phys.*, 64:189–193, 1986.
- [50] P. A. Lee, N. Nagaosa, and X.G Wen. Doping a Mott insulator: Physics of high-temperature superconductivity. *Rev. Mod. Phys.*, 78:17–85, 2007.
- [51] J. Orenstein and A. J. Millis. Advances in the physics of high-temperature superconductivity. *Science*, 288:468–474, 2000.
- [52] T. Kasuya and T. Saso, editors. *Theory of Heavy Fermions and Valence Fluctuations*.
- [53] P. Gegenwart, Q. Si, and F. Steglich. Quantum criticality in heavy-fermion metals. *Nat. Phys.*, 4:186, 2008.
- [54] M. B. Salamon and M. Jaime. The physics of manganites: structure and transport. *Rev. Mod. Phys.*, 73:583–628, 2001.
- [55] E. Dagotto. Open questions in CMR manganites, relevance of clustered states and analogies with other compounds including the cuprates. *New J. Phys.*, 7:67/1–28, 2005.
- [56] J. A. Wilson, F. J. Di Salvo, and S. Mahajan. Charge density waves in metallic, layered, transition metal dichalcogenides. *Phys. Rev. Lett.*, 32:882, 1974.

- [57] G. A. Scholz, O. Singh, R. F. Frindt, and A. E. Curzon. Charge density wave commensurability in 2H-TaS<sub>2</sub> and Ag<sub>x</sub>TaS<sub>2</sub>. *Solid State Commun.*, 44:1455, 1982.
- [58] J. P. Tidman, O. Singh, A. E. Curzon, and R. F. Frindt. The phase transition in 2H-TaS<sub>2</sub> at 75 K. *Philos. Mag.*, 30:1191, 1974.
- [59] D. E. Moncton, J. D. Axe, and F. J. DiSalvo. Study of superlattice formation in 2H-NbSe<sub>2</sub> and 2H-TaSe<sub>2</sub> by neutron scattering. *Phys. Rev. Lett.*, 34:734, 1975.
- [60] D. E. Moncton, J. D. Axe, and F. J. DiSalvo. Neutron scattering study of the charge-density wave transitions in 2H-TaSe<sub>2</sub> and 2H-NbSe<sub>2</sub>. *Phys. Rev. B*, 16:801, 1977.
- [61] C. Goupil. *Continuum theory and modeling of thermoelectric elements*.
- [62] A. Volta. New memoir on animal electricity from Don Alessandro Volta (in Italian). *Annals of chemistry and natural history*, 5:132–144, 1794.
- [63] T. J. Seebeck. Magnetic polarization of metals and ores by temperature differences (in German). *Abhandlungen der Königlich Akademie der Wissenschaften zu Berlin*, :265–373, 1822.
- [64] H. C. Ørsted. New experiments by Mr. Seebeck on electro-magnetic actions (in French). *Annales de chimie*, 2:199, 1823.
- [65] B.C. Sales. Thermoelectric devices: refrigeration and power generations with no moving parts. *Encyclopedia of Materials: Science and Technology*, :9179–9185, 2001.
- [66] J. C. A. Peltier. New experiments on the heat effects of electric currents. *Annales de Chimie et de Physique*, 56:371–386, 1834.
- [67] W. Thomson. On a mechanical theory of thermo-electric currents. *Proceedings of the Royal Society of Edinburgh*, 3(42):91–98, 1851.
- [68] A. F. Ioffe. *Semiconductor thermoelements, and thermoelectric cooling*.
- [69] S. Hüfner. *Photoelectron spectroscopy- principles and applications*.
- [70] C.J. Vineis, A. Shakouri, A. Majumdar, and M. G. Kanatzidis. Nanostructured thermoelectrics: big efficiency gains from small features. *Adv. Mater.*, 22:3970, 2010.
- [71] J. Y. Pei, A. D. LaLonde, N. A. Heinz, and G. J. Snyder. High thermoelectric figure of merit in PbTe alloys demonstrated in PbTe–CdTe. *Adv. Energy Mater.*, 2:670, 2012.

- [72] M. S. Dresselhaus, G. Chen, M. Y. Tang, R. G. Yang, H. Lee, D. Z. Wang, Z. F. Ren, J.-P. Fleurial, and P. Gogna. New directions for low-dimensional thermoelectric materials. *Adv. Mater.*, 19:1043, 2007.
- [73] L.-D. Zhao, V. P. Dravid, and M. G. Kanatzidis. The panoscopic approach to high performance thermoelectrics. *Energy Environ. Sci.*, 7:251, 2014.
- [74] M. G. Kanatzidis. Nanostructured thermoelectrics: the new paradigm. *Chem. Mater.*, 22:648, 2010.
- [75] A. D. LaLonde, Y. Pei, and G. J. Snyder. Reevaluation of  $\text{PbTe}_{1-x}\text{I}_x$  as high performance n-type thermoelectric material. *Energy Environ. Sci.*, 4:2090, 2011.
- [76] S. N. Girard, J. He, X. Zhou, D. Shoemaker, C. M. Jaworski, C. Uher, V. P. Dravid, J. P. Heremans, and M. G. Kanatzidis. High performance Na-doped  $\text{PbTe-PbS}$  thermoelectric materials: electronic density of states modification and shape-controlled nanostructures. *J. Am. Chem. Soc.*, 133:16588, 2011.
- [77] Y. Pei, X. Shi, A. LaLonde, H. Wang, L. Chen, and G. J. Snyder. Convergence of electronic bands for high performance bulk thermoelectrics. *Nature*, 473:66, 2011.
- [78] K. Biswas, J. He, Q. Zhang, G. Wang, C. Uher, V. P. Dravid, and M. G. Kanatzidis. Strained endotaxial nanostructures with high thermoelectric figure of merit. *Nat. Chem.*, 3:160, 2011.
- [79] E. S. Božin, C. D. Malliakas, P. Souvatzis, T. Proffen, N. A. Spaldin, M. G. Kanatzidis, and S. J. L. Billinge. Entropically stabilized local dipole formation in lead chalcogenides. *Science*, 330:1660, 2010.
- [80] T. Keiber, F. Bridges, and B. C. Sales. Lead is not off center in  $\text{PbTe}$ : the importance of r- space phase information in extended X-ray absorption fine structure spectroscopy. *Phys. Rev. Lett.*, 111:095504, 2013.
- [81] L. Fu. Topological crystalline insulators. *Phys. Rev. Lett.*, 106:106802, 2011.
- [82] S.-Y. Xu, C. Liu, N. Alidoust, M. Neupane, D. Qian, I. Belopolski, J.D. Denlinger, Y.J. Wang, H. Li, L.A. Wray, G. Landolt, B. Slomski, J.H. Dil, A. Marcinkova, E. Morosan, Q. Gibson, R. Sankar, F.C. Chou, R.J. Cava, A. Bansil, and M.Z. Hasan. Observation of a topological crystalline insulator phase and topological phase transition in  $\text{PbTe}_{1-x}\text{I}_x$ . *Nat. Commun.*, 3:1192, 2012.
- [83] Y. Tanaka, Z. Ren, T. Sato, K. Nakayama, S. Souma, T. Takahashi, K. Segawa, and Y. Ando. Experimental realization of a topological crystalline insulator in  $\text{SnTe}$ . *Nat. Phys.*, 8:800, 2012.

- [84] P. Dziawa, B. J. Kowalski, K. Dybko, R. Buczko, A. Szczerbakow, E. Łusakowska, M. Szot, T. Balasubramanian, B. M. Wojek, M. H. Berntsen, O. Tjernberg, and T. Story. Topological crystalline insulator states in  $\text{PbTe}_{1-x}\text{I}_x\text{Se}$ . *Nat. Mater.*, 11: 1023, 2012.
- [85] Y. Okada, M. Serbyn, H. Lin, D. Walkup, W. Zhou, C. Dhital, M. Neupane, S. Xu, Y. J. Wang, R. Sankar, F. Chou, A. Bansil, M. Z. Hasan, S. D. Wilson, L. Fu, and V. Madhavan. Observation of dirac node formation and mass acquisition in a topological crystalline insulator. *Science*, 341:1496, 2013.
- [86] B. M. Wojek, P. Dziawa, B. J. Kowalski, A. Szczerbakow, A. M. Black-Schaffer, M. H. Berntsen, T. Balasubramanian, T. Story, and O. Tjernberg. Band inversion and the topological phase transition in  $(\text{Pb},\text{Sn})\text{Se}$ . *Phys. Rev. B*, 90:161202, 2013.
- [87] C. M. Polley, P. Dziawa, A. Reszka, A. Szczerbakow, R. Minikayev, J. Z. Domagala, S. Safaei, P. Kacman, R. Buczko, J. Adell, M. H. Berntsen, B. M. Wojek, O. Tjernberg, B. J. Kowalski, T. Story, and T. Balasubramanian. Observation of topological crystalline insulator surface states on (111)-oriented  $\text{PbTe}_{1-x}\text{I}_x\text{Se}$  films. *Phys. Rev. B*, 89:075317, 2014.
- [88] Y. Tanaka, T. Shoman, K. Nakayama, S. Souma, T. Sato, T. Takahashi, M. Novak Kouji Segawa, and Yoichi Ando. Two types of Dirac-cone surface states on the (111) surface of the topological crystalline insulator  $\text{SnTe}$ . *Phys. Rev. B*, 88: 235126, 2013.
- [89] M. Neupane, S.-Y. Xu, R. Sankar, Q. Gibson, Y. J. Wang, I. Belopolski, N. Alidoust, G. Bian, P. P. Shibayev, D. S. Sanchez, Y. Ohtsubo, A. Taleb-Ibrahimi, S. Basak, W.-F. Tsai, H. Lin, T. Durakiewicz, R. J. Cava, A. Bansil, F. C. Chou, and M. Z. Hasan. Topological phase diagram and saddle point singularity in a tunable topological crystalline insulator. *Phys. Rev. B*, 92:075131, 2015.
- [90] Y. Matsushita, H. Bluhm, T. H. Geballe, and I. R. Fisher. Evidence for charge Kondo effect in superconducting Tl-Doped  $\text{PbTe}$ . *Phys. Rev. Lett.*, 94:157002, 2005.
- [91] J. Zhao, C. D. Malliakas, K. Wijayarathne, V. Karlapati, N. Appathurai, D. Y. Chung, S. Rosenkranz, M. G. Kanatzidis, and U. Chatterjee. Spectroscopic evidence for temperature-dependent convergence of light- and heavy-hole valence bands of  $\text{PbQ}$  ( $Q = \text{Te}, \text{Se}, \text{S}$ ). *EPL*, 117:27006, 2017.
- [92] J. Zhao, K. Wijayarathne, A. Butler, J. Yang, C. D. Malliakas, D. Y. Chung, D. Louca, M. G. Kanatzidis, J. van Wezel, and U. Chatterjee. Orbital selectivity

- causing anisotropy and particle-hole asymmetry in the charge density wave gap of 2H-TaS<sub>2</sub>. *Phys. Rev. B*, 96:125103, 2017.
- [93] H. Hertz. Ueber einen einfluss des ultravioletten lichtes auf die electriche Entladung. *Ann. Phys.*, 17:983, 1887.
- [94] The Nobel Prize in Physics 1921, Nobel Foundation. URL <https://www.nobelprize.org/prizes/physics/1921/summary/>.
- [95] The Nobel Prize in Physics 1923, Nobel Foundation. URL <https://www.nobelprize.org/prizes/physics/1923/ceremony-speech/>.
- [96] A. Damascelli. Probing the electronic structure of complex systems by ARPES. *Physica Scripta*, T109:61, 2013.
- [97] U. Chatterjee. PhD thesis, University of Illinois at Chicago, USA, 2007.
- [98] G. D. Mahan. Theory of photoemission in simple metals. *Phys. Rev. B*, 2:4334, 1970.
- [99] K Mitchell and R. H. Fowler. The theory of the surface photoelectric effect in metals—I. *Proc. R. Soc. London A*, 146:442, 1934.
- [100] R. E. B. Makinson. The surface photoelectric effect. *Phys. Rev.*, 75:1908, 1949.
- [101] M. J. Buckingham. The surface photoelectric effect. *Phys. Rev.*, 80:704, 1950.
- [102] W. L. Schaich and N. W. Ashcroft. Model calculations in the theory of photoemission. *Phys. Rev. B*, 3:2452, 1971.
- [103] P. J. Feibelman and D. E. Eastman. Photoemission spectroscopy- correspondence between quantum theory and experimental phenomenology. *Phys. Rev. B*, 10:4932, 1974.
- [104] J.B. Pendry. Theory of photoemission. *Surf. Sci.*, 57:679, 1976.
- [105] J.B. Pendry. Angular dependence of electron emission from surfaces. *J. Phys. C: Solid State Phys.*, 8:2413, 1975.
- [106] A. Liebsch. Theory of photoemission from localized adsorbate levels. *Phys. Rev. B*, 13:544, 1976.
- [107] A. Liebsch, edited by L Fiermans, J Vennik, and W Dekeyser. *Electron and ion spectroscopy of solids*.

- [108] M. Lindroos and A. Bansil. Surface states and angle-resolved photoemission spectra from  $\text{Nd}_{2-x}\text{Ce}_x\text{CuO}_4$  superconductor. *Phys. Rev. Lett.*, 75:1182, 1995.
- [109] M. Lindroos and A. Bansil. A novel direct method of fermi surface determination using constant initial energy angle-scanned photoemission spectroscopy. *Phys. Rev. Lett.*, 77:2985, 1996.
- [110] A. Bansil and M. Lindroos. Angle-resolved photo-intensities in high- $T_c$ s: Surface states,  $\text{CuO}_2$  plane bands, lineshapes, and related issues. *J. Phys. Chem. Solids*, 56:1855, 1995.
- [111] A. Bansil and M. Lindroos. Matrix element effects in the angle-resolved photoemission spectrum of BISCO. *J. Phys. Chem. Solids*, 59:1879, 1998.
- [112] A. Bansil and M. Lindroos. Importance of Matrix Elements in the ARPES Spectra of BISCO. *Phys. Rev. Lett.*, 83:5154, 1999.
- [113] M.B.J. Meinders. PhD thesis, University of Groningen, The Netherlands, 1994.
- [114] H. Y. Fan. Theory of Photoelectric Emission from Metals. *Phys. Rev.*, 68:43, 1945.
- [115] C. N. Berglund and W. E. Spicer. Photoemission studies of copper and silver: theory. *Phys. Rev.*, 136:A1030, 1964.
- [116] J. W. Gadzuk and M. Sunjić. Excitation energy dependence of core-level X-ray photoemission spectra line shapes in metals. *Phys. Rev. B*, 12:524, 1975.
- [117] T. Pillo. PhD thesis, University of Freiburg, Switzerland, 1999.
- [118] A. Damascelli, Z. Hussain, and Z-X Shen. Angle-resolved photoemission studies of the cuprate superconductors. *Rev. Mod. Phys.*, 75:473, 2003.
- [119] V. N. Strocov, H. I. Starnberg, P. O. Nilsson, H. E. Brauer, and L. J. Holleboom. New method for absolute band structure determination by combining photoemission with very-low-energy electron diffraction: application to layered  $\text{VSe}_2$ . *Phys. Rev. Lett.*, 79:467, 1997.
- [120] V. N. Strocov and R. Claessen and G. Nicolay and S. Hüfner and A. Kimura and A. Harasawa and S. Shin and A. Kakizaki and P. O. Nilsson and H. I. Starnberg and P. Blaha. Absolute band mapping by combined angle-dependent very-low-energy electron diffraction and photoemission: application to Cu. *Phys. Rev. Lett.*, 81:4943, 1998.

- [121] A. Kanigel, M. R. Norman, M. Randeria, U. Chatterjee, S. Suoma, A. Kaminski, H. M. Fretwell, S. Rosenkranz, T. Sato, M. Shi, T. Takahashi, Z. Z. Li, H. Raffy, K. Kadowaki, D. Hinks, L. Ozyuzer, and J. C. Campuzano. Evolution of the pseudogap from Fermi arcs to the nodal liquid. *Nature Physics*, 2:447, 2006.
- [122] N. V. Smith, P. Thiry, and Y. Petroff. Photoemission linewidths and quasiparticle lifetimes. *Phys. Rev. B*, 47:15476, 1993.
- [123] J. Zhao. PhD thesis, University of Illinois at Chicago, USA, 2012.
- [124] A. A. Abrikosov, L. P. Gor'kov, L. P., and I. E. Dzyaloshinskii. *Quantum field theoretical methods in statistical physics*.
- [125] L. Hedin, S. Lundqvist, edited by H. Ehrenreich, F. Seitz, and D. Turnbull. *Solid state physics: Advances in research and applications (vol 23)*.
- [126] A. L. Fetter and J. D. Walecka. *Quantum theory of many-particle systems*.
- [127] G.D. Mahan. *Many-particle physics*.
- [128] E. N. Economou. *Green's functions in quantum physics (Springer Series in Solid State Science - vol 7)*.
- [129] G. Rickayzen. *Green's Functions and Condensed Matter (Techniques of Physics - vol 7)*.
- [130] M. R. Norman, H. Ding, H. Fretwell, M. Randeria, and J. C. Campuzano. Extraction of the electron self-energy from angle-resolved photoemission data: Application to  $\text{Bi}_2\text{Sr}_2\text{CaCu}_2\text{O}_{8+x}$ . *Phys. Rev. B*, 60:7585, 1999.
- [131] J. D. Rameau. PhD thesis, State University of New York at Stony Brook, USA, 2009.
- [132] F. Flicker and J. van Wezel. Charge order in  $\text{NbSe}_2$ . *Phys. Rev. B*, 94:235135, 2016.
- [133] S. V. Borisenko, A. A. Kordyuk, V. B. Zabolotnyy, D. S. Inosov, D. Evtushinsky, B. Büchner, A. N. Yaresko, A. Varykhalov, R. Follath, W. Eberhardt, L. Patthey, and H. Berger. Two energy gaps and Fermi-surface arcs in  $\text{NbSe}_2$ . *Phys. Rev. Lett.*, 102:166402, 2009.
- [134] G. Wexler and A. M. Woolley. Fermi surfaces and band structures of the 2H metallic transition metal dichalcogenides. *J. Phys. C: Solid State Phys.*, 9:1185, 1976.

- [135] N. V. Smith, S. D. Kevan, and F. J. DiSalvo. Band structures of the layered compounds 1T-TaS<sub>2</sub> and 2H-TaSe<sub>2</sub> in the presence of commensurate charge density waves. *J. Phys. C: Solid State Phys.*, 18:3175, 1985.
- [136] R. E. Thorne. Charge density wave conductors. *Phys. Today*, 49:42, May 1996.
- [137] R. Peierls. *More surprises in theoretical physics*.
- [138] G. Grüner. *Density waves in solids*.
- [139] F. Weber, S. Rosenkranz, J.-P. Castellan, R. Osborn, R. Hott, R. Heid, K.-P. Bohnen, T. Egami, A. H. Said, and D. Reznik. Extended phonon collapse and the origin of the charge density wave in 2H-NbSe<sub>2</sub>. *Phys. Rev. Lett.*, 107:107403, 2011.
- [140] S. V. Borisenko, A. A. Kordyuk, A. N. Yaresko, V. B. Zabolotnyy, D. S. Inosov, R. Schuster, B. Büchner, R. Weber, R. Follath, L. Patthey, and H. Berger. Pseudogap and charge density waves in two dimensions. *Phys. Rev. Lett.*, 100:196402, 2008.
- [141] J. Laverock, D. Newby Jr., E. Abreu, R. Averitt, K. E. Smith, R. P. Singh, G. Balakrishnan, J. Adell, and T. Balasubramanian. k-resolved susceptibility function of 2H-TaSe<sub>2</sub> from angle-resolved photoemission. *Phys. Rev. B.*, 88:035108, 2013.
- [142] M. D. Johannes, I. Mazin, and C. A. Howells. Fermi-surface nesting and the origin of the charge density wave in NbSe<sub>2</sub>. *Phys. Rev. B*, 73:205102, 2006.
- [143] N. J. Doran, D. Titterton, B. Ricco, M. Schreiber, and G. Wexler. The electronic susceptibility and charge density waves in 2H layer compounds. *J. Phys. C*, 11:699, 1978.
- [144] T. M. Rice and G. K. Scott. New mechanism for a charge density wave Instability. *Phys. Rev. Lett.*, 35:120–123, 1975.
- [145] W. C. Tonjes, V. A. Greanya, Rong Liu, C. G. Olson, and P. Molinié. Charge density wave mechanism in the 2H-NbSe<sub>2</sub> family: angle-resolved photoemission studies. *Phys. Rev. B*, 63:235101, 2001.
- [146] U. Chatterjee, J. Zhao, M. Iavarone, R. Di Capua, J. P. Castellan, G. Karapetrov, C. D. Malliakas, M. G. Kanatzidis, H. Claus, J. P. C. Ruff, F. Weber, J. van Wezel, J. C. Campuzano, R. Osborn, M. Randeria, N. Trivedi, M. R. Norman, and S. Rosenkranz. Emergence of coherence in the charge-density wave state of 2H-NbSe<sub>2</sub>. *Nat. Commun.*, 6:6313, 2015.

- [147] K. Rossnagel, O. Seifarth, L. Kipp, M. Skibowski, D. Voß, P. Krüger, A. Mazur, and J. Pollmann. Fermi surface of 2H-NbSe<sub>2</sub> and its implications on the charge density wave mechanism. *Phys. Rev. B*, 64:235119, 2001.
- [148] R. Liu, W. C. Tonjes, V. A. Greanya, C. G. Olson, and R. F. Frindt. Fermi surface of 2H-TaSe<sub>2</sub> and its relation to the charge density wave. *Phys. Rev. B*, 61:5212, 2000.
- [149] W. C. Tonjes, R. Liu, C. G. Olson and R. F. Frindt. Momentum dependent spectral changes induced by the charge density wave in 2H-TaSe<sub>2</sub> and the implication on the CDW mechanism. *Phys. Rev. Lett.*, 80:5762, 1998.
- [150] F. Flicker and J. van Wezel. Charge order from orbital-dependent coupling evidenced by NbSe<sub>2</sub>. *Nat. Commun.*, 6:7034, 2015.
- [151] C. M. Varma and A. L. Simons. Strong coupling theory of charge density wave transitions. *Phys. Rev. Lett.*, 51:138–141, 1983.
- [152] A. Taraphder, S. Koley, N. S. Vidhyadhiraja, and M. S. Laad. Preformed excitonic liquid route to a charge density wave in 2H-TaSe<sub>2</sub>. *Phys. Rev. Lett.*, 106:236405, 2011.
- [153] S. Koley, N. Mohanta, and A. Taraphder. The unusual normal state and charge-density-wave order in 2H-NbSe<sub>2</sub>. *J. Phys.: Condens. Matter*, 27:185601, 2015.
- [154] X. Zhu, Y. Cao, J. Zhang, E. W. Plummer, and J. Guo. Classification of charge density waves based on their nature. *Proc. Natl. Acad. Sci. U.S.A.*, 112:2367–2371, 2015.
- [155] H.-M. Eiter, M. Lavagnini, R. Hackl, E. A. Nowadnick, A. F. Kemper, T. P. Devereaux, J.-H. Chu, J. G. Analytis, I. R. Fisher, and L. Degiorgi. Alternative route to charge density wave formation in multiband systems. *Proc. Natl. Acad. Sci. U.S.A.*, 110:64–69, 2012.
- [156] T. C. Chiang. Photoemission spectroscopy in solids. *Ann. Phys. (Leipzig)*, 10:61–74, 2001.
- [157] A.A. Kordyuk. Arpes experiment in fermiology of quasi-2d metals. *Low Temp. Phys*, 40:286–296, 2014.
- [158] J. C. Campuzano, M. R. Norman, and M. Randeria. *Photoemission in the High-Tc Superconductors*.

- [159] H.-B. Yang, J. D. Rameau, P. D. Johnson, T. Valla, A. Tsvelik, and G. D. Gu. Emergence of preformed Cooper pairs from the doped Mott insulating state in  $\text{Bi}_2\text{Sr}_2\text{CaCu}_2\text{O}_{8+\delta}$ . *Nature (London)*, 456:77, 2008.
- [160] J. D. Rameau, H.-B. Yang, and P. D. Johnson. Application of the Lucy–Richardson deconvolution procedure to high resolution photoemission spectra. *J. Electron Spectrosc. Relat. Phenom.*, 181:35, 2010.
- [161] C. J. Arguello, S. P. Chockalingam, E. P. Rosenthal, L. Zhao, C. Gutiérrez, J. H. Kang, W. C. Chung, R. M. Fernandes, S. Jia, A. J. Millis, R. J. Cava, and A. N. Pasupathy. Visualizing the charge density wave transition in 2H-NbSe<sub>2</sub> in real space. *Phys. Rev. B*, 89:235115, 2014.
- [162] J. i. Okamoto, C. J. Arguello, E. P. Rosenthal, A. N. Pasupathy, and A. J. Millis. Quasiparticle interference, quasiparticle interactions, and the origin of the charge density wave in 2H-NbSe<sub>2</sub>. *Phys. Rev. Lett.*, 114:037001, 2015.
- [163] M. M. Ugeda, A. J. Bradley, Y. Zhang, S. Onishi, Y. Chen, W. Ruan, C. Ojeda-Aristizabal, H. Ryu, M. T. Edmonds, H.-Z. Tsai, A. Riss, S.-K. Mo, D. Lee, A. Zettl, Z. Hussain, Z.-X. Shen, and M. F. Crommie. Characterization of collective ground states in single-layer NbSe<sub>2</sub>. *Nat. Phys.*, 12:92, 2016.
- [164] D. W. Shen, B. P. Xie, J. F. Zhao, L. X. Yang, L. Fang, J. Shi, R. H. He, D. H. Lu, H. H. Wen, and D. L. Feng. Novel mechanism of a charge density wave in a transition metal dichalcogenide. *Phys. Rev. Lett.*, 99:216404, 2007.
- [165] T.D. Shen, L. Yang, Y. Zhang, J. Shen, L. Fang, J. Yan, D. Ma, H. Wen, and D. Feng. Extraction of a clean charge-density-wave gap for 2H-Na<sub>x</sub>TaS<sub>2</sub>. *J. Phys. Chem. Solids*, 69:2956, 2008.
- [166] W. Z. Hu, G. Li, J. Yan, H. H. Wen, G. Wu, X. H. Chen, and N. L. Wang. Optical study of the charge-density-wave mechanism in 2H-TaS<sub>2</sub> and Na<sub>x</sub>TaS<sub>2</sub>. *Phys. Rev. B*, 76:045103, 2007.
- [167] J. Dai, E. Calleja, J. Alldredge, X. Zhu, L. Li, W. Lu, Y. Sun, T. Wolf, H. Berger, and K. McElroy. Microscopic evidence for strong periodic lattice distortion in two-dimensional charge-density wave systems. *Phys. Rev. B*, 89:165140, 2014.
- [168] H. Ding, T. Yokoya, J. C. Campuzano, T. Takahashi, M. Randeria, M. R. Norman, T. Mochiku, K. Kadowaki, and J. Giapintzakis. Spectroscopic evidence for a pseudogap in the normal state of underdoped high-T<sub>c</sub> superconductors. *Nature (London)*, 382:51, 1996.

- [169] A. G. Loeser, Z.-X. Shen, D. S. Dessau, D. S. Marshall, C. H. Park, P. Fournier, and A. Kapitulnik. Excitation gap in the normal state of underdoped  $\text{Bi}_2\text{Sr}_2\text{CaCu}_2\text{O}_{8+\delta}$ . *Science*, 273:325, 1996.
- [170] T. Timusk and B. Statt. The pseudogap in high-temperature superconductors: an experimental survey. *Rep. Prog. Phys.*, 62:61, 1999.
- [171] U. Chatterjee, J. Zhao D. Ai, S. Rosenkranz, A. Kaminski, H. Raffy, Z. Li, K. Kadowaki, M. Randeria, M. R. Norman, and J. C. Campuzano. Electronic phase diagram of high-temperature copper oxide superconductors. *Proc. Natl. Acad. Sci. USA*, 108:9346, 2011.
- [172] M. H. Whangbo and E. Canadell. Electronic origin of the structural modulations in layered transition metal dichalcogenides (Analogies between the concepts of molecular chemistry and solid-state physics concerning structural instabilities) . *J. Am. Chem. Soc.*, 114:9587, 1992.
- [173] J. van Wezel. Polar charge and orbital order in 2H-TaS<sub>2</sub>. *Phys. Rev. B*, 85:035131, 2012.
- [174] C. M. Varma, E. I. Blount, P. Vashishta, and W. Weber. Electron-phonon interactions in transition metals. *Phys. Rev. B*, 19:6130, 1979.
- [175] D. Mou, R. Jiang, V. Taufour, R. Flint, S. L. Budko, P. C. Canfield, J. S. Wen, Z. J. Xu, G. Gu, and A. Kaminski. Strong interaction between electrons and collective excitations in the multiband superconductor MgB<sub>2</sub>. *Phys. Rev. B*, 91:140502(R), 2015.
- [176] P. D. Johnson, A. V. Fedorov, and T. Valla. Photoemission studies of self-energy effects in cuprate superconductors. *J. Electron Spectrosc. Relat. Phenom.*, 117-118:153–164, 2001.
- [177] L. Wray, D. Qian, D. Hsieh, Y. Xia, L. Li, J. G. Checkelsky, A. Pasupathy, K. K. Gomes, C. V. Parker, A. V. Fedorov, G. F. Chen, J. L. Luo, A. Yazdani, N. P. Ong, N. L. Wang, and M. Z. Hasan. Momentum dependence of superconducting gap, strong-coupling dispersion kink, and tightly bound Cooper pairs in the high- $T_c$   $(\text{Sr,Ba})_{1-x}(\text{K,Na})_x\text{Fe}_2\text{As}_2$ . *Phys. Rev. B*, 78:184508, 2008.
- [178] T. Valla, A. V. Fedorov, P. D. Johnson, and S. L. Hulbert. Many-Body Effects in Angle-Resolved Photoemission: Quasiparticle Energy and Lifetime of a Mo(110) Surface State. *Phys. Rev. Lett.*, 83:2085, 1999.
- [179] Ph Hofmann, I. Yu Sklyadneva, E. D. L. Rienks, and E. V. Chulkov. Electron-phonon coupling at surfaces and interfaces. *New J. Phys.*, 11:125005, 2009.

- [180] Z. Sun, Y.-D. Chuang, A. V. Fedorov, J. F. Douglas, D. Reznik, F. Weber, N. Aliouane, D. N. Argyriou, H. Zheng, J. F. Mitchell, T. Kimura, Y. Tokura, A. Revcolevschi, and D. S. Dessau. Quasiparticle like peaks, kinks, and electron-phonon coupling at the  $(\pi,0)$  Regions in the CMR Oxide  $\text{La}_{2-2x}\text{Sr}_{1+2x}\text{Mn}_2\text{O}_7$ . *Phys. Rev. Lett.*, 97:056401, 2006.
- [181] T. Valla, A. V. Fedorov, P. D. Johnson, J. Xue, K. E. Smith, and F. J. DiSalvo. Charge density wave induced modifications to the quasiparticle self-energy in 2H-TaSe<sub>2</sub>. *Phys. Rev. Lett.*, 85:4759, 2000.
- [182] K. Rossnagel, Eli Rotenberg, N. V. Smith H. Koh, and L. Kipp. Fermi surface, charge-density-wave gap, and kinks in 2H-TaSe<sub>2</sub>. *Phys. Rev. B*, 72:121103(R), 2005.
- [183] S. Sugai, K. Murase, S. Uchida, and S. Tanaka. Studies of lattice dynamics in 2H-TaS<sub>2</sub> by Raman scattering. *Solid State Commun.*, 40:399–401, 1981.
- [184] W. G. McMullan and J. C. Irwin. Long-wavelength phonons in 2H-NbS<sub>2</sub>, 2H-TaS<sub>2</sub> and  $\text{Ag}_x\text{TaS}_2$ . *Can. J. Phys.*, 62:789, 1984.
- [185] P. Lazar, J. Martincova, and M. Otyepka. Structure, dynamical stability, and electronic properties of phases in TaS<sub>2</sub> from a high-level quantum mechanical calculation. *Phys. Rev. B*, 92:224104, 2015.
- [186] T. Valla, A. V. Fedorov, P. D. Johnson, P-A. Glans, C. McGuinness, K. E. Smith, E. Y. Andrei, and H. Berger. Quasiparticle spectra, charge density Waves, superconductivity, and electron-phonon coupling in 2H-NbSe<sub>2</sub>. *Phys. Rev. Lett.*, 92:086401, 2004.
- [187] A. A. Andreev and V. N. Radionov. *Sov. Phys. Semicond.*, 1:145, 1967.
- [188] H. Sitter, K. Lischka, and H. Heinrich. Structure of the second valence band in PbTe. *Phys. Rev. B*, 16:145, 1967.
- [189] Yu. I. Ravich, B. A. Efimova, and V. I. Tamarchenko. Scattering of current carriers and transport phenomena in lead chalcogenides. *Phys. Status Solidi B*, 43:11, 1971.
- [190] Christopher M. Jaworski, Michele D. Nielsen, Hsin Wang, Steven N. Girard, Wei Ca, Wally D. Porter, Mercouri G. Kanatzidis, and Joseph P. Heremans. Valence-band structure of highly efficient p-type thermoelectric PbTe-PbS alloys. *Phys. Rev. B*, 87:045203, 2013.

- [191] Z. M. Gibbs, H. Kim, H. Wang, R. L. White, F. Drymiotis, M. Kaviany, and G. J. Snyder. Temperature dependent band gap in PbX (X = S, Se, Te). *Appl. Phys. Lett.*, 103:262109, 2013.
- [192] R. S. Allgaier and B. B. Houston Jr. Hall coefficient behavior and the second valence band in lead telluride. *J. Appl. Phys.*, 37:302, 1966.
- [193] C. E. Ekum, D. J. Singh, J. Moreno, and M. Jarrell. Optical properties of PbTe and PbSe. *Phys. Rev. B*, 85:085205, 2012.
- [194] D. J. Singh. Doping-dependent thermopower of PbTe from boltzmann transport calculations. *Phys. Rev. B*, 81:195217, 2010.
- [195] V. Hinkel, H. Haak, C. Mariani, L. Sorba, K. Horn, and N. E. Christensen. Investigation of the bulk band structure of IV-VI compound semiconductors: PbSe and PbTe. *Phys. Rev. B*, 40:5549, 1989.
- [196] K. Nakayama, T. Sato, T. Takahashi, and H. Murakami. Doping induced evolution of fermi surface in low carrier superconductor TI-doped PbTe. *Phys. Rev. Lett.*, 100:227004, 2008.
- [197] A. Svane, N. E. Christensen, M. Cardona, A. N. Chantis, M. van Schilfgaarde, and T. Kotani. Quasiparticle self-consistent GW calculations for PbS, PbSe, and PbTe: Band structure and pressure coefficients. *Phys. Rev. B*, 81:245120, 2010.
- [198] B. Wiendlocha. Fermi surface and electron dispersion of PbTe doped with resonant Tl impurity from KKR-CPA calculations. *Phys. Rev. B*, 88:205205, 2013.
- [199] P. B. Littlewood, B. Mihaila, R. K. Schulze, D. J. Safarik, J. E. Gubernati, A. Bostwick, E. Rotenberg, C. P. Opeil, T. Durakiewicz, J. L. Smith, and J. C. Lashley. Band structure of snTe studied by photoemission spectroscopy. *Phys. Rev. Lett.*, 105:086404, 2010.
- [200] E. Miller, K. Komarek, and I. Cadoff. Interrelation of electronic properties and defect equilibria in PbTe. *J. Appl. Phys.*, 32:2457, 1961.
- [201] R. N. Tauber, A. A. Machonis, and I. B. Cadoff. Thermal and optical energy gaps in PbTe. *J. Appl. Phys.*, 37:4855, 1966.
- [202] Y. W. Tsang and Marvin L. Cohen. Calculation of the temperature dependence of the energy gaps in PbTe and SnTe. *Phys. Rev. B*, 3:1254, 1971.
- [203] R. Dalven. A review of the semiconductor properties of PbTe, PbSe, PbS and PbO. *Infrared Phys*, 9:141, 1969.

- [204] C. E. Hurwitz, A. R. Calawa, and R. H. Rediker. *IEEE J. Quantum Electron.*, Qe-1:102, 1965.
- [205] W. W. Scanlon. Recent advances in the optical and electronic properties of PbS, PbSe, PbTe and their alloys. *J. Phys. Chems. Solids*, 8:429, 1959.
- [206] H. Sitter, K. Lischka, and H. Heinrich. Structure of the second valence band in PbTe. *Phys. Rev. B*, 16:680, 1977.
- [207] Jack R. Dixon and H. R. Riedl. Electric-susceptibility hole mass of PbTe. *Phys. Rev.*, 138:A873, 1965.
- [208] N. V. Kolomoet, M.N. Vinograd, and L. M. Sysoeva. *Sov. Phys. Semicond.*, 1: 1020, 1968.
- [209] R. S. Allgaier. Valence bands in PbTe. *J. Appl. Physics.*, 32:2185, 1961.
- [210] J. J. Harris and B.K. Ridley. Room temperature transport properties of p-type PbTe. , *J. Phys. Chem. Solids*, 33:1455, 1972.
- [211] H. R. Riedl. Free-Carrier Absorption in p-Type PbTe. *Phys. Rev*, 127:162, 1962.
- [212] G. Nimtz and B. Schlicht. *Narrow-gap lead salts (Springer tracts in modern physics - vol. 98)*.
- [213] L. M. Rogers. The Hall mobility and thermoelectric power of p-type lead telluride. *Br. J. Appl. Phys.*, 18:1227, 1967.
- [214] S. V. Airapetyants, M. N. Vinogradova, I. N. Dubrovskaya, N. V. Kolomoets, and I. M. Rudnik. *Sov. Phys. Solid State*, 8:1069, 1966.
- [215] A. J. Strauss. Inversion of conduction and valence bands  $Pb_{1-x}Sn_xSe$  Alloys. *Phys. Rev.*, 157:608, 1967.
- [216] A. Andrevv. The band edge structure of the IV-VI semiconductors. *Journal de Physique Colloques*, 29 (C4):50, 1968.
- [217] Yu. I. Ravich and S. A. Nemov. Hopping conduction via strongly localized impurity states of Indium in PbTe and its solid solutions. *Phys. Usp.*, 41:735, 1998.
- [218] D.L.Mitchell, E. D. Palik, and J. N. Zemel. Magneto-optical band studies of epitaxial PbS, PbSe and PbTe. *Physics. of Semiconductors: Proceedings of the seventh international conference, Paris*, page 325, 1964.
- [219] S. P. Chashchln, I. S. Averyanov, N. S. Baryshev, V. A. Kudryashov, N. P. Markina, and Y. A. Shuba. *Sov. Phys. Semicond.*, 3:1055, 1970.